ABSTRACT

Title of dissertation: CONSTRAINING HIGH-ENERGY DARK MATTER SIGNALS

James Patrick Harding, Doctor of Philosophy, 2012

Dissertation directed by: Professor Kevork N. Abazajian and Professor Zackaria Chacko
Department of Physics

I consider methods of indirect detection of dark matter annihilation, including astrophysical foreground modeling, techniques for background removal, and current and predicted limits to the dark matter annihilation and decay rate. Dark matter signals from several sources are considered: the center of the Milky Way Galaxy, the Milky Way Galactic halo, diffuse extragalactic emission, and dwarf galaxies.

The strongest dark matter signal is expected to come from the inner degrees of the Galaxy. With the signal and background regions from the High Energy Spectroscopic System (HESS) collaboration from the Galactic center, I derive the strongest constraints on TeV-scale dark matter. I consider a number of dark matter models, including those with Sommerfeld-enhanced cross-sections, and show that the HESS Galactic center observations are in tension with many of these dark matter models. At lower energies in the Galactic center, the Wilkinson Microwave Anisotropy Probe (WMAP) sees extended emission, the "WMAP haze", which is consistent with the synchrotron radiation from a population of high-energy electrons and positrons.

Comparing the e^+e^- emission from pulsars and dark matter annihilation in the as a source for this synchrotron emission, the two sources show morphological differences, with dark matter giving a more sharply-peaked flux profile and pulsars giving a more extended profile. Both sources give signals consistent with the WMAP haze, but future experiments should be able to identify the source of the emission based on morphology.

I also discuss the modeling of blazars, one of the largest foregrounds in the extragalactic gamma-ray sky. I present a model of blazars which yields gamma-ray flux consistent with the diffuse gamma-ray background (DGRB) radiation observed by the Large Area Telescope (LAT) on the Fermi Gamma-Ray Space Telescope. Specifically, I model the emission from blazars with a luminosity-dependent luminosity evolution model for the blazar gamma-ray luminosity function and use a blazar spectral energy distribution for the blazar emission spectra. By extending this model to the Fermi-LAT 5-year sensitivity, I show that the DGRB will decrease by a factor of $\sim 2-3$ with five years of Fermi-LAT observations. An analysis of the DGRB is used to constrain the cross-section of dark matter annihilations for several dark matter annihilation channels and masses, and I include a predicted constraint from the Fermi-LAT 5-year DGRB forecast. I also consider the effects of gamma-rays from inverse-Compton emission on the dark matter annihilation signal and consider the dark matter cross-section limits when including this effect.

I conclude with the expected sensitivity of the water Cherenkov detector to high-mass annihilating dark matter from both the Galactic center and dwarf galaxies. At high dark matter masses, the High Altitude Water Cherenkov (HAWC)

Observatory should be more sensitive to dark matter in dwarf galaxies than prior experiments.

CONSTRAINING HIGH-ENERGY DARK MATTER SIGNALS

by

James Patrick Harding

Dissertation submitted to the Faculty of the Graduate School of the
University of Maryland, College Park in partial fulfillment
of the requirements for the degree of
Doctor of Philosophy
2012

Advisory Committee:
Professor Zackaria Chacko, Chair
Professor Kevork N. Abazajian, Co-Chair/Advisor
Professor Rabindra Mohapatra
Professor Jordan Goodman
Professor Massimo Ricotti

Acknowledgments

Foremost, I would like to thank my advisor, Professor Kevork Abazajian, for providing interesting and challenging research opportunities over the last four years. His guidance has been superlative, and he has been very eager to send me to conferences and introduce me to other researchers in the field. This thesis truly could not have happened without his help and encouragement.

I would like to thank the faculty and staff of the University of Maryland Physics Department and the Maryland Center for Fundamental Physics in particular for providing a supportive education and research atmosphere. I especially owe my thanks to Professor Zackaria Chacko for helping to chair my dissertation, and to Professor Rabindra Mohapatra, Professor Jordan Goodman, and Professor Massimo Ricotti for taking the time from their busy schedules to read this thesis and serve on my dissertation committee.

My family has been the one constant during the years, and no amount of thanks can ever express the gratitude I feel toward them. Dad, Mom, Lisa, Joel, Anne, and Brooke, your well-wishes have been received and embraced from across the country. And to my extended family as well, your love and support has been a blessing.

To my roommates through the years, it has been a pleasure. Remington, Jennifer, Brandon, Bill, Kevin, and Lindy, our discussions have been one of the great pleasures these past years. To all the friends I have made in Maryland, I wish you all the best.

Finally, to Mary, you have been the best friend and partner I could have asked for. Thank you for being there through it all.

Chapters 2-5 of this thesis are published, and Chapter 6 is being prepared for publication. I was the primary researcher for each of these papers.

Chapter 2 is a reproduction of K. N. Abazajian and J. P. Harding, JCAP 1201 (2012) 041, [arXiv:1110.6151]. We thank Prateek Agrawal, Mike Boylan-Kolchin, Manoj Kaplinghat, Mike Kuhlen, Tracy Slatyer and Neal Weiner for useful discussions. KNA & JPH are supported by NSF Grant 07-57966 and NSF CAREER Award 09-55415.

Chapter 3 is a reproduction of J. P. Harding and K. N. Abazajian, Phys. Rev. D 81 (2010) 023505, [arXiv:0910.4590]. We thank Z. Chacko, Doug Finkbeiner, Ted Jacobson, and Manoj Kaplinghat for useful discussions. J.P.H. is partially supported by the UMD/GSFC Joint Space Institute and the Maryland Center for Fundamental Physics. K.N.A. is partially supported by NSF Theoretical Physics Grant No. 0757966.

Chapter 4 is a reproduction of K. N. Abazajian, S. Blanchet, and J. P. Harding, Phys. Rev. D 84 (2011) 103007, [arXiv:1012.1247]. We would like to thank P. Agrawal, M. Ajello, J. Beacom, Z. Chacko, D. Malyshev and J. McEnery for useful discussions. KNA and JPH are supported by NSF Grant 07-57966 and NSF CAREER Award 09-55415. SB has been partially supported by MICNN, Spain, under contracts FPA 2007-60252 and Consolider-Ingenio CPAN CSD2007-00042 and by the Comunidad de Madrid through Proyecto HEPHACOS ESP-1473. SB acknowledges support from the CSIC grant JAE-DOC.

Chapter 5 is a reproduction of K. N. Abazajian, S. Blanchet, and J. P. Harding, Phys. Rev. D 85 (2012) 043509, [arXiv:1011.5090]. We would like to thank P. Agrawal, J. Beacom, Z. Chacko, J. McEnery and N. Weiner for useful discussions. KNA and JPH are supported by NSF Grant No. 07-57966 and NSF CAREER Award No. 09-55415. This work has been partially supported by MICNN, Spain, under contracts FPA 2007-60252 and Consolider-Ingenio CPAN CSD2007-00042 and by the Comunidad de Madrid through Proyecto HEPHACOS ESP-1473. S.B. acknowledges support from the CSIC under Grant No. JAE-DOC.

Chapter 6 is being prepared for publication by K. N. Abazajian, B. Baughman, and J. P. Harding, for the HAWC Collaboration.

Table of Contents

List of Tables

List of Figures

Chapter 1

Introduction to Dark Matter Indirect Detection

1.1 Evidence for Dark Matter

Since its discovery in the 1930s, the evidence for dark matter has been plentiful. Dark matter was first discovered by observations that rotation curves in galaxies and clusters differed significantly from the rotation curve expected from the observed luminous matter [1]. The luminous matter of galaxies is largely contained within the inner few kiloparsecs of the galaxy. According to the law of gravitation, in the outer regions of a galaxy, the circular velocity of observed bodies should therefore follow:

$$F_G = \frac{GmM(<r)}{r^2} = \frac{mv_{\rm cir}^2}{r} \tag{1.1}$$

$$v_{\rm cir}(r) \propto r^{-1/2} \ , \tag{1.2}$$

with $M(<r)$ the mass contained with radius from the galactic center r and $v_{\rm cir}$ the circular velocity at radius r. However, the circular velocity tends to flatten out at large radii rather than decreasing, consistent with

$$\begin{aligned} M(<r) &\propto r \\ \rho_M &\propto r^{-2} \ . \end{aligned} \tag{1.3}$$

This indicates an additional mass component to galaxies which is not luminous and has a density profile $\rho_M \propto r^{-2}$ which continues out to large radii. This additional,

non-luminous mass is referred to as "dark matter". Further evidence for the dark matter comes from anisotropies in the cosmic microwave background (CMB), which has shown that the dark matter makes up 22.8% of the energy budget of the universe, but ordinary baryonic matter makes up only 4.6% [2]. The case for dark matter has also been made based on large-scale structure of the universe [3, 4] and observations of galaxy clusters [5, 6].

Although dark matter has only been observed through its gravitational interactions, the properties of dark matter are well constrained. Observations of gravitational microlensing have determined that the dark matter is made up of particles with masses $M_\chi \lesssim 10^{-7} M_\odot$. Baryonic clumps of matter cannot explain the majority of the dark matter observed in the Galaxy [7–9]. Additionally, the particles making up the dark matter cannot have ultrarelativistic velocities without underproducing the temperature variations in the CMB, so the dark matter mass must be greater than $M_\chi \gtrsim 10$ eV.

The most popular dark matter model is the weakly interacting massive particle (WIMP), with a dark matter particle of mass $M_\chi \sim 100$ GeV which interacts through the weak force. WIMPs were formed in the early universe in equilibrium with other particles at high temperature. As the universe cooled, WIMPs collided and annihilated into standard model particles. However, once the expansion of the universe exceeded the annihilation rate of the WIMPs, they stopped annihilating and the number density of WIMPs "froze out", giving the dark matter number density seen today. The so-called "WIMP Miracle" is that for a WIMP with weak-scale cross-section ($\sigma \sim 1$ pb) and a weak-scale mass ($M_\chi \sim 100$ GeV), the relic density

of thermal WIMPs is $\Omega_{WIMP} \approx 0.2$, consistent with the energy density for the dark matter. For a detailed calculation of the thermal WIMP cross-section, see Appendix A.

1.2 Calculations of the Dark Matter Annihilation Flux

1.2.1 Particle Flux from Dark Matter Annihilations

The number of dark matter annihilations per unit volume is $\rho(\vec{x})^2/(2M_\chi^2)\langle\sigma_{\rm A}v\rangle$, for dark matter mass M_χ and dark matter number density ρ/M_χ . $\langle\sigma_{\rm A}v\rangle$ is the annihilation cross-section times the relative velocity between interacting dark matter particles, averaged over their velocity distribution, and the factor of two comes from symmetry concerns. The number of dark matter collisions per unit time per unit observational area integrated along a particular line-of-sight is then

$$\frac{dN}{dtdA} = \frac{\langle\sigma_{\rm A}v\rangle}{2M_\chi^2}\int \frac{r^2 dr d\Omega}{4\pi r^2}\rho(\vec{x})^2 = \frac{\langle\sigma_{\rm A}v\rangle}{2M_\chi^2}\int \frac{dr d\Omega}{4\pi}\rho(\vec{x})^2 \ . \tag{1.4}$$

Observationally, we detect the number of Standard Model particles per unit energy produced by dark matter annihilations rather than the annihilations themselves. For an annihilation final-state f, the branching fraction B_f is the fraction of time a dark matter annihilation will end up in that final state. For a particular Standard Model particle i, $dN_f^{(i)}/dE$ is the number of particles i per unit energy produced in final-state f. The details of which final states occur with which branching fractions depends on the precise dark matter model under consideration, though often, for simplicity, a particular dark matter annihilation channel is assumed to

dominate and its branching fraction is set to unity. To simulate hadronization and decay of standard model particles into final states, analytical expressions or simulations are used (e.g. PYTHIA [10]). The flux of particles i per units energy and solid angle coming from a region of dark matter annihilations is given by

$$\frac{dF_i}{dEd\Omega} = \frac{\langle \sigma_{\rm A} v \rangle}{2} \sum_f \frac{dN_f^{(i)}}{dE} B_f \int_0^\infty \frac{dr}{4\pi} \frac{\rho(\vec{x})^2}{M_\chi^2} \ . \tag{1.5}$$

1.2.2 Dark Matter Distributions

Dark matter in galaxies exists in a roughly spherically symmetric "halo" that approximately falls off as $\rho(r) \propto r^{-2}$ with the distance from the galactic center. Numerical N-body simulations have been done considering both pure dark matter and dark matter with baryons [11–23]. The most widely adopted dark matter profile is the Navarro-Frenk-White (NFW) profile [17], parameterized as

$$\rho(r) = \frac{\rho_s}{(r/r_s)(1+r/r_s)^2} \tag{1.6}$$

with scale radius $r_s \approx 20$ kpc for our Galaxy. The NFW profile is sometimes generalized as

$$\rho(r) = \frac{\rho_s}{(r/r_s)^\gamma (1+(r/r_s)^\alpha)^{(\beta-\gamma)/\alpha}} \tag{1.7}$$

to allow for cuspier or more-cored dark matter profiles, with the standard NFW profile having $(\alpha, \beta, \gamma) = (1, 3, 1)$. A somewhat shallower dark matter profile, the Einasto profile, is parameterized as [24, 25]

$$\rho(r) = \rho_s \exp\left[-\frac{2}{\alpha} \left(\left(\frac{r}{r_s} \right)^\alpha - 1 \right) \right], \tag{1.8}$$

with scale radius $r_s \approx 20$ kpc and $\alpha = 0.1 - 0.2$ for Milky-Way-type halos [18, 22]. The scale density for these Galactic dark matter profiles, ρ_s, is fixed such that the dark matter density at the solar distance $R_\odot \approx 8.5$ kpc is $\rho_\odot \approx 0.39$ GeV cm^{-3} [26, 27].

1.3 Overview of Topics Covered, by Chapter

The following chapters illustrate the diversity and complexity that is the indirect detection of dark matter. Therein, dark matter annihilation signals from several regions are considered: the Galactic center (GC), the outer Galaxy, and dwarf spheroidal galaxies. Populations of both Galactic pulsars and extragalactic blazars are included as backgrounds for dark matter signals. Both Earth-based and space-based observations are considered as possible detectors for the dark matter.

In Chapter 2, I examine the constraints on models of weakly interacting WIMP dark matter from the recent observations of the Galactic center by the High Energy Spectroscopic System (HESS) telescope, from [28]. In that work, we analyze canonical WIMP annihilation into Standard Model particle final states, including $b\bar{b}$, $t\bar{t}$, and W^+W^-. The constraints on annihilation into $b\bar{b}$ is within an order of magnitude of the thermal cross section at $\sim$3 TeV, while the $\tau^+\tau^-$ channel is within a factor of $\sim$2 of thermal. We also study constraints on Sommerfeld-enhanced dark matter annihilation models, and find that the gamma-ray observational constraints here rule out all of the parameter space consistent with dark matter annihilation interpretations of PAMELA and the Fermi-LAT e^+e^- spectrum, in specific classes of models,

and strongly constrains these interpretations in other classes. The gamma-ray constraints we find are more constraining on these models, in many cases, than current relic density, cosmic microwave background, halo shape and naturalness constraints.

Chapter 3, from [29], considers an excess in microwave emission coming from the GC, the "WMAP haze" and whether it is a dark matter signal or an astrophysical one. In that paper, in the case of synchrotron emission models of the haze, we present tests for the source of radiating high-energy electrons/positrons. We explore several models in the case of a pulsar population or dark matter annihilation as the source. These morphological signatures of these models are small behind the WMAP Galactic mask, but are testable and constrain the source models. We show that detailed measurements of the morphology may distinguish between the pulsar and dark matter interpretations as well as differentiate among different pulsar models and dark matter profile models individually. Specifically, we find that a zero central density Galactic pulsar population model is in tension with the observed WMAP haze. The upcoming Planck Observatory's greater sensitivity and expected smaller Galactic mask should potentially provide a robust signature of the WMAP haze as either a pulsar population or the dark matter.

Chapter 4 shows the consistency between the diffuse gamma-ray background (DGRB) and an unresolved population of blazars, done in Ref. [30]. We examine the constraints on the luminosity-dependent density evolution model for the evolution of blazars given the observed spectrum of the DGRB, blazar source count distribution, and the blazar spectral energy distribution sequence model, which relates the observed the blazar spectrum to its luminosity. We show that the DGRB

observed by the Large Area Telescope (LAT) aboard the Fermi Gamma Ray Space Telescope can be produced entirely by gamma-ray emission from blazars and non-blazar active galactic nuclei, and that our blazar evolution model is consistent with and constrained by the spectrum of the DGRB and flux source count distribution function of blazars observed by Fermi-LAT. Our results are consistent with previous work that used EGRET spectral data to forecast the Fermi-LAT DGRB. The model includes only three free parameters, and forecasts that $\gtrsim$95% of the flux from blazars will be resolved into point sources by Fermi-LAT with 5 years of observation, with a corresponding reduction of the flux in the DGRB by a factor of $\sim$2 to 3 (95% CL), which has implications for the Fermi-LAT's sensitivity to dark matter annihilation photons.

Chapter 5 is Ref. [31], the companion work to Ref. [30] of Chapter 4. It shows the dark matter constraints from the Fermi-LAT DGRB and considers how these constraints will improve if blazars are resolved as the blazar model in Chapter 3 predicts. We perform a detailed examination of current constraints on annihilating and decaying dark matter models from both prompt and inverse-Compton emission photons, including both model-dependent and model-independent bounds. We also show that the observed isotropic DGRB, which provides one of the most conservative constraints on models of annihilating weak-scale dark matter particles, may enhance its sensitivity by a factor of $\sim$ 2 to 3 (95% C.L.) as the Fermi-LAT experiment resolves DGRB contributing blazar sources with five years of observation. For our forecasts, we employ the results of constraints to the luminosity-dependent density evolution plus blazar spectral energy distribution sequence model, which is

constrained by the DGRB and blazar source count distribution function.

In Chapter 6, I show a forthcoming work which I have done with the High Altitude Water Cherenkov (HAWC) collaboration. In it, we show a forecast for dark matter annihilation limits from the HAWC observatory, considering dark matter annihilations into three channels: the hadronic $t\bar{t}$ channel, the bosonic W^+W^- channel, and the leptonic $\tau^+\tau^-$ channel. Using numerical models, we determine the significance of the dark matter signal coming from each of three regions, the Draco and Coma Berenices dwarf galaxies and the GC. Assuming that no signal is observed above background for these sources, we determine the dark matter annihilation cross-section limits that can be derived after one year of HAWC observations. Although it is located toward the horizon for the HAWC observatory, the GC will provide the strongest HAWC limits on dark matter annihilations, due to the large number of dark matter annihilations occurring there. For dwarf galaxies, on the other hand, the optimal sources are those which have the smallest zenith angle from the HAWC observatory, regardless of dark matter density. The HAWC forecasted cross-section limits give stronger constraints in many cases than the Fermi-LAT or air-Čerenkov detectors, at high dark matter masses.

Chapter 7 relates the different dark matter sources and detectors considered in this work, comparing their relative strengths. It also discusses the current status of the WMAP haze, from Chapter 3, and the blazar model of the DGRB, from Chapters 4 and 5. It concludes by discussing the status of indirect dark matter detection experiments in the near future.

Chapter 2

Constraints on WIMP and Sommerfeld-Enhanced Dark Matter Annihilation from HESS Observations of the Galactic Center

2.1 Introduction

The existence of cosmological dark matter has been well-established by observations of galaxy clusters, galaxy rotation curves, the cosmic microwave background (CMB), and large-scale cosmological structure. However the identity of the dark matter has remained a fundamental unsolved problem in cosmology and particle physics for nearly 80 years [1]. Several particle candidates have been proposed that could account for the dark matter (for a review, see, e.g. [32]). One well-motivated dark matter candidate is a weakly-interacting massive particle (WIMP), which can naturally produce a relic abundance at the observed dark matter density. Thermal production of dark matter prefers a scale of the dark matter cross-section at $\langle \sigma_{\rm A} v \rangle \approx 3 \times 10^{-26}$ cm^3 s^{-1}. This annihilation rate into Standard Model particles results in energetic gamma-ray production through the hadronization of quarks, bremsstrahlung of leptons, or directly into two gammas through higher-order processes. This leads to the so-called method of "indirect detection" of dark matter, constraining the dark matter mass, annihilation cross-section, and annihilation spectrum through a search for the Standard Model byproducts of WIMP annihilation.

The High Energy Stereoscopic System (HESS) telescope has strong sensitivity to high-energy gamma-rays such as those from high-mass WIMPs [33]. HESS consists of an array of atmospheric Čerenkov telescopes in Namibia designed to search for high-energy gamma-rays, with 960 pixels per telescope at a resolution of 0.16° per pixel [34]. Specifically, HESS is sensitive to gamma-ray energies from a few hundred GeV to a few tens of TeV. Previously, studies of the Galactic Ridge for $|\ell| < 0.8°$ and $|b| < 0.3°$ by HESS [35] have been used to limit the dark matter cross-section at high masses (0.5-30 TeV) [36–43]. However, an even more stringent constraint on the dark matter cross-section has been shown to come from a new analysis of a region around the Galactic Center (GC) [33]. Here, we analyze in detail the constraints arising from this observation.

The HESS GC analysis uses a reflected background technique to provide a robust background region for the gamma-ray signal from the GC. Because the background region is further from the GC than the source region, it is expected that the dark matter signal should be larger in the source region than the background region, for a dark matter halo profile whose density peaks toward the GC. The HESS GC analysis shows no excess gamma-ray signal in the source region over the background region. Therefore, any dark matter annihilation signal must produce few enough gamma-rays that the gamma-ray flux in the source region is indistinguishable from the gamma-ray flux in the background, at the current HESS sensitivity.

There have recently been stacked studies of the gamma-ray signals coming from dwarf spheroidal galaxies by the Fermi-LAT which have been used to constrain WIMP annihilation cross-sections and, in particular, have excluded thermal low-

mass WIMPs in the $b\bar{b}$ and $\tau^+\tau^-$ annihilation channels below $\sim$ 30 GeV [44, 45]. Here, we show that the HESS GC analysis provides much tighter constraints than the stacked Fermi-LAT dwarf spheroidals for dark matter masses above the Fermi-LAT energy window.

There remains interest in the possibility of dark matter annihilation as the source of the excess cosmic ray positron fraction at $\sim$ 10-100 GeV observed by the PAMELA satellite, with e^+e^- pairs produced either directly or indirectly in a dark matter particle pair annihilation cascade [46–49]. Additionally, features in the higher-energy 10^2 to 10^3 GeV e^+e^- spectrum seen by the Fermi-LAT [50] are also consistent with the dark matter annihilation interpretations of the lower energy positron excess data [41, 51, 52]. A recent study of the e^+e^- data from the Fermi-LAT is consistent with the positron excess of the PAMELA satellite and shows the spectrum continuing to rise up to at least $\sim$ 200 GeV [53].

In order to achieve the dark matter annihilation rate required for these e^+e^- signals while remaining consistent with the expected thermal production cross section, and to avoid an excess in anti-proton observations (which is not seen), the annihilation rate can be enhanced through a low-energy Sommerfeld-enhancement and limited to leptonic modes with a light ($<$ 1 GeV) dark-force carrying particle [54–57]. Such an enhanced cross-section from a new force is in tension with detailed calculations of the relic abundance of the dark matter, so that such a candidate in many cases may not contribute to all of the dark matter [58–62]. Such candidates are also constrained by non-thermal distortions of the CMB [62–65] and asphericity observed in dark matter halos [58, 60]. Cases of these models remain

viable given all such constraints [66, 67]. There are also constraints on these models from the observed diffuse gamma-ray and X-ray backgrounds [31, 68], observations toward the GC by Fermi-LAT [69], as well as big-bang nucleosynthesis [70, 71].

One model of dark matter with a light dark-force carrying particle and Sommerfeld-enhanced cross-section is "eXciting dark matter" (XDM) [54, 72]. XDM was initially proposed to explain the 511 keV gamma-ray signal from the GC (see Ref. [73] for a discussion of these signals). In XDM, there are two lowest-energy dark states χ and χ^* which have masses differing by only a few MeV, with a light gauge bosons ϕ mediating excitations from χ to χ^*. The exchange of many gauge bosons leads to a Sommerfeld-enhanced cross-section much larger than that of a thermal relic. The annihilation $\chi\chi \to \phi\phi$ followed by the decay of ϕ into leptons leads to an excess of high-energy electrons and positrons in the GC. This scenario has also been considered to explain the excess in local positrons seen by the PAMELA and Fermi-LAT satellites. Most recently, Ref. [66] has interpreted the XDM explanation for the PAMELA and Fermi-LAT excesses including constraints from the thermal relic density, CMB, self-interaction bounds, and naturalness bounds. Below, we compare the gamma-ray constraints from the HESS GC analysis to these other XDM limits.

The sensitivity of the HESS GC observation to dark matter annihilation, as with all Galactic Center observations, depends on the nature of the dark matter density profile. Specifically, for the HESS GC background subtraction method, there must be a higher dark matter density within the inner $\lesssim$150 pc, in the signal region, than the background subtraction region between approximately 150 pc and 450 pc. As pointed out also in the HESS Collaboration analysis [33], if there exists

a constant-density core within the inner ∼450 pc of the Milky Way, no limits on dark matter annihilation can be derived from the HESS GC observation since the background subtraction would also remove any equivalent signal.

There is significant debate in the literature as to the nature of the inner dark matter profile of a galaxy such as the Milky Way. Numerical simulations are employed in attempts to accurately determine the inner dark matter density profile. The canonically-adopted dark matter halo density profile for the case of cold dark matter is the r^{-1} inner-radius scaling Navarro-Frenk-White (NFW) profile [17]. The highest spatial resolution simulations of Milky-Way-type halo formation are pure dark matter halo simulations: Via Lactea II [12], GHALO [22] and AQUARIUS (A-1) [18] (which have gravitational softening lengths of 40, 61 and 20 pc, respectively), which find a peaked density profile down to ∼100 pc, with a logarithmically-changing slope that is sometimes dubbed an "Einasto" profile. The vast majority of studies that include baryons in addition to dark matter have found that baryonic effects concentrate and steepen the central dark matter distribution due to adiabatic contraction [11, 13], including recent high-resolution simulations with gas cooling, star formation, and stellar feedback processes [14, 15, 19, 23]. Importantly, Ref. [14] does an extensive error analysis of their numerical results. In contrast, some studies' simulations have claimed that baryonic effects may have the opposite effect, reducing the dark matter density in the central region via dark matter expansion from stellar and gas feedback outflows, and producing flat or nearly-flat density cores at up to 2-3 kpc in size for an approximately Milky Way size halo, fit by cored isothermal or Burkert profiles [16, 20, 21]. It has been shown in Ref. [74] that the S2 or Plummer

force softening must be a factor of ≈5 times smaller than the scale of interest for the inner profile of dark matter halos in order to achieve greater than 5% accuracy in radial accelerations of particles, with an ideal time-step algorithm choice. Poor force resolution has been shown to generally lead to artificially lower central densities [75]. The gravitational softening length used in the simulations in Ref. [21] is 0.5 kpc, so it is questionable to draw conclusions at the claimed ∼kpc core scale. In the recent work of Ref. [16], the gravitational softening length is 0.3125 kpc [76], and therefore conclusions of the inner 1-2 kpc are also difficult to make with confidence. Furthermore, Ref. [16] finds evidence for a core to be produced only in the more extreme feedback High Feedback Run, while the Low Feedback Run found adiabatic contraction that steepened the dark matter profile.

In summary, work indicating the presence of dark matter density cores in numerical simulations are at the edge of their resolution limits. It is important to consider that if it becomes firmly established from numerical simulations that there is necessarily a constant-density core in the Milky Way at the $\gtrsim$ 450 pc scale, then the HESS GC limits presented here are not applicable due to the observation's background subtraction method. This was also noted by the HESS collaboration work [33]. However, at this time robust numerical simulations predominantly indicate contraction and steepening of the central density profile due to baryonic effects, and the adoption of the non-contracted NFW or Einasto profile here is conservative relative to the steeper profiles.

Below we show that, in the case of a non-adiabatically-contracted NFW or Einasto dark matter halo profile, the HESS GC observation provides a strong limit

on the cross-section of high-mass WIMPs' annihilation into several Standard Model channels. Furthermore, we show how the dark matter annihilation interpretation of the PAMELA excess and Fermi-LAT e^+e^- feature signals is excluded at above 95% CL in many cases. Dark matter interpretations of these signals are in tension with the HESS GC observations for two-body standard model particle final states and gauge-boson mediated four-lepton final states, when also including the constraints for Fermi-LAT observations toward local dwarf galaxies. Importantly, the HESS limits presented here for XDM are more constraining than the thermal relic density, CMB, self-interaction bounds, and naturalness bounds.

2.2 Data Analysis

The data used in this paper comes from the HESS collaboration analysis of the GC from Ref. [33]. The events analyzed are those from 112 hours of live time from the HESS very-high energy gamma-ray instrument with zenith angles smaller than 30° which were within the central 4° of the HESS field-of-view. Contamination of the dark matter signal due to the Galactic plane is excluded by masking the regions with Galactic latitude $|b| < 0.3^\circ$ and an additional mask within 0.3° of the extended source HESS J1745–303 ($(b, \ell) = (-0.6^\circ, 358.71^\circ)$) [77].

The source region is defined by $0.02^\circ \times 0.02^\circ$ pixels that lie within 1° of the GC, do not lie within the mask, and have a well-defined background. The background region is determined by choosing a telescope pointing position within 1.5° of the GC and rotating each pixel in the source region (with masked pixels removed) by 90°,

180°, and 270° about the telescope pointing position. Any of these pixels which is further than 1° from the GC and does not lie within the mask is considered background. Pixels within the inner 1° for which there are no corresponding background pixels are excluded from the analysis. This process was then repeated for multiple telescope pointing positions, calculating the differential flux in both the background and source regions. For additional details on the HESS GC analysis, see Ref. [33].

2.3 Dark Matter Annihilation Limits from the HESS GC Observations

2.3.1 Gamma-Ray Emission from Annihilating Dark Matter

A robust calculation of the expected final state radiation from dark matter annihilation requires accurate quantification of the dark matter source as well as the products in the final state gamma-ray radiation chain. The differential flux per solid angle for a dark matter candidate with cross-section $\langle \sigma_{\rm A} v \rangle$ over a solid angle $\Delta\Omega$ is

$$\frac{dF}{dE} = \frac{\langle \sigma_{\rm A} v \rangle}{2} \frac{J_{\Delta\Omega}}{J_0} \frac{1}{4\pi M_\chi^2} \frac{dN_\gamma}{dE} \ , \tag{2.1}$$

where dN_γ/dE is the gamma-ray spectrum per annihilation and M_χ is the dark matter particle mass. The integrated mass density squared along line-of-sight x, averaged over the solid angle of the observation region $\Delta\Omega$ is defined as

$$J_{\Delta\Omega} = \frac{J_0}{\Delta\Omega} \int_{\Delta\Omega} d\,\Omega \int d\,x \ \rho^2(r_{\rm gal}(b, \ell, x)) \ , \tag{2.2}$$

where distance from the GC is given by

$$r_{\rm gal}(b,\ell,x) = \sqrt{R_\odot^2 - 2xR_\odot\cos(\ell)\cos(b) + x^2}\ . \tag{2.3}$$

A normalization constant $J_0 \equiv 1/\left[8.5\ {\rm kpc}(0.3\ {\rm GeV\ cm^{-3}})^2\right]$ is chosen to make J dimensionless, but the final flux calculation is independent of the choice of J_0. The coordinates b and ℓ are the Galactic latitude and longitude, respectively. Following the HESS Collaboration, the dark matter profiles $\rho(r)$ we choose are the non-adiabatically-contracted Einasto and NFW models of Ref. [78] with the local dark matter density $\rho_\odot \equiv 0.389$ GeV cm^{-3} (0.385 GeV cm^{-3}) for an NFW (Einasto) profile [26]. Since there were several telescope pointing positions not given explicitly in Ref. [33], we cannot and did not independently calculate $\bar{J}_{\,\Delta\Omega}$ but adopt those of the HESS Collaboration. Importantly, as discussed in the introduction and in the HESS Collaboration study, in the case of a cored-isothermal or Burkert profile with a constant-density core that extends at or beyond $\sim$450 pc, then the background subtraction region would have an identical annihilation signal as the signal region, and no constraint can be placed on dark matter annihilation by this method. We have checked that the J-values for the single pointing shown in figure 2 of Ref. [33] are approximately their $\bar{J}$'s. Averaging over telescope pointing positions, the HESS analysis calculated the dark matter J-values for the source ($\bar{J}_{\rm s}$) and background

($\bar{J}_{\rm b}$) regions using the NFW and Einasto profiles [33]:

$$\bar{J}_{\rm s}^{\rm NFW} = 1604 \tag{2.4}$$

$$\bar{J}_{\rm b}^{\rm NFW} = 697 \tag{2.5}$$

$$\bar{J}_{\rm s}^{\rm Einasto} = 3142 \tag{2.6}$$

$$\bar{J}_{\rm b}^{\rm Einasto} = 1535 \ . \tag{2.7}$$

Note that toward the GC we adopt zero astrophysical substructure boost. However, there may be a substructure contribution to the flux of order 4% to 0.04% in the inner $\sim 1^\circ$ view of the GC [79].

2.3.2 Calculation of Dark Matter Spectra

To calculate the photon spectrum for a particular WIMP annihilation channel, we use PYTHIA 6.4 to simulate the photon radiation of charged particles as well as decays of particles such as the π^0 [10]. Specifically, we run PYTHIA to simulate an e^+e^- collision at a center of mass energy of $2M_\chi$ through a Z' to a final state that corresponds to the annihilation products of the dark matter. For WIMP annihilation to final states through light gauge bosons (such as the $4e$ and 4μ channels) we have the Z' decay into two scalar (H_0) states, each of which annihilates into two leptons. For the XDM case, we employ a light gauge boson which has branching fraction to e^+e^-, $\mu^+\mu^-$, and $\pi^+\pi^-$ set by the particular XDM model. For the models with light gauge bosons, photons can only be radiated at fairly low energy in the gauge boson rest frame. Therefore, in the center-of-mass frame of the dark matter annihilation, the average number of hard photons is significantly reduced in comparison to direct

annihilation to a two-body standard model final state.

We turn off initial state radiation such that all photons only come from the radiation or decay of the dark matter annihilation products. We turn on the decays of particles which are not decayed with the default PYTHIA settings, namely muons, charged pions, and charged kaons. Additionally, we turn on the muon decay channel $\mu^- \to e^- \nu_\mu \bar{\nu}_e \gamma$, with the standard branching fraction of 0.014 [27]. Using a large sample of events for each final state and each value of M_χ, the number of photons in the final state in a given logarithmic energy bin is counted and averaged over the number of events, yielding the average number of photons in that energy bin per annihilation event.

For WIMP annihilation to final states through extremely light gauge bosons ($m_\phi \lesssim 0.5$ GeV), the PYTHIA calculation becomes impractical due to low-energy cutoffs for radiation processes. For such annihilation channels (with $m_\phi = 0.25$ GeV and $m_\phi = 0.35$ GeV) we instead use the analytic formulae given in Appendix A of Ref. [80]. For the $4e$ state, all photons come from radiation off the final electrons and positrons. For the 4μ state, photons come from radiation off the final electrons and positrons as well as the radiation from the muons before they decay. We have verified the analytic spectra model by comparison to PYTHIA spectra for heavier gauge bosons.

2.3.3 Limits on the Dark Matter Annihilation Cross-Section

Figure 3 of Ref. [33] shows the observed source and background fluxes in 35 energy bins from 0.28 to 31 TeV. The two regions are consistent with each other, with zero difference in flux having a $\chi^2/\mathrm{DOF} = 0.75$. Therefore, any dark matter signal must be small enough that the source region does not have appreciably greater gamma-ray flux, within errors, than the background region. Figure 2.1 illustrates the difference between the lack of a dark matter signal from HESS and two representative dark matter signals. Using the dark matter J-values from Eqs. 2.4–2.7, we have derived 95% one-sided confidence-level (CL) (corresponding with a 90% two-sided CL) constraints on the dark matter cross-section as a function of mass for several key annihilation channels, using the total χ^2 in all bins.

In the figures, the light blue cross-hatched region is excluded at 95% CL for both the NFW and Einasto dark matter profiles. The singly-hatched light blue regions are excluded at 95% CL for the Einasto profile but not for the more conservative NFW profile. The purple regions are the 95% CL limits from a combined analysis of ten dwarf spheroidal galaxies from the Fermi-LAT Collaboration [44]. In particular, note that in figure 2.2(a) and figure 2.3(b) we have extended the mass of the dark matter down to 10 GeV in order to show the exclusion of a standard thermal relic below 27 GeV (37 GeV) for the $b\bar{b}$ ($\tau^+\tau^-$) annihilation channel by the Fermi-LAT stacked analysis of dwarf galaxies [44]. The dark pink regions represent the annihilation cross-section for a thermal relic, $\langle \sigma_{\mathrm{A}} v \rangle \approx 3 \times 10^{-26}$ cm^3 s^{-1}. The dark matter constraints for the standard WIMP annihilation channels $b\bar{b}$, $t\bar{t}$, and W^+W^-

are shown in figure 2.2. We show the $t\bar{t}$ channel since this should dominate for high mass dark matter ($M_\chi \gtrsim 200$ GeV). Our $b\bar{b}$ constraints are consistent with the quark channel limits from HESS [33]. As a comparison to the thermal cross-section, figure 2.2(c) also includes the expected cross-section for a non-thermal wino-like neutralino (the dashed red line) [81].

Figure 2.3 shows the dark matter limits for dark matter annihilating directly into leptons, whereas in figure 2.4, the dark matter annihilates into two gauge bosons ϕ of mass $m_\phi = 0.25$ GeV which then decay into leptons. (Note that the $4e$ case requires an *ad hoc* requirement of gauge boson decay into electrons and not muons. Neither the constraints nor signals would be significantly different in the case of, e.g., $m_\phi = 0.2$ GeV, where annihilation to e^+e^- would be energetically required.) Heavy dark matter masses annihilating primarily into leptons are particularly interesting in the context of the PAMELA positron excess [46] and the e^+e^- feature seen by the Fermi-LAT [50]. Such leptonic annihilation channels with a cross-section much larger than that of a thermal relic have been studied as the source of these anomalies [41, 51]. In figures 2.3 and 2.4 we have included one dark matter annihilation interpretation of the PAMELA excess in light pink and the analogous interpretation of the Fermi-LAT feature in red [41]. Recent analysis of the positron fraction by the Fermi-LAT Collaboration consistent with the PAMELA excess continues to rise up to energies of 180 GeV bin center energy, ruling out PAMELA regions below $M_\chi \approx 160$ GeV from being consistent with dark matter annihilation [53]. In figures 2.3(a) and 2.4(b) we include fits to the interpretation of the PAMELA excess in light green outline and the Fermi-LAT e^+e^- feature in dark green outline from

Ref. [51]. In panel 2.4(b), for the NFW profile case, we exemplify the strength of the limit by plotting the 95%, 99.7%, and 99.9999% CL limits as dashed, dot-dashed and solid lines, respectively.

In figure 2.5 three benchmark XDM models which are consistent with a combination of the PAMELA signal and the Fermi-LAT feature are shown, with red representing the 68% CL region and light pink representing the 95% CL region. Figure 2.5(a) contains the regions for annihilations which go 50% into e^+e^- and 50% into $\mu^+\mu^-$ through two intermediate gauge bosons of mass $m_\phi = 0.35$ GeV; figure 2.5(b) contains the regions for annihilations which go 33% into e^+e^-, 33% into $\mu^+\mu^-$, and 33% into $\pi^+\pi^-$ through two intermediate gauge bosons of mass $m_\phi = 0.58$ GeV; and figure 2.5(c) contains the regions for annihilations which go 25% into e^+e^-, 25% into $\mu^+\mu^-$, and 50% into $\pi^+\pi^-$ through two intermediate gauge bosons of mass $m_\phi = 0.90$ GeV.

When comparing to signal-fit regions from other work, a scaling of $\rho_0^2/\rho_\odot^2$ has been done to normalize that work's local dark matter density ρ_0 to the one adopted here. In the literature, signals for the PAMELA and Fermi-LAT excesses are ascribed boost factors for dark matter annihilation that can include both astrophysical substructure boosts and particle physics boosts, as well as the enhancement of latter due to the former. The local boost can be separated as $B_{\rm local} = B_s B_p$ into the substructure boost B_s and the particle boost B_p (when ignoring the enhancement of the latter to the former). To be clear and conservative, we employ a relatively strong local substructure boost, $B_s = 1.57$, using that expected from unresolved substructure calibrated to the Via Lactea II simulations [31, 82]. We incorporate

the fit regions from Ref. [51] such that

$$E_F = \left(\frac{\rho_\odot}{0.3 \text{ GeV cm}^{-3}}\right)^2 B_s B_p \ . \tag{2.8}$$

Both $B_{\rm local}$ and E_F designate the scaling factor from $\langle \sigma_{\rm A} v \rangle = 3 \times 10^{-26}$ cm^3 s^{-1}, as shown in our figures.

Relative boosts between the GC and local effects can alter the relative constraints between the annihilation in the GC versus local cosmic ray signals in Sommerfeld-enhanced annihilation models, where Sommerfeld-enhancement is greater in low-velocity substructures. As discussed in Ref. [67], the boost toward the GC relative to the local is

$$\frac{B_{\rm GC}}{B_{\rm local}} = \frac{S_{v(r=0)}/S_{v\sim 150 \text{ km/s}}}{1 + (S_{v\to 0}/S_{v\sim 150 \text{ km/s}})\Delta(8.5 \text{ kpc})}, \tag{2.9}$$

where S is the Sommerfeld-enhancement in a given model at a distance r from the GC, for a given velocity dispersion of the dark matter v. Here, $\Delta \equiv 1 - B_s$, which we take to be $\Delta(8.5 \text{ kpc} = 0.57$.

For specificity, we adopt $m_\phi = 0.25$ GeV, which corresponds to $S_{v\to 0}/S_{v\sim 150 \text{ km/s}} \approx 5$, from figure 1 of Ref. [67]. This model is a $4e$ channel case shown in figure 2.4(a). The purple rectangle shows the range of annihilation cross sections for a 1.2 TeV Sommerfeld-enhanced scenario consistent with the thermal relic density, the CMB, self-interaction bounds, and naturalness, for Δ from 10^{-4} to unity, corresponding to $B_{\rm local}$ from 30 to 300 [67]. The scaling of the signal toward the GC relative to the local boost is set explicitly by the local substructure boost Δ, and the value of $S_{v(r=0)}$, which is determined by the velocity dispersion of dark matter in the $\sim$450 pc of the HESS observation of the GC (and *not* exactly at $r = 0$).

It has been shown that the dark matter velocity rapidly decreases toward the GC in Milky Way scale halos [83], and the limit $v \to 0$ is potentially appropriate for $S_{v(r=0)}$, which we adopt in one case of our limits. In this GC low velocity limit case, one can take the substructure dominant versus subdominant cases:

$$\frac{B_{\rm GC}(v \to 0)}{B_{\rm local}} \approx \begin{cases} 5 & (\Delta = 10^{-4}), \\ 0.83 & (\Delta = 1). \end{cases} \tag{2.10}$$

Baryonic effects have been found to enhance the velocity of the dark matter toward the GC to make it comparable or greater than to that at the solar distance [19, 84], such that $S_{v(r=0)} \approx S_{v\sim 150 \text{ km/s}}$ [85], and in that scenario the substructure limiting cases are:

$$\frac{B_{\rm GC}(v \sim 150 \text{ km s}^{-1})}{B_{\rm local}} \approx \begin{cases} 1 & (\Delta = 10^{-4}), \\ 0.17 & (\Delta = 1). \end{cases} \tag{2.11}$$

We designate these ranges of constraints as bars and arrows for the corresponding four cases in figure 2.4(a), with the $v \to 0$ GC in green and $v \sim 150$ km s^{-1} GC in dark blue.

Ref. [67] claims that $\Delta(8.5 \text{ kpc})/\Delta(r = 0) \sim 20$ is relevant for the comparative constraints between the GC and the local boost, which strictly is only the case for strong local substructure domination and high velocities in the GC. More generally, it is Eq. (2.9) and the local substructure boost that sets the scaling, and is what we adopt. Note that any substructure in the dark matter of the GC region would enhance the constraints here. We ignore this enhancement to be conservative, i.e., we only include the annihilation from the smooth component in the GC region.

2.3.4 Discussion

For the $b\bar{b}$ annihilation channel (figure 2.2(a)), the HESS GC constraints are stronger than the constraints from the Fermi-LAT analysis of dwarf spheroidal galaxies for $M_\chi \gtrsim 900$ GeV when adopting a non-cored Einasto or NFW dark matter profile. The limits on this channel for an Einasto dark matter profile are within an order of magnitude of the thermal cross-section for 2 TeV $\lesssim M_\chi \lesssim$ 5 TeV. Similarly, the W^+W^- annihilation channel (figure 2.2(c)) has stronger constraints than the Fermi-LAT dwarfs for $M_\chi \gtrsim 800$ GeV and limits $\langle \sigma_{\rm A} v \rangle \leq 3 \times 10^{-25}$ cm^3 s^{-1} for 1 TeV $< M_\chi <$ 6 TeV. The $t\bar{t}$ annihilation channel (figure 2.2(b)) has somewhat weaker constraints, limiting $\langle \sigma_{\rm A} v \rangle \leq 5 \times 10^{-25}$ cm^3 s^{-1} for 2 TeV $< M_\chi <$ 10 TeV.

The light pink PAMELA excess region of Ref. [41] and the light green PAMELA excess region of Ref. [51] are both excluded above $M_\chi \sim 400$ GeV by the HESS GC data for the $\mu^+\mu^-$ annihilation channel (figure 2.3(a)) when adopting a non-cored Einasto or NFW halo model. Also for the $\mu^+\mu^-$ channel, the red Fermi-LAT feature region of Ref. [41] and the dark green Fermi-LAT feature region of Ref. [51] are excluded by the HESS GC data when adopting either halo model.

In the $\tau^+\tau^-$ annihilation channel (figure 2.2(b)), the HESS GC observation excludes a cross-section of $\langle \sigma_{\rm A} v \rangle > 4 \times 10^{-26}$ cm^3 s^{-1} for a dark matter mass $M_\chi \approx 1$ TeV, when adopting an Einasto profile, within a factor of $\sim$2 of the thermal cross-section. The HESS GC excludes the light pink PAMELA excess region above $M_\chi \approx 400$ GeV and the Fermi-LAT dwarf analysis excludes the $\tau^+\tau^-$ channel below $M_\chi \approx 400$ GeV, so this model for the PAMELA excess has been ruled out at all dark

matter masses when adopting an NFW profile. The red Fermi-LAT feature region is also excluded, at greater than 99.9999% CL, in the $\tau^+\tau^-$ channel for both the Einasto and NFW dark matter profiles, consistent with previous results [36, 38, 41].

For the $4e$ annihilation channel (figure 2.4(a)), the HESS GC observation constrains the light pink PAMELA excess region of Ref. [41] above $M_\chi \approx 600$ GeV for the Einasto halo model, and is constrained above $M_\chi \approx 500$ GeV for the NFW halo model. Similarly, the 4μ annihilation channel (figure 2.4(b)) has both the light pink region and the light green PAMELA excess region of Ref. [51] constrained above $M_\chi \approx 1.5$ TeV for the Einasto halo model, and above $M_\chi \approx 3$ TeV for the NFW halo model.

In the $4e$ channel (figure 2.4(a)), the purple rectangle shows the range of boost factors for a 1.2 TeV Sommerfeld-enhanced model consistent with the thermal relic density, the CMB, self-interaction bounds, and naturalness, for Δ conservatively from 10^{-4} to unity [67]. Note that the gamma-ray annihilation constraints from the HESS GC on the annihilation cross-section and boost factor, when adopting an NFW or Einasto profile, is often stronger than those from the thermal relic density, the CMB, self-interaction bounds, and naturalness considerations. Specifically, the limits to boosts toward the GC are $B_{\rm GC} \lesssim 27$, which for the comparable central velocity case excludes models with local substructure $\Delta \lesssim 0.025$ (0.17) for $B_{\rm local} = 30$ (50). Our canonical case for $\Delta \approx 0.57$, with GC dark matter velocities comparable to that locally, is unconstrained at 95% CL. Note that any substructure within the inner degree of the HESS GC observation would further enhance these limits due to the corresponding Sommerfeld-enhancement saturation in the GC substructure.

The substructure boost in the inner degree has been seen in simulations at the level of $\Delta(r \sim 0.15 \text{ kpc}) \sim 4 \times 10^{-2}$ to 4×10^{-4} [79].

The XDM annihilation models: $\text{Br}(e^+e^-) = \text{Br}(\mu^+\mu^-) = 0.5$, $m_\phi = 0.35$ GeV (figure 2.5(a)); $\text{Br}(e^+e^-) = \text{Br}(\mu^+\mu^-) = \text{Br}(\pi^+\pi^-) = 0.33$, $m_\phi = 0.58$ GeV (figure 2.5(b)) ; and, $\text{Br}(e^+e^-) = \text{Br}(\mu^+\mu^-) = 0.25$,$\text{Br}(\pi^+\pi^-) = 0.5$, $m_\phi = 0.90$ GeV (figure 2.5(c)) are excluded at greater than 95% CL when adopting an Einasto halo profile. However, when adopting an NFW halo profile, these XDM models have a region from 0.8 TeV $\lesssim M_\chi \lesssim$ 1 TeV below $\langle \sigma_\text{A} v \rangle \sim 1.8 \times 10^{-24}$ cm^3 s^{-1} which remains consistent at 95% CL.

2.4 Conclusions

The HESS telescope's observations toward the Galactic center present the strongest constraints on WIMP dark matter annihilation into Standard Model particles for $M_\chi \gtrsim 900$ GeV, given a non-adiabatically-contracted NFW or Einasto profile for the Milky Way dark matter profile. As discussed in the introduction, the HESS GC observation is not sensitive to dark matter annihilation for large constant-density cored dark matter profiles. If such profiles are established to be valid in the Milky Way, the HESS GC observation provides no empirical constraint in these cases given the background subtraction method. If adiabatic contraction and steepening of the dark matter density profile is well established, then the constraints could become stronger. We find that constraints on annihilation into $b\bar{b}$ final states comes within an order of magnitude of the canonical thermal cross section, while $t\bar{t}$

is within a factor of ∼20. The $\tau^+\tau^-$ channel is within a factor of ∼2 of the thermal cross-section. This bodes well for the future Čerenkov Telescope Array's potential impact at constraining canonical thermal WIMP dark matter this mass scale [86].

We also examine constraints on Sommerfeld-enhanced dark matter annihilation models which produce the PAMELA positron excess and Fermi-LAT e^+e^- spectral feature, including XDM. The models with pure leptonic modes $\tau^+\tau^-$ and $4e$ are excluded at greater than 95% CL by the HESS GC when adopting NFW or Einasto dark matter halo profiles. For other cases, (e.g. 4μ, $2e2\mu$, $e^+e^-\mu^+\mu^-\pi^+\pi^-$), the models are in tension with the HESS GC observations, with portions of the signal 95% CL parameter space are excluded at the 95% CL level. Significantly, the exclusions presented here from HESS GC gamma-ray observations on Sommerfeld-enhanced upper boosts are more constraining, in many cases, than prior constraints from diffuse gamma-rays [31, 68], relic density considerations [58–62], the CMB [62–65], halo shapes [58, 60], and naturalness [66, 67]. In the case where the velocity dispersion of dark matter in the center of the Galaxy is comparable to that locally, the supplemental Sommerfeld-enhancement from local substructure and not at the GC weakens the constraints in certain models.

Gamma-ray astronomy has produced the most stringent constraints on the canonical thermal WIMP model's annihilation cross-section, with Fermi-LAT's stacked observations of dwarf galaxies being the most constraining at low masses, and HESS's observations of the Galactic center being the most constraining at higher masses. With further observation and new technologies, the nature of dark matter may be revealed by gamma-ray telescopes.

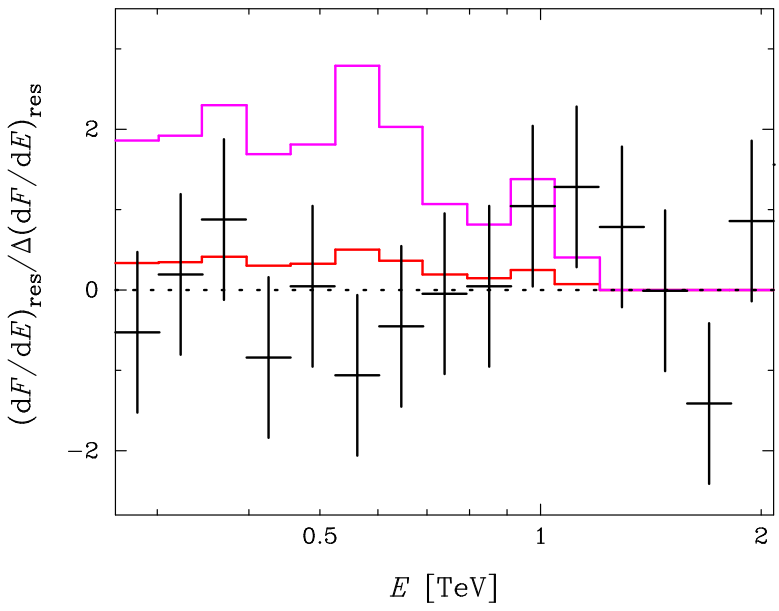

Figure 2.1: Shown are the data from the HESS GC observation, for which the signal and background are consistent with no difference in flux at the level of $\chi^2/\mathrm{DOF} = 0.75$. For comparison, two possible dark matter signals are shown as well. Both dark matter signals are for a 1.2 TeV WIMP annihilating via 0.25 GeV gauge bosons into two e^+e^- pairs, for an NFW halo profile. The red (lower) histogram is the signal expected for a dark matter cross-section $\langle\sigma_{\mathrm{A}}v\rangle = 9 \times 10^{-25}$ cm^3 s^{-1}, which has a total $\Delta\chi^2 = 2.79$. The magenta (upper) histogram is the signal expected for a dark matter cross-section $\langle\sigma_{\mathrm{A}}v\rangle = 5 \times 10^{-24}$ cm^3 s^{-1} and mass $M_\chi = 1.2$ TeV, with a $\Delta\chi^2 = 41.2$. These signals correspond with the upper end of the red Fermi-LAT plus PAMELA region, and lower end of the purple rectangle in figure 2.4(a), in the case of assuming a subdominant substructure contribution, and are excluded at greater than 95% CL. Note that the HESS GC observation extends to higher energies than shown here.

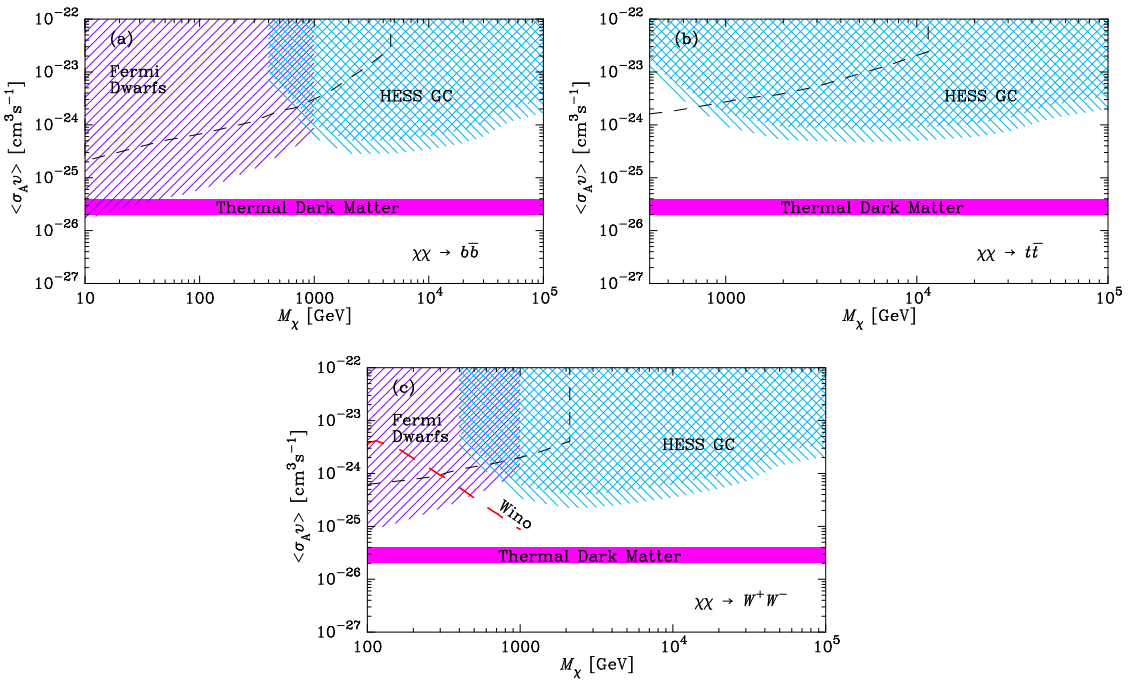

Figure 2.2: Shown are the constraints on dark matter in three canonical annihilation channels: (a) $b\bar{b}$; (b) $t\bar{t}$; (c) W^+W^-. The regions are labeled according to their constraining observations as described in the text: "HESS GC" are the 95% CL limits from the HESS analysis of the GC. The double hatched region is constrained for both the Einasto and NFW halo models, and the single hatched region is constrained for only the Einasto halo model. The regions labeled "Fermi Dwarfs" are the 95% CL limits from the Fermi-LAT collaboration analysis of dwarf spheroidals. In the W^+W^- channel, panel (c), the mass for a non-thermal wino-like neutralino is shown as a thick-dashed red line [81]. For comparison, we plot the 3σ limits from Ref. [69] for their analysis of the Fermi-LAT observation of the $3^\circ \times 3^\circ$ region around the Galactic Center as dashed (black) lines in all panels for the respective channels.

Figure 2.3: Shown on the following page are the constraints on dark matter in two leptonic annihilation channels: (a) $\mu^+\mu^-$; (b) $\tau^+\tau^-$. The regions are labeled according to their constraining observations as described in the text: "HESS GC" are the 95% CL limits from the HESS analysis of the GC. The double hatched region is constrained for both the Einasto and NFW halo models, and the single hatched region is constrained for only the Einasto halo model. The regions labeled "Fermi Dwarfs" are the 95% CL limits from the Fermi-LAT collaboration analysis of dwarf spheroidals. The light pink shaded region is consistent with a dark matter interpretation of the PAMELA signal and the dark red shaded region is that from the Fermi-LAT e^+e^- feature from Ref. [41]. In the $\mu^+\mu^-$ channel, panel (a), the light green outlined region is consistent with a dark matter interpretation of the PAMELA signal and the dark green outlined region with that of the Fermi-LAT e^+e^- feature from Ref. [51]. PAMELA regions below $M_\chi = 160$ GeV are ruled out by the rise in the positron fraction seen by the Fermi-LAT [53]. In panel (b), to illustrate the strength of the HESS GC limits, we show for the NFW profile the 95%, 99.7% and 99.9999% CL limits in dotted, dot-dashed and solid lines, respectively. For comparison, we plot the 3σ limits from Ref. [69] for their analysis of prompt and inverse-Compton emission in the Fermi-LAT observation of the $3^\circ \times 3^\circ$ region around the Galactic Center as dashed (black) lines in both panels for the respective channels.

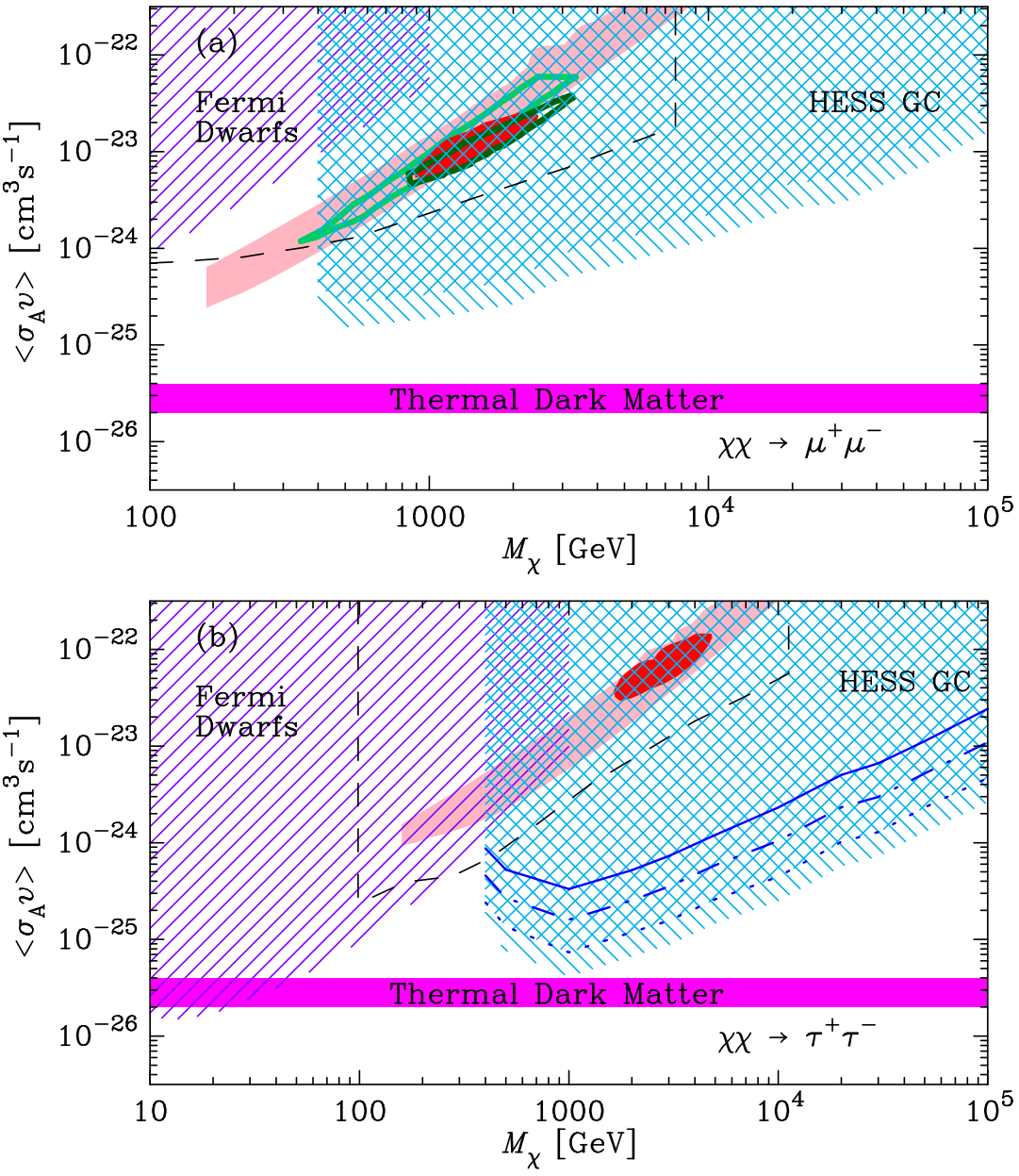
(a)
Fermi
Dwarfs
HESS GC
Thermal Dark Matter
$\chi\chi \to \mu^+\mu^-$
$<\sigma_A v>$ [cm^{3}s^{-1}]
M_χ [GeV]
(b)
Fermi
Dwarfs
HESS GC
Thermal Dark Matter
$\chi\chi \to \tau^+\tau^-$
$<\sigma_A v>$ [cm^{3}s^{-1}]
M_χ [GeV]

Figure 2.4: Shown on the following page are the constraints on dark matter in two annihilation channels: (a) annihilation into two e^+e^- pairs via two intermediate 0.25 GeV gauge bosons ϕ (note that this case requires an *ad hoc* requirement of decay into electrons and not muons); (b) annihilation into two μ^+ and two μ^- via two intermediate 0.25 GeV gauge bosons ϕ. The regions are labeled according to their constraining observations as described in the text: "HESS GC" are the 95% CL limits from the HESS analysis of the GC. The double hatched region is constrained for both the Einasto and NFW halo models, and the single hatched region is constrained for only the Einasto halo model. The light pink shaded region is consistent with a dark matter interpretation of the PAMELA signal and the dark red shaded region is that of the Fermi-LAT e^+e^- feature from Ref. [41]. In the $4e$ channel, panel (a), the purple rectangle demonstrates the range of Sommerfeld-enhanced cross-sections consistent with constraints from thermal relic density, the CMB, self-interaction bounds, and naturalness [67]. The green (blue) bars and arrows show the HESS GC limits for the two cases of velocity dispersions of $v \to 0$ ($v \sim 150$ km s^{-1}), respectively, with the upper and lower bars for each color representing the two local substructure boost limits, as described in the text. In the 4μ channel, panel (b), the light green outlined region is consistent with a dark matter interpretation of the PAMELA signal and the dark green outlined region is that for Fermi-LAT e^+e^- feature from Ref. [51]. PAMELA regions below $M_\chi \approx 160$ GeV are ruled out by the rise in the positron fraction seen by the Fermi-LAT [53].

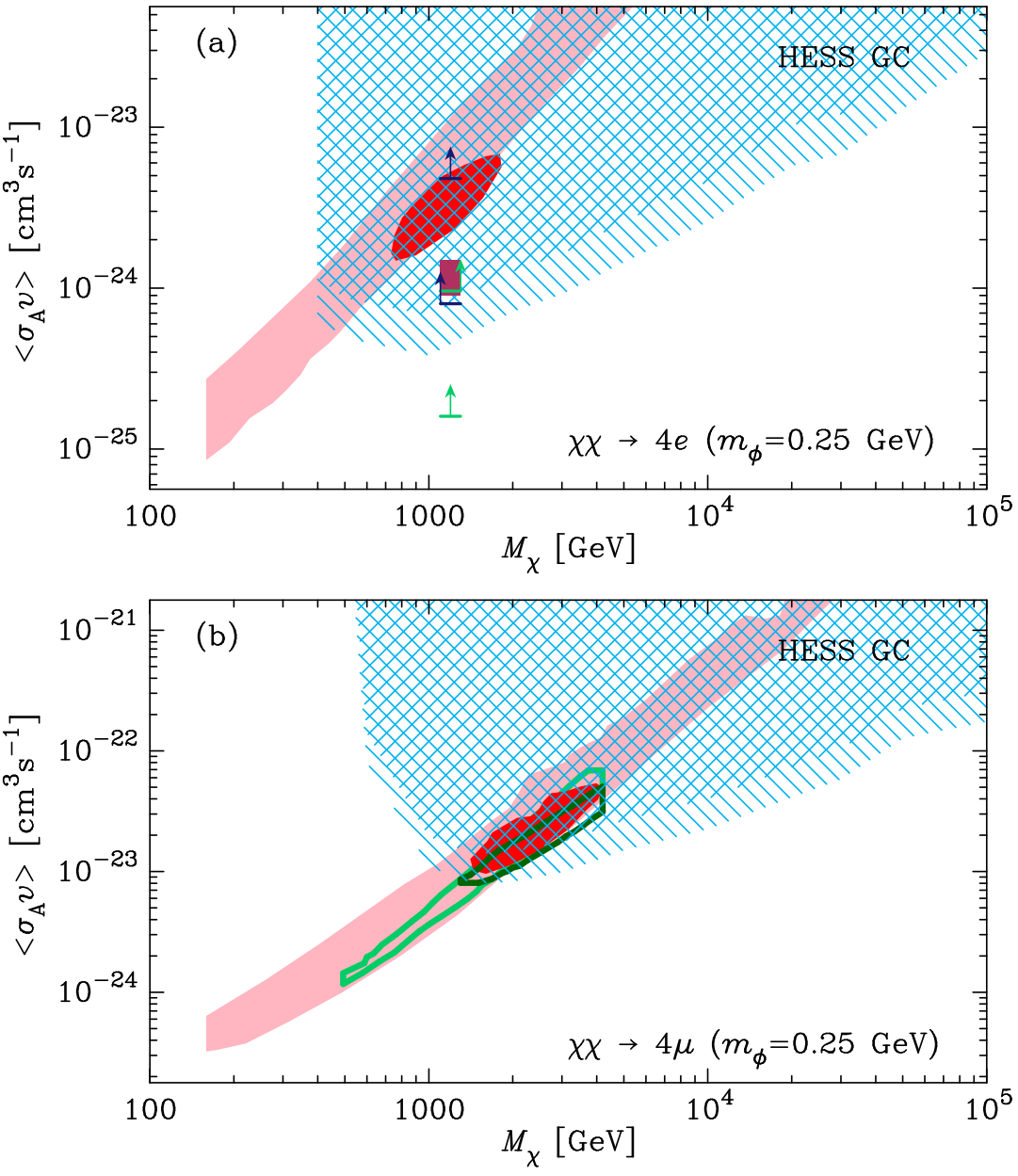
(a)
HESS GC
$\chi\chi \rightarrow 4e$ (m_ϕ=0.25 GeV)
$<\sigma_A v>$ [cm^{3}s^{-1}]
10^{-23}
10^{-24}
10^{-25}
100
1000
10^4
10^5
M_χ [GeV]
(b)
HESS GC
$\chi\chi \rightarrow 4\mu$ (m_ϕ=0.25 GeV)
$<\sigma_A v>$ [cm^{3}s^{-1}]
10^{-21}
10^{-22}
10^{-23}
10^{-24}
100
1000
10^4
10^5
M_χ [GeV]

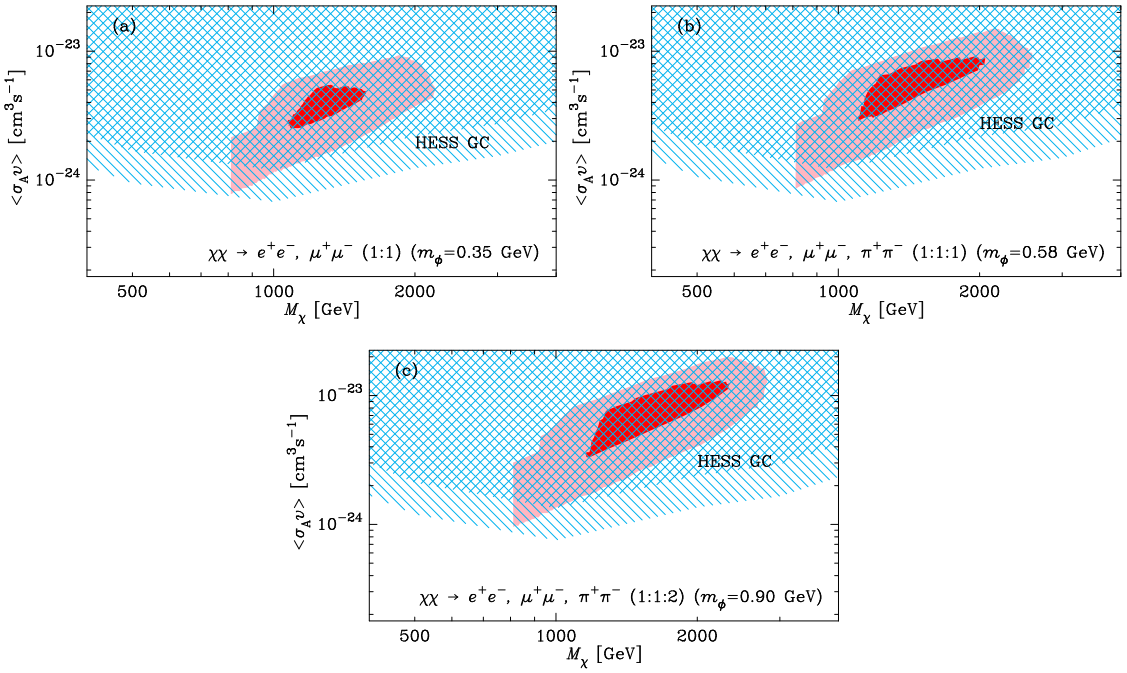

Figure 2.5: Shown are the constraints on dark matter in three XDM annihilation cases: (a) annihilation into 50% e^+e^- and 50% $\mu^+\mu^-$ via two intermediate 0.35 GeV gauge bosons ϕ; (b) annihilation into 33% e^+e^-, 33% $\mu^+\mu^-$, and 33% $\pi^+\pi^-$ via two intermediate 0.58 GeV gauge bosons ϕ; (c) annihilation into 25% e^+e^-, 25% $\mu^+\mu^-$, and 50% $\pi^+\pi^-$ via two intermediate 0.90 GeV gauge bosons ϕ. The regions are labeled according to their constraining observations as described in the text: "HESS GC" are the 95% CL limits from the HESS analysis of the GC. The double hatched region is constrained for both the Einasto and NFW halo models, and the single hatched region is constrained for only the Einasto halo model. The light pink and dark red shaded regions are the 68% and 95% CL regions consistent with the XDM dark matter interpretation of a combination of the PAMELA signal and the Fermi-LAT e^+e^- feature from Ref. [66].

Chapter 3

Morphological Tests of the Pulsar and Dark Matter Interpretations of the WMAP Haze

3.1 Introduction

The Wilkinson Microwave Anisotropy Probe (WMAP) has provided a detailed map of the cosmic microwave background (CMB) as well as the foreground from our Galaxy [87, 88]. The foreground emission from the center of the Galaxy shows an excess of emission in the inner $5 - 20^{\circ}$ around the Galactic center. This excess of microwave emission is known as the "WMAP haze" [89]. Due to the Galactic plane, the current data on the haze only goes down to about 6 degrees from the Galactic center. Two notable features of the haze are the approximate spherical symmetry and the strong angular dependence of the flux. In particular, the flux increases quickly toward the Galactic center.

The size and shape of the haze is currently not well constrained. Using a different foreground model may change the look of the haze slightly. For instance, Ref. [90] used a different synchrotron map to model the WMAP data and found that the haze in that case is smaller in spatial extent and slightly smaller in magnitude. A cleaner foreground subtraction is needed to further constrain the source of the haze. In this paper, we will use the measurement of the haze presented in Ref. [91].

An explanation for the WMAP haze is a previously unknown source of microwave emission. The frequency dependence of the haze is quite hard, so a hard source like synchrotron radiation is a likely candidate [91–93]. The magnetic field in the Galactic center tends to be tens of microgauss. Therefore, the synchrotron radiation from highly relativistic electrons and positrons near the Galactic center could be the source of the microwave signal [94]. Another possibility for the source of the haze was thermal bremsstrahlung from ionized gas [89]. However, the Hα skymap shows no significant increase in the regions where the haze is strongest. At high density and high temperature ($\sim 10^5$K) such a gas could still explain the haze, but the emission from such regions is constrained to be small, ruling it out as the source of the haze [95].

In the synchrotron emission interpretation, calculating the complete propagation of electrons in the interstellar medium requires the full diffusion-loss equation. This includes spatial diffusion of the e^+e^-, reacceleration of the particles due to momentum-space diffusion, energy loss due to several different mechanisms, convection of the particles in the Galaxy, and the particle source. To solve this complete equation, one may use the software GALPROP [96, 97]. However, the major necessary physical features of the source and synchrotron emission can be sufficiently modeled using a Green's function solution to the diffusion-loss equation, which we employ [98, 99].

The source of high energy electrons and positrons required for synchrotron emission remains a mystery [100]. One intriguing explanation of the haze is from dark matter annihilations in the Galactic center [93]. The e^+e^- produced from by

the annihilation products move through the Galactic magnetic field, creating the diffuse synchrotron emission [91]. This model matches the haze well, especially the strong angular dependence and approximate spherical symmetry.

It should be noted that Ref. [101] claims that dark matter annihilations cannot explain the haze because it would require too large of a clumpiness boost factor. In this work, we employ similar methods to those used in that paper and do not find that too large of a boost factor is necessary. Ref. [101] averaged the dark matter density over the direction perpendicular to the Galactic plane, which is inaccurate in light of the morphological effects we present below.

Another source for the haze is e^+e^- coming from the magnetosphere boundary of Galactic pulsars [102]. This type of emission from nearby pulsars can be the source of positrons in the PAMELA results [46, 103–106] and also the source of features seen by ATIC [105–107] and the Fermi Gamma-Ray Space Telescope [50, 108].

In this paper, we explore models of the WMAP haze in the context of synchrotron radiation from the electron and positron production of Galactic pulsars and dark matter annihilations. We will show tests of this diffuse synchrotron emission which could distinguish between the exotic explanation of dark matter annihilations and the astrophysical pulsar sources. We also show how haze observations can test pulsar and dark matter models separately. These tests can be done with upcoming results from the Planck Observatory, which has been shown, e.g. in Leach, et al. [109], to be expected to have a much smaller Galactic mask than WMAP [110, 111].

Recently, Kaplinghat et al. [102] showed that the morphology of the haze is different depending on the source. This work pointed out that for a source with spher-

ical symmetry, the haze should be slightly elliptically stretched along the Galactic plane while for a centrally-peaked pulsar source, the signal lies primarily along the Galactic plane and has less spherical symmetry.

In this work, we examine the morphological structure of the WMAP haze in detail. First, we consider the signal due to pulsars, both from a Gaussian distribution and one which vanishes at the Galactic center. Second, we look at dark matter annihilations models' sensitivity to the dark matter density profile. Lastly, we compare the pulsar and dark matter scenarios to quantitatively distinguish them from one another.

3.2 Calculation of Synchrotron Flux

To calculate the propagation of the electrons from their source, we must solve the diffusion-loss equation for e^+e^-: [98, 99]

$$\frac{\partial}{\partial t}\frac{dn}{d\epsilon} = \vec{\nabla}\cdot\left[K\left(\epsilon,\vec{x}\right)\vec{\nabla}\frac{dn}{d\epsilon}\right] + \frac{\partial}{\partial\epsilon}\left[b\left(\epsilon,\vec{x}\right)\frac{dn}{d\epsilon}\right] + Q\left(\epsilon,\vec{x}\right) \quad , \tag{3.1}$$

with K the diffusion constant, b the energy loss rate, Q the source term, and $\epsilon = E/\left(1\text{ GeV}\right)$. This simplified diffusion-loss equation is derived from the full equation by assuming that reacceleration is small compared to spatial diffusion and that convection is small compared to the particle velocities. For highly relativistic e^+e^- in the Galaxy, these are both reasonable assumptions.

For the simplified diffusion-loss equation, we shall use the parameterization of Ref. [91]. We assume a spatially-independent diffusion constant $K\left(\epsilon\right) = 10^{28}\epsilon^{0.33}\text{ cm}^2\text{ s}^{-1}$ inside a "diffusion zone" of half-thickness 3 kpc away from

the Galactic plane and "large" in the radial direction of the Galactic plane. Outside this region, it is assumed that all particles are no longer confined to the Galactic magnetic field and therefore are free-streaming. Inside this region, the Galactic field is assumed to be a constant. This is a reasonable approximation because it is known that the Galactic magnetic field decreases quickly away from the Galactic center, but its exact profile is unknown. The energy loss rate is also assumed to be spatially-independent and is parameterized by $b(\epsilon) = \epsilon^2/\tau_E$ with $\tau_E = 2 \times 10^{15}$ s. This characteristic energy-loss time τ_E accounts for losses due to inverse Compton scattering on the CMB and starlight, as well as synchrotron energy losses. The source term $Q(E, \vec{x})$ is the rate of particles created per unit time per unit volume per unit energy. We will further assume that the diffusion-loss equation is in steady-state, so all terms are time-independent. The assumptions of spatial and temporal independence of the diffusion and loss parameters should be valid as long as we are concerned only with regions close to the Galactic center, so the average values of parameters can change only slightly in the time and distances involved. The assumption of time-independence in the source term assumes that the rate of pulsar formation and death is steady over the timescale of the electron propagation, during which only a few new pulsars should have formed.

For our parameters, an analytic solution to the diffusion-loss equation can be found using Green's function techniques [98, 99]. Writing the source term as $Q(E, \vec{x}) = f(E)g(\vec{x})$, this analytic solution is given by:

$$\frac{dn}{dE} = E^{-2} \int_E^\infty dE' f(E) \tau_D(E', E, \vec{x}) \ , \tag{3.2}$$

$$\tau_D(E', E, \vec{x}) = \tau_E\left(\pi D^2\right)^{3/2} \sum_{n=-\infty}^{\infty} (-1)^n \int_0^{\infty} ds' s' \int_{-L}^{L} dz' \tag{3.3}$$
$$\times \int_0^{2\pi} d\theta' g(s', z') \exp\left(-\frac{s^2 + s'^2}{D^2}\right)$$
$$\times \exp\left(\frac{2ss'\cos(\theta - \theta')}{D^2}\right) \exp\left(-\frac{(z - (-1)^n z' - 2nL)^2}{D^2}\right) \ ,$$

where $\vec{x} = (s, \theta, z)$ are cylindrical coordinates from the Galactic center, $L = 3$ kpc is the end of the diffusion zone and $D^2 = 8.4\,(\epsilon^{-0.67} - \epsilon'^{-0.67})$ kpc^2 is the integrated energy-dependent diffusion parameter. To convert this e^+e^- density to a synchrotron flux at earth, we must integrate over line-of-sight ℓ and then convolve it with the synchrotron spectrum for a single electron [99]:

$$\Phi\,(\alpha, \psi) = \frac{m_e^2 c^4}{4\pi \tau_{\rm syn} \nu_B} \int d\epsilon \int d\ell \frac{dn}{dE} \left(\frac{1}{P}\frac{dP}{dy}\right) \tag{3.4}$$

$$\frac{1}{P}\frac{dP}{dy} = \frac{27\sqrt{3}}{32\pi} y \int_0^{\pi} d\phi \sin(\phi) \int_{y/\sin(\phi)}^{\infty} K_{5/3}(x) dx \ . \tag{3.5}$$

Here, $\tau_{\rm syn} = 4\tau_E$ is the energy loss time due to synchrotron emission, ν is frequency, $y = (\nu m_e^2 c^4)/(\nu_B E^2)$, and $\nu_B = (3eB)/(4\pi m_e)$ is the characteristic synchrotron frequency. As in Ref. [91], we choose a constant magnetic field of 10 μG in the Galactic center and look primarily at the $\nu = 22$ GHz band of the haze. We will use a coordinate system where α is the angle out from the Galactic center and ψ is the angle up from the Galactic plane.

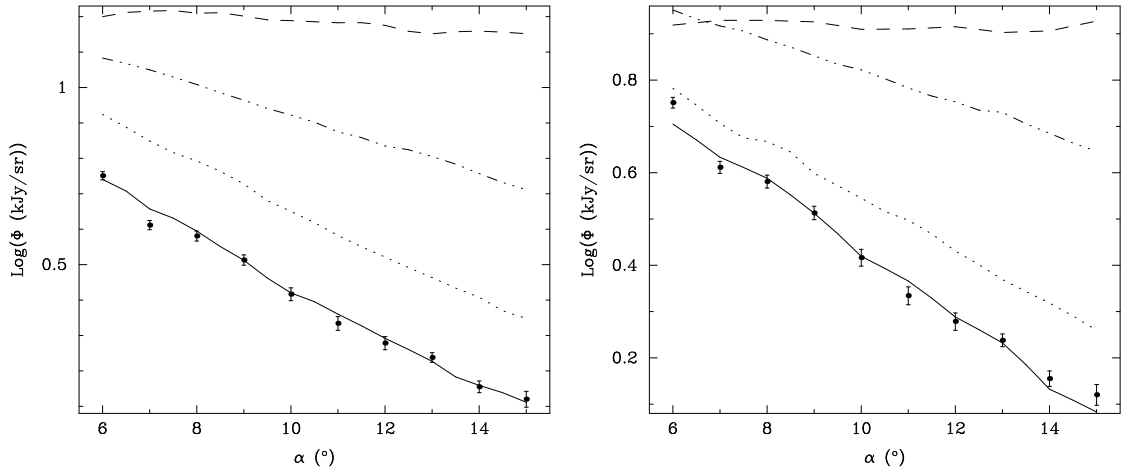

Figure 3.1: Angular flux profile Φ versus angle from the Galactic center α. The diagram on the left is for the Gaussian pulsar distribution and the diagram on the right is for the pulsar distribution with no pulsars at the Galactic center. From top to bottom, the lines are the $\psi = 0°$ (dashed), $\psi = 30°$ (dash-triple dotted), $\psi = 60°$ (dotted), and $\psi = 0°$ (solid) plot. The plots are scaled with the $\psi = 90°$ plot normalized to the flux of the WMAP haze. The points are the WMAP haze with errors from Ref. [91].

3.3 Electron Source Function

3.3.1 Source Function for Pulsars

In order to calculate the diffuse synchrotron flux Φ coming from pulsars, it is necessary to solve for the rate of e^+e^- produced per units energy, volume, and time. This can be separated into two parts, the rate of electron (and positron) production in a given pulsar, $d^2N/(dEdt)$, and the spatial distribution of the pulsars in the Galaxy $\rho(\vec{x})$.

For the number of electrons and positrons produced at a given energy in a given time, we use a model which does a fit to gamma-ray production from Galactic

pulsars to determine the e^+e^- rate from pulsars in the Galaxy [112]. Above about 1.5 GeV, this model is similar to the positron model in Ref. [113]. For the combined e^+e^- production rate, this model gives

$$\frac{d^2N}{dEdt} = \left(5.7 \times 10^{40}\ \mathrm{GeV}^{-1}\ \mathrm{s}^{-1}\right) f_e \dot{N}_{100} \left(\frac{E}{\mathrm{GeV}}\right)^{-1.6} \exp\left[-\frac{E}{80\ \mathrm{GeV}}\right] \quad , \qquad (3.6)$$

where f_e is the ratio of e^+e^- to photon production in mature pulsars and $\dot{N}_{100}$ is the rate of pulsar formation in the Galaxy per hundred years. The free parameters f_e and $\dot{N}_{100}$ are to account for the fact that the fit to gamma-ray pulsar data was done assuming a pulsar production rate of one per hundred years, so the overall normalization is unknown.

The distribution of pulsars in the Galaxy can be broken into two parts, a radial component $\rho_s(s)$ and a component against the Galactic plane $\rho_z(z)$. The full pulsar density is, then, $\rho(\vec{x}) = \rho_s(s)\,\rho_z(z)$. The perpendicular distribution ρ_z should be peaked about the Galactic plane to match pulsar surveys with $\rho_z(-z) = \rho_z(z)$. This has been parameterized as [114]

$$\rho_z(z) = \frac{1}{0.61\pi^{1/2}} \exp\left[-\left(\frac{z}{0.61\ \mathrm{kpc}}\right)^2\right]\ \mathrm{kpc}^{-1} \qquad (3.7)$$

with the normalization $\int_{-\infty}^{\infty} dz = 1$.

Because of observational bias in pulsar surveys, there is much model dependence in the shape of the radial distribution of pulsars ρ_s. For example, one must be careful in selection effects due to bright pulsars being more easily observable than dim ones. Also, in the inner part of the Galaxy, the pulsar distribution is largely unknown due to scattering and obscuration, so a targeted high-frequency radio survey would be needed to detect these innermost pulsars [115].

This ambiguity in models has lead to two distinct fits to the pulsar survey data: a Gaussian fit with a peak at the Galactic center or a Boltzmann-like distribution which goes to zero at the Galactic center. As evidence for the latter, the Effelsberg 5 GHz Galactic center survey has not found any pulsars towards the Galactic center, but it is possible that any survey below 10 GHz cannot avoid scattering and obscuration effects [116, 117]. If a large number of pulsars in the inner kiloparsecs are observed by the Fermi Gamma-Ray Space Telescope, it could distinguish between these two models as well [50].

The zero central density distribution is one in which the function peaks toward the Galactic center and then goes to zero at the center itself. This model is plausible if the pulsar distribution is similar to the distribution of supernova remnants and some astrophysical gas populations, which are in rings peaked about 4 kpc from the Galactic center [115, 118–120]. This model of the pulsar radial distribution can be parameterized as [117]

$$\rho_s^{0\mathrm{GC}}(s) = (376)^{-1} \left(\frac{s}{\mathrm{kpc}}\right)^{2.35} \exp\left[-\frac{s}{1.53\ \mathrm{kpc}}\right]\ \mathrm{kpc}^{-2}\ , \tag{3.8}$$

where s is the distance from the Galactic center in the Galactic plane (in kpc). This distribution has been normalized to unity using $2\pi \int_0^\infty \rho_s(s) s ds = 1$.

Another radial distribution of Galactic pulsars is Gaussian, with a peak at the Galactic center falling off in the outer Galaxy. This model is motivated by stellar evolution arguments where the distribution is expected to be more densely peaked near the Galactic center, following the stellar distribution in the Galaxy. Such a

radial distribution has been parameterized as [114]

$$\rho_s^{\rm Gauss}(s) = \frac{1}{64\pi} \exp\left[-\left(\frac{s}{8\ {\rm kpc}}\right)^2\right]\ {\rm kpc}^{-2}\ , \tag{3.9}$$

where s is the distance from the Galactic center in the Galactic plane. This distribution has been normalized to unity as the zero central density distribution was. An exponential fit like the one used by Ref. [102] can be modified to be indistinguishable from the Gaussian form [114].

3.3.2 Source Function for Dark Matter Annihilations

To compare the pulsar source scenario with dark matter ones, we consider two different Navarro-Frenk-White (NFW) [17] type dark matter profiles with WIMP annihilations. In this model, the relativistic e^+e^- are formed when dark matter particles annihilate in the Galactic dark matter halo. This can happen if the dark matter is its own antiparticle, as in the case of supersymmetric neutralinos [93]. For the halo shape, we use a generalization of the standard NFW profile [17]. The generalization can be written in the form

$$\rho = \frac{\rho_0}{(r/r_s)^\gamma (1 + r/r_s)^{3-\gamma}}\ , \tag{3.10}$$

for scale density ρ_0 and scale radius r_s. The original NFW profile has $\gamma = 1$. A slightly steeper profile with $\gamma = 1.2$ is also consistent with Milky-Way constraints [26, 121, 122]. We take $r_s = 25$ kpc as our canonical scale radius. The scale density is normalized to local earth dark matter density (~ 0.3 GeV/cm^3) [123]. A standard WIMP has a weak-interaction cross-section of $\langle \sigma v \rangle = 3 \times 10^{-26}$ cm^{3}s^{-1} [91,

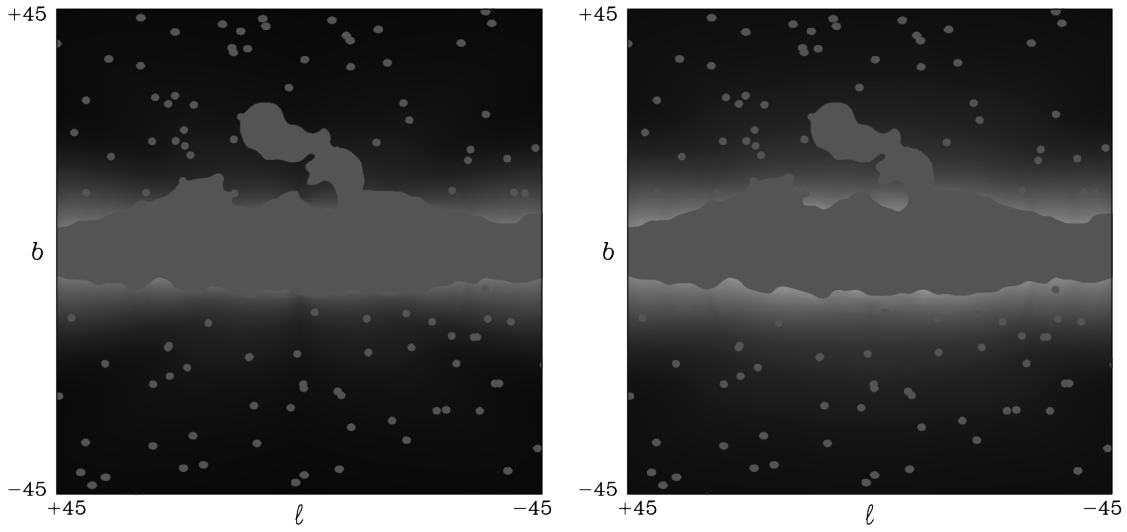

Figure 3.2: Relative flux Φ versus Galactic coordinates ℓ and b for the Gaussian pulsar profile (left) and the pulsar profile with no pulsars at the Galactic center (right). The mask is that from WMAP K-band mask Kp4 [125].

124]. For simplicity, we consider the direct annihilation channel where the product is exactly one positron and one electron with energy equal to the dark matter particle mass. We use 100 GeV dark matter particles as a canonical value. The morphological tests here are not sensitive to this choice. The source function for e^+e^- formed from such a dark matter annihilation is

$$Q(E,\vec{x})^{\rm DM} = \frac{\rho^2}{2M^2}\langle\sigma v\rangle 2\delta(E-M) \ . \tag{3.11}$$

3.4 Synchrotron Flux from Sources

3.4.1 Flux from Pulsars

For the standard pulsar distribution which increases toward the Galactic center, the e^+e^- source term is

$$Q(E, \vec{x}) = \frac{d^2N}{dEdt}\rho_z(z)\rho_s^{\text{Gauss}}(s) \ . \tag{3.12}$$

Using this with an overall scaling factor for the normalization of the particle production rate we find that the angular flux profile (Φ vs. α) away from the Galactic plane fits the WMAP haze well, in agreement with Kaplinghat et al. [102]. As in that work, we use an overall scaling factor to account for the uncertainties in particle production as well as a constant offset to account for uncertainties in background subtraction. We find that a physically reasonable scaling factor with electron production with similar magnitude to photon production in pulsars fits the data well.

We find that if one measures at an angle not orthogonal to the Galactic plane, but in an arbitrary direction, there is a strong dependence in the angular flux profile. As the direction of the line-of-sight shifts away from the vertical, there is a significant flattening in the angular flux profile (figure 3.1). This leveling-off is due to the large scale with which the pulsar distribution drops off in the s-coordinate as compared to the relative steepness with which it drops off in the z-coordinate. Also, the overall magnitude of Φ changes by a factor of four to five at angle $\alpha = 10°$. This effect is due to the fact that all fluxes should be equivalent in the Galactic center and begin dropping off with varying steepness at that angle. The 2-dimensional flux profile is

shown in figure 3.2.

For the zero central density pulsar distribution, the source term becomes

$$Q(E,\vec{x}) = \frac{d^2N}{dEdt}\rho_z(z)\rho_s^{0\mathrm{GC}}(s) \ . \tag{3.13}$$

With this profile, we need a slightly different normalization to match the flux of the haze, which could be accounted for by modifying diffusion-loss parameters. In this case, however, the flattening-out effect happens at angles much closer to the normal to the Galactic plane. Because this profile has its maximum density at around 4 kpc out from the Galactic center, the line-of-sight integral keeps increasing out to $\alpha \approx 25^\circ$. This creates a second peak in the angular flux profile at $\alpha \approx 20^\circ$ before the flux begins to fall off at large angles. This can best be seen in the (ℓ, b) diagram, figure 3.2, around $(\pm 20^\circ, 0^\circ)$. There the magnitude increases slightly; this feature is not apparent in the WMAP haze. Unless this feature is detected, it is improbable that such a Galactic pulsar distribution could cause the haze. This could be seen in upcoming Planck observations which will likely have a smaller mask [109].

3.4.2 Flux from Dark Matter Annihilations

Here we consider Dark Matter annihilations as a source for the haze. Using the source term $Q(E,\vec{x})^{\mathrm{DM}}$ and normalizing the flux Φ away from the Galactic plane to the haze, we solve the diffusion-loss equation to determine the angular flux profile for the $\gamma = 1.0$ and $\gamma = 1.2$ NFW-type profiles.

The results of the angular flux profile for these cases are shown in figure 3.3. As with the flux profiles due to pulsars, we used a constant offset to account for

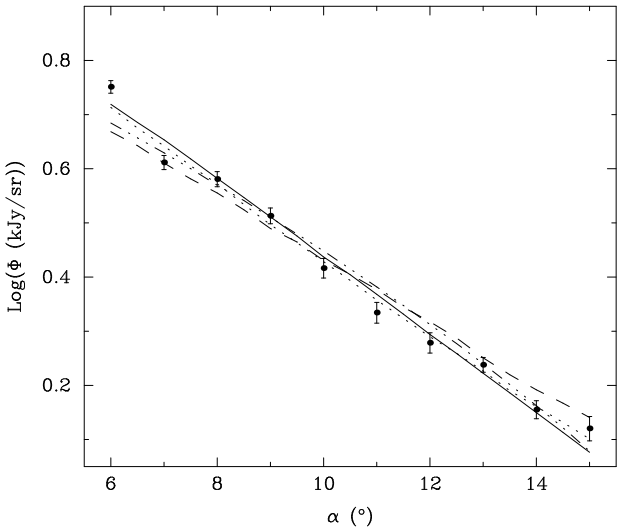

Figure 3.3: Angular flux profile, Φ versus angle from the Galactic center α for the $\gamma = 1.0$ and $\gamma = 1.2$ dark matter profiles. The upper lines are for the $\psi = 90°$ (solid) and $\psi = 0°$ (dotted) curves using $\gamma = 1.2$. The lower lines are for the $\psi = 90°$ (dash-triple dotted) and $\psi = 0°$ (dashed) curves using $\gamma = 1.0$. The plots are scaled with the $\psi = 90°$ plot normalized to the flux of the WMAP haze. The points are the WMAP haze with errors from Ref. [91].

uncertainties in background subtraction as well as a boost factor to account for the possible clumpiness of the dark matter. We found that it only required reasonable boost factors of five to ten to match the haze. Due to the significant lack of dependence on direction, we have only plotted the $\psi = 0°$ and $\psi = 90°$ (Φ, α) curves for each case. Significantly, the turning-over effect seen with pulsars is not seen here. Towards the Galactic plane, there is a slight flattening of the curve, but it is not as drastic as with the pulsar source. Given proper foreground subtraction, this distinction may be used to distinguish between the dark matter and pulsar explanations of the WMAP haze. In the diagrams of relative magnitude of Φ versus

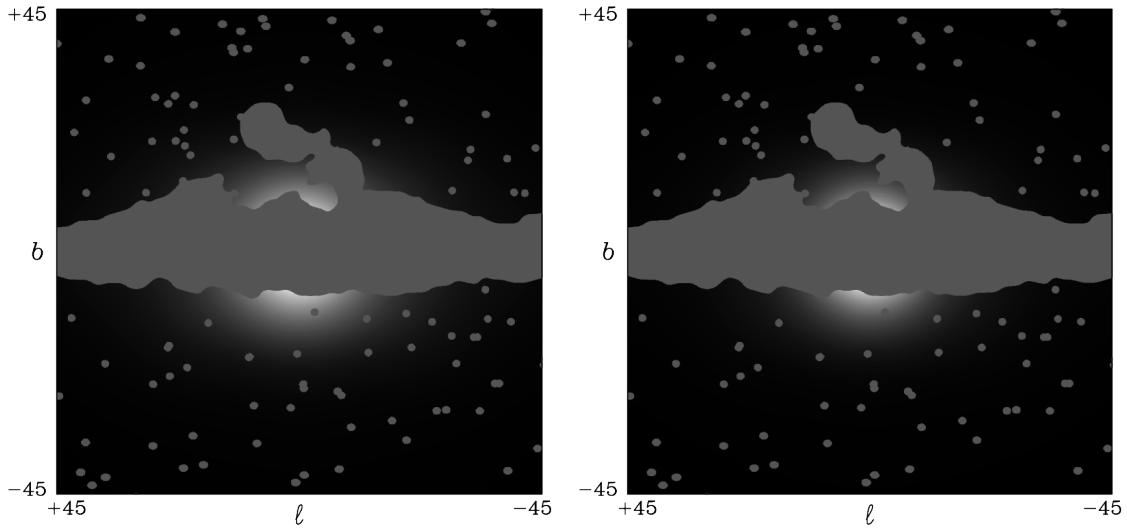

Figure 3.4: Relative flux Φ versus Galactic coordinates ℓ and b for the standard NFW dark matter profile with $\gamma = 1.0$ (left) and the NFW-type dark matter profile with $\gamma = 1.2$ (right). The mask is that from WMAP K-band mask Kp4 [125].

ℓ and b, figure 3.4, the two dark matter profiles have very similar characteristics. Both are significantly closer to spherical symmetry than the pulsar diagrams. There is some broadening in the b-direction, due to the size of the diffusion region being finite away from the Galactic plane. The cuspier $\gamma = 1.2$ profile loses magnitude much more quickly away from the Galactic center, so it appears slightly more spherically symmetric on a plot weighted by magnitude. However, both fall off in similar elliptical regions. This sensitivity of the WMAP haze to the dark matter density profile can be used to constrain the Galactic halo's profile if the dark matter model is verified. In particular, this should be seen in Planck observations using a likely smaller Galactic mask [109].

3.4.3 Dark Matter versus Pulsars

Not only can the details of the pulsar or dark matter distributions be tested separately, but these tests can distinguish between the two models and determine the source of the WMAP haze. For comparison, we will use the best-fitting candidate from each category: the Gaussian pulsar distribution and the $\gamma = 1.2$ dark matter distribution. Within the known values for each source, both can create a synchrotron signal large enough to cause the haze. Both sources have increased flux toward the Galactic center which falls off quickly away from it.

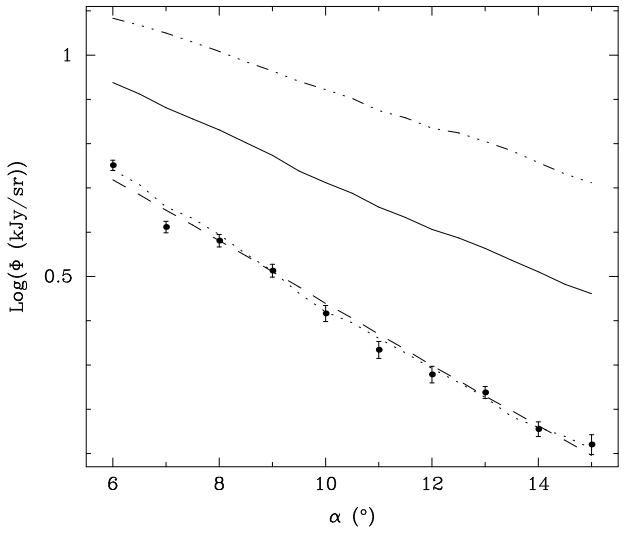

Figure 3.5: Angular flux profile, Φ versus angle from the Galactic center α for the $\gamma = 1.2$ dark matter profile and the Gaussian pulsar profile. The dashed line is the average over $\psi = 30^\circ - 90^\circ$ for the $\gamma = 1.2$ dark matter distribution. The upper (dash-triple dotted) line and lower (dotted) line are the $\psi = 30^\circ$ and $\psi = 90^\circ$ curves for the Gaussian pulsar distribution, respectively. The solid curve is an average from $\psi = 30^\circ - 90^\circ$ for the Gaussian pulsar distribution. The plots are scaled with the $\psi = 90^\circ$ plot normalized to the flux of the haze. The points are the WMAP haze with errors from Ref. [91].

The largest difference between these two possible sources is the strength of the signal towards the Galactic plane. For the pulsar source, the strongest signal comes along the Galactic plane and does not decrease very quickly near it. The dark matter source has approximately equal signal strength in all directions, though it does lose strength more slowly along the Galactic plane than in other directions. Unfortunately, the Galactic plane itself masks most of this primary difference, though there are regions near the Galactic center which remain unmasked. We therefore compare the signal away from the Galactic plane.

As can be seen in figure 3.5, there are two significant differences between the pulsar source and the dark matter source when looking above the Galactic plane. For $\psi \geq 30^\circ$, there is little distinguishable difference between the dark matter signal in any direction, so it is simply represented by the average over angles above 30 degrees. Primarily, the pulsar source has a different magnitude at different angles ψ. This can be seen by the vertical shift in the plots for different ψ values. Even among the angles above the mask, there is a factor of 3 decrease in the flux Φ for lines-of-sight away from the Galactic plane. Secondarily, there is a flattening in the pulsar signal that is not present in the dark matter signal. Over the angles $\alpha = 6^\circ$ to 15°, the $\psi = 90^\circ$ plot changes by roughly 50 percent more than the $\psi = 30^\circ$ plot. Such an effect is seen in the dark matter plots as well, but below the 10 percent level, which changes the signal minimally. Even above the mask, the two sources have substantial differences. With the Planck observatory's smaller expected Galactic mask, these differences should be even more apparent.

3.5 Conclusions

High-energy electrons/positrons moving in the Galactic magnetic field could be the source of the WMAP haze. Using the diffusion-loss equation, we have taken a set of models of likely sources and calculated the resulting synchrotron signal as a test for the models. The simplified equation can be solved analytically using a Green's function approach, where it is useful for an understanding of the underlying physics. We considered tests of several models of the haze source, namely a peaked Gaussian distribution of pulsars, a distribution of pulsars peaked away from the Galactic center, and two dark matter distributions as possible sources, all consistent with other constraints.

We find that the WMAP haze could be caused by diffuse synchrotron emission due to pulsars, in agreement with Kaplinghat et al. [102]. Moreover, we find that if the haze is caused by pulsars, the angular flux profile from the Galactic center should be peaked more sharply when using a line-of-sight away from the Galactic plane and is flattened significantly when using a line-of-sight closer to the Galactic plane. Also, if the pulsar distribution vanishes in the Galactic center, a brightness about 20° out along the Galactic plane should be visible.

With annihilating dark matter, the angular flux profile from Galactic center is largely independent of direction and has rough spherical symmetry. If the signal is found to be strongly spherically symmetric, then this would be an indication that annihilating dark matter could be the true source.

This directional-dependence of the angular flux profile would be a smoking gun

for pulsars causing the haze as opposed to the more spherical dark matter explanation. The Planck probe's increased sensitivity, larger number of bands, enhanced models, and expected smaller Galactic mask will test these models [109–111]. This will be instrumental in determining the source of the WMAP haze as an astrophysical signal or the indirect detection of the dark matter.

Chapter 4

The Contribution of Blazars to the Extragalactic Diffuse Gamma-ray Background and Their Future Spatial Resolution

4.1 Introduction

The source of the extragalactic isotropic diffuse gamma-ray background (DGRB) has been an unsolved question in astrophysics for some time. In this paper, we show how the DGRB spectrum can be produced by a combination of blazar and nonblazar active galactic nuclei (AGN) gamma-ray sources. We also show that the blazar flux source-count distribution function (dN/dF) is consistent with the full DGRB originating from these sources. Furthermore, we show how less-detailed models of the blazar contribution failed to be consistent with the DGRB. We explore how the implications for dark matter detection or constraints from the DGRB will evolve as the blazar sources of the DGRB are resolved.

The DGRB was first discovered by the SAS 2 experiment in 1975, for gamma-ray emission in the range of 35 to 300 MeV [126–129]. This background was seen at energies up to 20 GeV by the EGRET Collaboration, and it was confirmed at these energies in the first-year data from the Large Area Telescope (LAT) aboard the *Fermi Gamma-Ray Space Telescope* [130–132]. The assumed extragalactic source of the DGRB is determined by measuring the complete diffuse (unresolved) flux

and then subtracting off a model to account for the background coming from our Galaxy. This yields a measure of the flux coming from unresolved diffuse sources, presuming there is no minimal isotropic component from the Galaxy, e.g. dark matter annihilation or decay. The DGRB has been used to constrain dark matter annihilation in Galactic and extragalactic sources [36, 133, 134].

The most recent measurement of the DGRB was performed by the Fermi-LAT. In the Fermi-LAT Collaboration analysis, the gamma-ray intensity was measured in the range of 100 MeV to 100 GeV above 10° in Galactic latitude ($|b| > 10°$). The total flux is modeled by stacking the spectra of known sources with the cosmic-ray background, the Galactic diffuse background, and the DGRB. This analysis gives a DGRB intensity that is roughly 25% of the total observed flux. The DGRB seen by the Fermi-LAT is consistent with a power law in energy with index 2.41. This value for the DGRB is notably softer at high energies than was previously seen in the EGRET Collaboration, which is partly due to an updated model of the diffuse Galactic emission in Ref. [130] (hereafter FS10).

A detailed spectral energy distribution (SED) sequence model of blazars can reproduce the DGRB [135, 136]. We explore this model in this work. Many models have been proposed to explain the DGRB. It has been shown that emission from AGN can account for the diffuse background from 10 keV to 100 MeV, but above that energy, this model cannot account for the large gamma-ray flux [137]. Radiation from star-forming galaxies could account for much of the DGRB up to 10 GeV, but this also cannot explain the high intensities observed at higher energies [138]. Emission from millisecond pulsars has been proposed as a source as well [139].

However, millisecond pulsars as a dominant source of the DGRB may be inconsistent with the lack of anisotropy in the DGRB [140].

Dark matter annihilation, both as a component of the extragalactic diffuse emission and as an unaccounted foreground from the Milky Way can contribute to the DGRB, but the fluxes from dark matter are expected to be lower than the DGRB flux and have a different spectral shape [36, 133]. However, measurements of the DGRB are one of the strongest ways to constrain dark matter annihilation [134]. If dark matter is a significant contributor, it may be disentangled from astrophysical sources due to its angular correlation on the sky [141–147]. Pioneering work proposed that blazars could account for *all* of the DGRB seen by the EGRET Collaboration [148]. The blazar class of AGN has been studied in depth as the origin of the DGRB at high energies [148–159].

In Ref. [135] it was shown that the DGRB can be composed of blazars and nonblazar AGN in the luminosity-dependent density evolution (LDDE) SED blazar model. This model contains only three free parameters describing the gamma-ray luminosity function (GLF) of blazars. We show that this model is consistent with producing the full DGRB spectrum as well as the blazar source-count distribution, dN/dF, of blazars as measured by Fermi-LAT. In addition, we constrain this model by these measurements and find parameters for which the model successfully reproduces these measurements. Note that both the source-count distribution dN/dF and DGRB spectrum are predicted by the model, and not an input to the model.

Recent work by the Fermi-LAT Collaboration found that the DGRB could not be composed entirely by blazars [131] (hereafter FB10). However, that work adopted

an over-simplification of the blazar SED to be a single power-law (PL), independent of blazar luminosity, which is inconsistent with the observed spectral luminosity dependence seen in the SED sequence [160–162]. In contrast, in a separate paper, the Fermi-LAT Collaboration emphasizes the need for including departures from pure-PL behavior in blazar spectra when calculating the contribution of unresolved low-luminosity blazars to the DGRB [163]. Incorporating the SED departure and its dependence on blazar luminosity evolution when modeling the DGRB is exactly the intent of the work presented here.

Furthermore, the blazar model in FB10 lacks a physical evolution model for blazars. Instead of the source-count distribution resulting from the cosmological evolution of blazars, the source-count distribution is an input to the model, as a broken power-law with four free parameters. Note that even though the model in FB10 is simplistic, it contains *more* free parameters than the LDDE plus SED-sequence model explored here. In our approach there are three parameters in the adopted blazar model which describe the relation between the GLF and x-ray luminosity function (XLF). Because the FB10 model employs a pure-PL luminosity-independent SED with a broken-PL source-count distribution, the conclusions of that work do not apply to the model examined here. Other parameters in our work (*e.g.*, the SED sequence and the low-energy nonblazar AGN model) are constrained by other observations and remain fixed in our blazar model analysis. Namely, the observational constraints on the SED sequence come from spectral population models of blazars as in [161, 162, 164], and the nonblazar AGN spectrum is constrained by the hard x-ray luminosity function derived from *HEAO1*, *ASCA*, and *Chandra*

x-ray AGN surveys [137, 165].

A recent paper by Malyshev and Hogg [166] using the one-point probability distribution function (PDF) of the DGRB also concludes that blazars cannot constitute the total DGRB flux as measured by Fermi-LAT, when modeled as a pure-PL SED with a fixed dN/dF. However, this conclusion also only applies to the model which they consider, which adopt blazars as having pure-PL luminosity-independent SEDs, and not to the LDDE SED-sequence model examined here.

Because observed blazars make up about 15% of the total gamma-ray flux, unresolved blazars are a likely candidate to make up the DGRB [131, 132]. Blazars were the most numerous point-source objects observed by the EGRET Collaboration [167]. Additionally, observed blazar spectra tend to follow a similar power law in energy as the DGRB. However, it is known that blazars have a luminosity dependence to their spectral shape, which is incorporated in the SED-sequence model [161, 162, 164], but ignored in the analysis of FB10.

Blazars are the combination of two classes of AGN: flat-spectrum radio quasars (FSRQs) and BL Lacertae objects (BL Lacs). FSRQs are AGN that have spectral index $\alpha_r < 0.5$ in the radio band and have radio emission lines with equivalent width greater than 5 Å. BL Lacs have no strong absorption or emission features, and have equivalent widths less than 5 Å [168]. Broadly speaking, blazars tend to have their bolometric luminosities dominated by the gamma-ray luminosity and have great variability in that luminosity. Therefore, it is believed that blazars represent the small set of AGN that are observed along the jet axis, as opposed to nonblazar AGN which are observed far from the jet axis and dominate emission by their luminous

accretion disk. This jet source is expected to be relativistically beamed, as opposed to the more isotropic flux coming from the AGN's accretion disk [169, 170].

Different models of blazar emission have been proposed in the literature [148–159]. One is the pure luminosity evolution (PLE) model of the distribution of blazars [149–152]. In this model, only the blazar luminosity is evolved in redshift. An alternative model, LDDE, relates the gamma-ray luminosity of blazars to the redshift-dependent distribution of x-ray emission from nonblazar AGN [155]. This technique more realistically fits the blazar evolution to the AGN distribution, rather than assuming that all blazars have identical evolution regardless of luminosity. In many models for blazar spectra, a simple power-law or distribution of power laws is used as the intrinsic blazar spectrum, but more detailed frequency-dependent models have been used as well [153].

Here, we employ the LDDE model for blazar distributions. For the intrinsic spectrum of blazars, we use a frequency-dependent SED based on the multiwavelength study of Ref. [161, 162, 164]. We use these models to derive the differential blazar spectrum in redshift, luminosity, and energy. By integrating over these variables, we can determine the number of detectable blazars for given detector sensitivities, and we can calculate the expected gamma-ray flux from unobserved blazars to determine how significantly they contribute to the DGRB. Additionally, we add a fixed nonblazar AGN component to our predicted blazar flux, which should make the net flux from our model fit the diffuse background over the energy range from 10 keV to 100 GeV.

Below, we begin by describing the DGRB seen by the Fermi-LAT as well as its

data on blazars. We will then describe our model in detail, specifying the evolution model and SED used in our calculations and how we fit these to the known data. We use this model to predict the ability of the Fermi-LAT to detect blazars and how this will affect the DGRB. Throughout the paper, we take a flat universe with the cosmological parameters $\Omega_m = 0.272$, $\Omega_\Lambda = 0.728$, and $H_0 = 70.2$ km s^{-1} Mpc^{-1} [2]. *Note,* the use of h in the text refers to Planck's constant, and not the Hubble parameter.

4.2 First-Year Findings by the Fermi-LAT Collaboration

4.2.1 DGRB Measurements

From its first year of data, the Fermi-LAT has measured a spectrum for the DGRB (FS10). To get this spectrum, the total gamma-ray intensity had known sources subtracted from it, as well as the background from cosmic rays, and the expected Galactic diffuse emission. At this time, resolved extragalactic sources account for about 15% of the total gamma-ray flux in the sky. To calculate the gamma-ray emission from Galactic cosmic rays, the local cosmic-ray spectra are extrapolated to give source populations, which are then propagated through appropriate target distributions using the GALPROP particle propagation package [96, 97]. This diffuse Galactic emission is the largest component of the DGRB, comprising roughly half of the total observed intensity. A small component to the DGRB is a background due to cosmic-ray interaction with the Fermi-LAT itself. This background has been studied in detail in FS10 and is very well characterized. This background

accounts for 1 to 10% of the total emission, with a greater fraction at low energies and a lesser fraction at high energies. The residual intensity after all of these components have been removed is called the isotropic DGRB. It makes up around 25% of the total emission. Because of the model dependence of these subtractions, the uncertainties on the DGRB are dominated by systematics (FS10). The DGRB may come from unresolved extragalactic sources or unaccounted Galactic sources, such as millisecond pulsars, or, potentially, from Galactic dark matter annihilation or decay.

4.2.2 Point-Source Sensitivity

The Fermi-LAT detector has a spectrally dependent point-source sensitivity due to the higher spatial resolution of the instrument to higher-energy photons. The flux limit to point sources is shown in figure 4.1, along with the sample of blazar fluxes and spectral indices from FB10. In FS10, the DGRB spectrum is compared to that measured by EGRET, which had a point-source sensitivity of 1×10^{-7} ph cm^{-2}s^{-1}, despite the fact that the point-source sensitivity of the two instruments, and therefore the measured DGRB flux between the two instruments' measurements, are quantitatively different.[1] We derive the flux limit from the sample of blazars used in FB10, using the lowest-flux end of the blazar sample, which

[1]Because of this direct comparison in FS10, in the v1 preprint of this work, a point-source sensitivity cutoff of the measured DGRB spectrum of FS10 was adopted to be 1×10^{-7} ph cm^{-2}s^{-1}, instead of the spectrally dependent sensitivity here. This does not change our conclusions, but does modify our best-fit model parameters and our 5-year forecast DGRB spectra.

satisfied the test-statistic $TS = 25$. In FB10, the source-count distribution and DGRB spectrum was fit with only blazars resolved at $TS = 50$; therefore, the point-source limit is augmented by a factor of 2, as shown by the solid in figure 4.1, with the point-source sensitivity always below or equal to Fermi-LAT's believed completeness for all spectra sources at 7×10^{-8} ph cm^{-2}s^{-1}.

Importantly, it should be made clear that a fixed point-source sensitivity cannot be exactly specified for the DGRB spectrum derived in FS10. In that work, all sources above a $TS = 200$ are allowed to vary in the amplitude of their flux during the fitting of the extragalactic isotropic DGRB. Therefore, the exact flux-limit of the DGRB spectrum, and therefore the nature of the spectrum itself, as presented in FS10, is ill-defined. We therefore adopt the best-estimate method of modeling the DGRB spectrum as done by the Fermi-LAT Collaboration itself in FB10, with a $TS = 50$ spectrally-dependent flux limit. We define the power-law photon index Γ for the non-power-law SED-sequence model of a blazar by fitting a power law to the Poisson-limited spectrum within the observed energy range of Fermi-LAT.

As the point-source sensitivity of Fermi-LAT improves with integration time, the resolution of the extragalactic DGRB into point sources will not proceed proportionally to the sensitivity, but rather in a combination of the sensitivity with where the population of extragalactic emitters lies with respect to that sensitivity/spectral-index plane. In particular, for the LDDE plus SED-sequence blazar model here, there are more hard-spectrum sources with lower gamma-ray flux. This trend already can be seen in the plotted blazar points in figure 4.1.

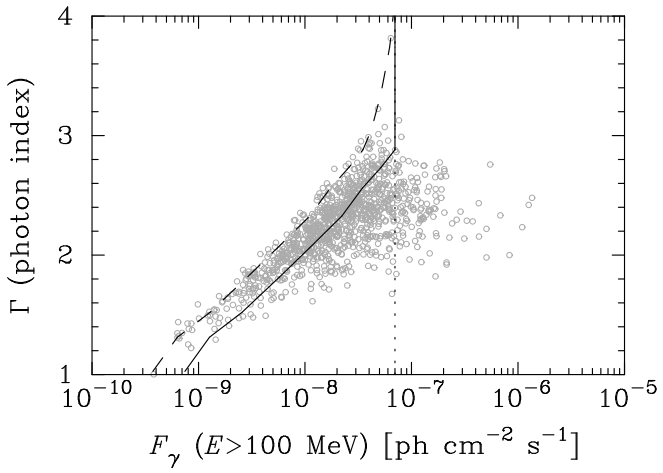

Figure 4.1: Shown is a sample of the blazar gamma-ray fluxes above 100 MeV (F_{100}) versus their power-law fit spectral-index Γ from FB10. The blazars (points) are shown above point-source detection test-statistic $TS = 25$ (with the corresponding point-source limit shown as the dashed line), while those below $TS = 50$ are modeled, in our work and in FB10, to contribute to the DGRB as measured by FS10 (with point-source limit shown by the solid line). Note the total luminosity vs spectrum dependence of the blazar population evident in this plot. The first-year Fermi-LAT point-source sensitivity is complete above the dashed line at 7×10^{-8} ph cm^{-2}s^{-1} (FB10).

4.2.3 Blazar Measurements

Through one year of running, the Fermi-LAT has detected a total of 296 FSRQs, 300 BL Lacs, and 72 blazars of unknown type. The observed FSRQs have an average spectrum with photon index 2.48 and BL Lacs have average photon index of 2.07 [171]. This power-law index is similar to the DGRB power-law index of 2.41, which suggests that unresolved blazars could be the primary source of the DGRB. Additionally, the stacked spectra of known blazars detected by the Fermi-LAT are

responsible for 15% of their total observed gamma-ray emission observed by the Fermi-LAT. The number of blazars observed above a given flux tends to follow a broken power law, with a break at $F(> 100\ \mathrm{MeV}) = 6 \times 10^{-8}$ photons cm^{-2} s^{-1}. This break seems to be independent of detector sensitivity, because the sensitivity dies off much more quickly as a function of flux than the blazar number count (FB10).

In the Fermi-LAT measurements, FSRQs and BL Lacs have similar variability properties, so the assumption that they are of one class appears valid. For BL Lacs, the LAT has detected significantly more hard-spectrum sources than soft-spectrum sources, which is consistent with the known selection bias in the measurement. FSRQs peak at a redshift of unity, indicating that the sample is approaching completeness. In contrast, BL Lacs peak at low redshift, indicating that the sample is not yet complete. FSRQs tend to be more luminous than BL Lacs: FSRQs have radio luminosities that peak at $L_{\mathrm{rad}} \approx 10^{44.5}$ erg/s whereas BL Lacs have lower radio luminosities peaking at $L_{\mathrm{rad}} \approx 10^{42}$ erg/s [171]. This would indicate that there is a fairly large contribution of low-luminosity, soft-spectrum BL Lacs that has yet to be resolved.

The differences in spectra between FSRQs and BL Lacs are significant. The average gamma-ray photon index is roughly 0.5 larger for FSRQs than for BL Lacs. Even among BL Lacs themselves, high-synchrotron-peak BL Lacs have a photon index of 2.28 while low-synchrotron-peak BL Lacs have a photon index of 1.96. FSRQs give off their peak synchrotron radiation at around 10^{13} Hz whereas for BL Lacs, the distribution is much broader, stretching from 10^{12} Hz to 10^{17} Hz [171]. FSRQs have their inverse Compton (IC) peaks at energies less than 100 MeV, so power-law fits

work fairly well to match their LAT-measured spectra. For BL Lacs, the peak IC emission tends to lie in the LAT's energy range, with low-synchrotron-peak BL Lacs peaking closer to 100 MeV and high-synchrotron-peak BL Lacs peaking closer to 100 GeV. Because of these peaks, these spectra do not match a power-law, though a broken power-law can approximately fit them [163].

To truly model the blazar SED, a multiwavelength analysis is needed [161, 162, 164]. The Fermi-LAT Collaboration did a multiwavelength study of the spectra of blazars, combining the results of several radio, x-ray, optical, and gamma-ray blazar studies [172]. This study found strong correlation between the x-ray and gamma-ray spectral slopes, indicating that blazar spectra fit a two-peaked, synchrotron plus IC scenario well. They found that BL Lacs have larger synchrotron peaks than FSRQs, which explains why BL Lacs have harder gamma-ray indices. This study plotted the SED for several blazars, all of which have a strong double-peaked shape when luminosity is plotted versus frequency on a log-log plot. This is consistent with previous analyses of the blazar SED [161, 162, 164].

4.3 Determination of Blazar Flux and Spectrum

4.3.1 Spectral Energy Distribution

The model of blazar emission we use consists of two parts: a GLF to give the density of blazars per unit luminosity and an SED to determine the luminosity of blazars as a function of energy. These are denoted by $\rho_\gamma(L_\gamma, z)$ and $\nu L_\nu(x; P)$, where z is redshift of the blazar, L_γ is the gamma-ray luminosity (defined as νL_ν

at $h\nu = 100$ MeV), $x \equiv \log_{10}(\nu/\text{Hz})$ for blazar rest-frame frequency ν, and P is the bolometric luminosity. Because our SED separates blazars according to radio luminosity, the bolometric luminosity is used to determine which SED curve matches a given blazar. For a given SED curve, the bolometric luminosity can be calculated as $\int L_\nu d\nu$. This can then be used to find the gamma-ray luminosity.

Ref. [161, 162, 164] analyzed the relationship between frequency and luminosity for blazars. To get these relationships, blazars were binned by radio luminosity. This analysis showed that blazar gamma-ray index is correlated with blazar luminosity. This correlation is consistent with the experimental results that FSRQs have high luminosities and large gamma-ray spectral indices while BL Lacs have lower luminosities and smaller spectral indices [163, 172, 173]. A proper calculation using blazar spectra should account for this relationship between index and luminosity, and not simply use a power law in energy for the blazar spectrum. Note that this was not done in Ref. [131], which claimed that blazars cannot constitute the full DGRB.

For the frequency dependence of the blazar luminosity, we use the SED sequence of Inoue and Totani [135]. In this model, blazars SEDs are fit over frequencies from radio to gamma ray, as in Ref. [161, 162, 164]. Each SED is comprised of two components, a synchrotron component at lower energies and an IC component at higher energies. These are each parameterized by a parabolic peak with a lower-energy linear tail. The details of the model are determined by fitting to the data in Ref. [161, 162, 164], which give νL_ν as a function of rest-frame frequency ν for five luminosity bins. This provides the gamma-ray luminosity (νL_ν at $h\nu = 100$ MeV),

the specific luminosity $L_\nu(\nu)$, and the bolometric luminosity $\int L_\nu d\nu$ for a blazar with known radio band luminosity (νL_ν at 5 GHz). The full model can be found in Appendix B.1.

As a check on the versatility of the SED model, we explicitly compared the model to several blazar spectra measured by the Fermi-LAT Collaboration [163, 172]. The model fit the data in the Fermi-LAT energy range well. It also matched the data qualitatively: the model spectra had increasing, decreasing, or flat spectral shapes in agreement with the Fermi-LAT-measured spectra. Such agreement indicates that this SED fit approximates the full blazar SED well.

4.3.2 Gamma-ray Luminosity Function

For the distribution of gamma-ray blazars, we follow the hard x-ray AGN distributions parameterized by Ueda et al [165]. Similar work was done for soft x-rays by Hasinger et al [174]. However, the hard x-ray parameterization gives a more conservative prediction of blazar detection by Fermi-LAT, so we use that here. For rest-frame (emission frame) energy of $\epsilon_{\rm gam,res} = 100$ MeV, the gamma-ray luminosity is given by $L_\gamma \equiv (\epsilon_{\rm gam,res}/h) L_\nu(\epsilon_{\rm gam,res}/h, P)$.

Reference [135] argues that the gamma-ray luminosity can be related to the x-ray AGN disk luminosity L_X through the bolometric luminosity by $P = 10^q L_X$, where q is a scaling parameter. This is because the bolometric luminosity from a blazar jet is proportional to the mass accretion rate $\dot{m}$. For blazars with low accretion rate, the conversion of power into luminosity is inefficient, with $L_X \propto \dot{m}^2$.

For blazars with high accretion rate close to the Eddington limit, the conversion is efficient and the disk luminosity goes as $L_X \propto \dot{m}$ [175–177]. Because black hole growth takes place mostly near the Eddington limit, it is reasonable to assume that $P \propto \dot{m} \propto L_X$ [178]. Note, L_X is the x-ray luminosity from the accretion disk of the blazar, not to be confused with the x-ray luminosity of the beam.

The comoving number density per unit L_γ of gamma-ray blazars is

$$\rho_\gamma(L_\gamma, z) = \kappa \frac{dL_X}{dL_\gamma} \rho_X(L_X, z), \tag{4.1}$$

where ρ_X is the comoving number density of AGN per unit L_X, z is the redshift to the source, and κ is the fraction of AGN observed as blazars. The quantity ρ_γ is referred to as the GLF. A parameterization of the x-ray luminosity function ρ_X is found in Appendix B.2. The GLF has three free parameters: q determines the ratio of bolometric jet luminosity to accretion-disk x-ray luminosity, γ_1 is the faint-end index that determines how the GLF behaves for low luminosities, and the blazar fraction is κ.

These GLF models are based on LDDE of AGN, as opposed to PLE models. In PLE models, AGN luminosity changes with redshift, but the comoving density of AGN remains constant. This has been a popular method of determining blazar parameters [149–152]. LDDE models have a peak evolution redshift which depends on luminosity, so AGN of different luminosities will have slightly different evolutions [165, 174]. This gives a better fit to the AGN data and should describe blazar evolution more fully than PLE models [155]. The exact relationship between x-ray AGN and gamma-rays blazars is not yet known. We are using the simple ansatz that

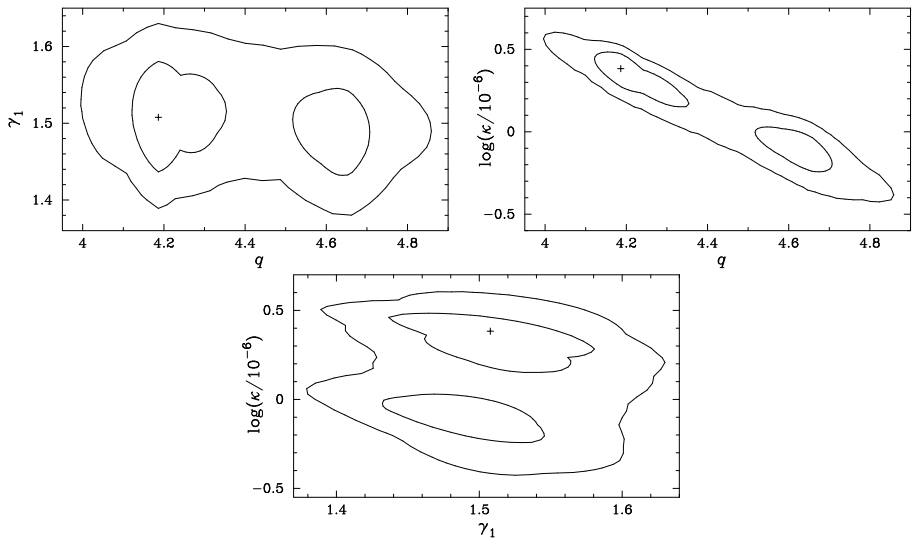

Figure 4.2: Shown are contours with 68% and 95% confidence level (CL) regions for the parameters of the luminosity scale q and GLF faint-end index γ_1, q vs κ, and κ vs γ_1. The best-fit value is labeled by the cross.

they are related as shown in Eq. (4.1), as proposed by Inoue and Totani [135]. To the best of our knowledge, this model satisfies all current observations and constraints, and therefore is a viable possibility.

4.3.3 Calculation of Blazar Number and Flux

For a given blazar, the gamma-ray flux observed on Earth is

$$F_\gamma(z, P) = \frac{1+z}{4\pi d_L(z)^2} \int_{E_{\rm min,obs}(1+z)/h}^{\infty} d\nu \frac{L_\nu(\nu, P)}{h\nu}, \tag{4.2}$$

where d_L is the luminosity distance, P is the bolometric luminosity, and $E_{\rm min,obs} = 100$ MeV is the minimum observable photon energy on Earth by the Fermi-LAT.

With the GLF and SED, the number count of blazars detected above a sensi-

tivity F_γ is

$$N(>F_\gamma) = 4\pi \int_0^{z_{\rm max}} dz \frac{dV}{dz} \int_{L_\gamma^{\rm lim}(z,F_\gamma)}^{\infty} dL_\gamma \rho_\gamma(L_\gamma, z), \tag{4.3}$$

where $L_\gamma^{\rm lim}$ is the luminosity below which a blazar at redshift z is no longer detectable for the sensitivity F_γ. We set the parameter $z_{\rm max} = 5$, but this does not affect the calculation significantly, since the peak distribution is at redshift of order unity.

The diffuse flux coming from unresolved blazars is given by

$$\begin{aligned} \frac{dN}{dE_{\gamma 0} dA dt d\Omega} = \quad & \frac{1}{4\pi} \int_0^{z_{\rm max}} dz \frac{d\chi}{dz} e^{-\tau(z, E_{\gamma 0})} \\ & \times \int_{L_{\gamma,\rm min}}^{L_\gamma^{\rm lim}(F_\gamma, z)} dL_\gamma \frac{\rho_\gamma(L_\gamma, z)}{h} \\ & \times \frac{L_\nu[E_\gamma/h, P(L_\gamma)]}{E_\gamma}. \end{aligned} \tag{4.4}$$

Here, E_γ is the emitted photon energy [and $E_{\gamma 0} = E_\gamma/(1+z)$ is the observed photon energy at Earth], A is area on Earth, t is time on Earth, and Ω is solid angle in the sky. Here $L_\nu/(E_\gamma)$ is the number of photons emitted per rest-frame frequency per rest-frame time per blazar (h is Planck's constant). The quantity $dL_\gamma \rho_\gamma$ is the number of blazars per comoving volume. The integral $d\chi$ is the line-of-sight integral over the comoving distance. Because for $\gamma_1 > 1$ the integral diverges at zero luminosity, $L_{\gamma,\rm min}$ is a lower bound on the luminosity integral. We choose $L_{\gamma,\rm min} = 10^{42}$ erg s^{-1} which is an order of magnitude lower than any Fermi-LAT observed blazar [163, 172]. That is, we impose a step-function cutoff of blazar GLF. The final result is not strongly dependent on the value of this cutoff, with a 2-order-of-magnitude difference in $L_{\gamma,\rm min}$ modifying our best-fit parameters by $\sim$25%.

The $\exp(-\tau)$ factor in the diffuse flux calculation accounts for absorption of the photons on intergalactic background radiation before reaching Earth. We use the

absorption factor from Gilmore et al. [179]. This absorption factor was determined through the use of galaxy formation models to find the contribution of starlight to the absorption, as well as a contribution from quasars which is calculated based on empirical data. This model predicts lower values of the opacity τ than previous estimates, which leads to less expected absorption. This is consistent with the Fermi-LAT observing several high-energy photons coming from fairly high redshifts, and this opacity is consistent with the findings of Ref. [180].

4.3.4 DGRB Spectrum Calculation

In addition to the blazar contribution to the DGRB flux, we also include a nonblazar AGN component to our DGRB spectrum calculation. Ref. [137] has shown that nonblazar AGN can account for the background radiation down to keV energies. The combination of blazars with nonblazar AGN gives a unified model that can explain the diffuse high-energy x-ray to gamma-ray background over 8 orders of magnitude in energy.

The AGN model we use is the model of Ref. [137]. This model assumes the usual thermal electrons from AGN coronae, but it includes a high-energy nonthermal component as well. These electrons Comptonize, which produces the known x-ray spectra of AGN. This high-energy component is analogous to the emission from solar coronae in solar flares. Such electrons are assumed to have a power-law injection spectrum $dN/dE \propto E^{-\Gamma}$. By adding this nonthermal electron source to the usual thermal one, it is found that the model matches the diffuse background spectrum

well from energies from keV to tens of MeV.

Specifically, we choose the $\Gamma = 3.5$ nonblazar AGN model of Ref. [137], which we increase in amplitude by a factor of 2 in order to match 50% of the amplitude of the lowest-energy point in the Fermi-LAT DGRB spectrum, with a broken power law matching the measurements of the diffuse background by the COMPTEL Collaboration [181]. The power-law slope of the nonblazar AGN spectrum is fixed by modeling of the hard x-ray luminosity function from x-ray AGN surveys [137, 165], and the amplitude is fixed to match the lowest point in the Fermi-LAT DGRB spectrum. This amplitude is fixed throughout our fitting. In order to reflect the uncertainty of the amplitude of the flux in the lowest-energy bin, we allow for it to have an amplitude uncertainty of 10%, which we vary and show in figure 4.3. Another low-energy emission source, such as millisecond pulsars or star-forming galaxies, may be responsible for the lowest-energy portion of the DGRB, but our analysis is not strongly dependent on the spectral shape taken by the low-energy emission source. For example, the gamma-ray spectrum from star-forming galaxies in Ref. [138] has a similar shape and potential amplitude as the nonblazar AGN component.

In our blazar model, there are three free parameters, in addition to those fixed in the nonblazar AGN model, as described in section 4.3.2: q, γ_1, and κ. All other parameters in the blazar model are fixed to values based on data from other observations such as the SED sequence. It is the purpose of this paper to determine how well unresolved blazars can reproduce the DGRB. Therefore, we simultaneously fit to the blazar source-count distribution dN/dF from Ref. [131] and the DGRB spectrum from FS10. This simultaneous fit allows some freedom in

the blazar spectrum while still conforming to known blazar number distributions. We can use the results of such a fit to constrain models of the DGRB from unresolved blazars and predict a consistent model of the 5-year Fermi-LAT measurements of the DGRB.

Fitting the model to the blazar dN/dF and the DGRB spectrum, we found that a simultaneous fit was quite reasonable. We set the lowest blazar luminosity as $L_{\gamma,\mathrm{min}} = 10^{42}$ erg s^{-1}, as discussed above. The best-fit values we get are $q = 4.19^{+0.57}_{-0.13}$, $\gamma_1 = 1.51^{+0.10}_{-0.09}$, and $\log_{10}(\kappa/10^{-6}) = 0.38^{+0.15}_{-0.70}$ (95% CL). The best-fit 68% and 95% CL regions for q and γ_1 are shown in figure 4.2. These are consistent with previous work [135], though more constrained because we are also fitting the source-count distribution function dN/dF. The model reproduces the DGRB and blazar dN/dF, with a reduced $\chi^2/\mathrm{DOF} = 0.63$. The value of q indicates that the bolometric luminosity of a blazar jet is roughly 15 thousand times more luminous than the x-ray from the accretion disk. Here, $\gamma_1 > 1.0$ so low-luminosity blazars have significant contributions to the total blazar flux. Therefore, a ten or more order-of-magnitude lower value of $L_{\gamma,\mathrm{min}}$ would modify the calculation considerably, though no blazars have been detected below our $L_{\gamma,\mathrm{min}}$ threshold, and therefore it seems unlikely that there is a large population of very-low-luminosity blazars. The fraction $\kappa \simeq 2.4 \times 10^{-6}$ implies that there is roughly one blazar for every 420 thousand nonblazar AGN. Our fit to the DGRB spectrum is shown in figure 4.3 and the fit to dN/dF is in figure 4.4.

Our value for the AGN XLF and blazar GLF ratio κ, 3.4×10^{-6} to 5×10^{-7} (at 95% CL), is similar to and slightly larger than the central value derived by Inoue &

Totani [135], 1.7×10^{-6}. This implies that only a small fraction of x-ray loud AGN is visible as gamma-ray blazars. The intrinsic jet opening angle of a blazar has been found to be ~ 1 deg (subtending an area of $\sim 2 \times 10^{-4}$ steradian) [183]. Following from this is that only $\sim 2 \times 10^{-5}$ of the AGN jets are potentially visible as blazars. Our model then requires that only $\lesssim 20\%$ of AGN jets are gamma-ray blazars. This is not inconsistent with jet models [184], though if this fraction drops considerably (i.e., κ is required to be much smaller), then it would call into question the blazar model analyzed here.

Note that using the dN/dF estimated from a power-law blazar spectrum model is not perfect, due to the fact that the detection efficiency estimate depends on the spectral model [131]. However, Ref. [131] tested the dN/dF dependence on the sensitivity estimate with a non-power-law fit to the blazar spectra and found it did not significantly change the measurement of dN/dF. We also verified this sensitivity dependence with a test fitting by increasing the errors on the measured dN/dF at low flux, and we found that our model did not prefer a different amplitude or shape to the source counts at the low flux where the efficiency for blazar detection is low.

Refs. [135, 136] used a combined GLF plus SED model to predict the Fermi-LAT's ability to observe blazars and their spectra, using the results of the EGRET Collaboration. The paper fit its GLF parameters using the redshift and gamma-ray luminosity distributions of EGRET blazars. This led to a prediction that 600 to 1200 blazars should be resolved in 5 years of Fermi-LAT data, which would yield 98% to 100% of the total blazar flux. However, the cumulative number of blazars predicted by that paper is in disagreement with the observations of the Fermi-

LAT [131]. The cumulative number count by Ref. [135] is predicted to have a break at 10^{-7} photons cm^{-2} s^{-1} whereas the break seen by the Fermi-LAT Collaboration is at 5×10^{-8} photons cm^{-2} s^{-1}. Also, the surface density of sources predicted in that paper is too small to match the measured value.

Importantly, Refs. [135, 136] fit their model to the EGRET catalog blazar spectra SED, not that from Fermi-LAT. The EGRET telescope had strong cuts which limited high-energy photon observations, which lead to EGRET only observing a few BL Lacs [131]. Also, the redshift and luminosity distributions are strongly dependent on detector sensitivity, because BL Lacs have lower luminosity and therefore are observed at lower redshifts. This means that the current data for the overall blazar redshift distribution, in particular, is more strongly biased toward lower redshifts than the complete distribution. Ref. [185] posited that one significant source for the difference between this calculation and the Fermi-LAT results comes from needing to correctly account for Fermi-LAT sensitivities. By fitting to dN/dF, which is not as heavily dependent on detector sensitivity, we can get a more robust prediction that should not change significantly for different sensitivities. Refs. [135, 136] argued that a model of this type should roughly match the DGRB spectrum. In Ref. [135], the model parameters were fit to the EGRET DGRB spectrum, and, as discussed above, the model parameters are roughly consistent with our results. In our analysis here, we use the DGRB spectrum and flux source counts, as measured by the Fermi-LAT, as a constraint in order to determine how well this class of models fits the DGRB and blazar population. For those models that fit the spectrum, we can determine the predicted values for the DGRB flux at the Fermi-LAT's 5-year

sensitivities and determine the theoretical uncertainty on these predictions.

In another analysis of the contribution of blazars to the DGRB, the Fermi-LAT Collaboration used the currently measured differential number distributions of blazars (dN/dF) and blazar gamma-ray index (Γ) distributions to estimate the contribution of unresolved blazars to the DGRB [131]. In that analysis, it was found that less than 20% of the DGRB can be accounted for by blazar emission. However, in that calculation, the assumption was made that the distribution of indices Γ is independent of sensitivity. Because less-luminous BL Lacs have significantly different indices than more luminous FSRQs, the overall distribution of indices should change as better sensitivity allows a greater fraction of BL Lacs to be detected.

Additionally, it was shown in Refs. [163, 172] that a basic power-law model does not fit the individual blazar spectra well, especially for the low-luminosity BL Lacs. A GLF plus SED model should overcome these issues. The GLF accounts for differing redshifts of blazars, so the relationship between flux sensitivity and luminosity detectability is well-defined. The SED accounts for the distribution of luminosities with energy, so a calculation around the IC peaks for BL Lacs should more realistically reproduce the contribution to the DGRB from blazars than a simple distribution of photon indices. This is especially important to incorporate when determining the contribution of unresolved low-luminosity blazars to the DGRB, since they have much harder spectra than high-luminosity blazars.

4.4 5-year Predictions for Blazars and the DGRB

We adopt the 5-year predictions for a sensitivity to point-sources by Fermi-LAT of $S_5 = 2 \times 10^{-9}$ photons cm^{-2} s^{-1} above 100 MeV. This value is consistent with the Fermi-LAT Collaboration's estimate of the LAT sensitivity to point sources with gamma-ray index of $\sim$2 [186].[2] As discussed earlier, the majority of low-flux blazars are expected to be BL-Lacs, which predominantly have radio luminosity less than 10^{43} erg/s [171]. Such low-luminosity blazars have gamma-ray indices of $\sim$2 or less, according to the blazar SED. Therefore, we find the use of $S_5 = 2 \times 10^{-9}$ photons cm^{-2} s^{-1} as the Fermi-LAT 5-year sensitivity to blazars of all gamma-ray indices to be a reasonable estimate.

To determine the total number of blazars detectable by the Fermi-LAT, we need to take Eq. (4.3) down to a sensitivity of S_5. Similarly, we can determine the total number of blazars in the sky by letting the sensitivity go to zero flux. With 95% CL, we predict that there are $5.4^{+1.8}_{-1.7} \times 10^4$ total blazars in the observable universe. Of these, 2415^{+240}_{-420} should be detectable by the Fermi-LAT after 5 years of running. The amount of flux coming from blazars per logarithmic sensitivity is shown in figure 4.5. Our prediction is that $94.7^{+1.9}_{-2.1}$% of blazar flux is expected to be resolved by the Fermi-LAT after 5 years, mostly at lower energies. In contrast, the flux for nonblazar AGN should not be appreciably resolved for another 4 orders of magnitude in sensitivity.

In addition to the number counts of blazars, we can also predict the distribu-

[2] http://fermi.gsfc.nasa.gov/science/433-SRD-0001_CH-04.pdf

tions of blazars in luminosity and redshift. To get these distributions, we differentiate Eq. (4.3). The distribution of blazars in radio luminosity, shown in figure 4.6, shifts toward lower luminosities at better sensitivities. This is due to the FSRQ population being mostly resolved, whereas the new resolved sources at better sensitivities are mostly low-luminosity BL Lacs. The redshift distribution of blazars, figure 4.7, should shift toward higher redshifts as sensitivity improves. Because the FSRQ sample is mostly complete, it would be expected that the redshift distribution of BL Lacs, and blazars in general, should be roughly similar to the current redshift distribution of FSRQs. Our prediction of the redshift distribution of blazars after 5 years of Fermi-LAT running matches well with the current FSRQ distribution, which provides a verification of our theory and fit parameters. Note that the FSRQ sample is not totally complete, and the objects to be resolved at $z \gtrsim 2$ would be FSRQs. As can be seen in figure 9 of Ref. [171], the distribution of FSRQs reaches the current flux limit, so there remains a population of high-luminosity, soft spectral index, high redshift FSRQs to be resolved.

In our model, we fit the total blazar plus AGN flux to the DGRB spectrum for the spectrally-dependent sensitivity as described above. The model fit worked exceptionally well, indicating that a combination of blazar flux with the flux of nonblazar AGN makes up all the DGRB over a wide range in energies. With this fit, we then calculated what the combined flux should be after 5 years of Fermi-LAT observations, giving the sensitivity of 2×10^{-9} photons cm^{-2} s^{-1}. The upper and lower bounds of the 95% CL region of this calculation are given by the upper and lower forecast points in figure 4.3. We have included a 10% uncertainty on the

nonblazar AGN flux in this error estimate to account for the error in the lowest-energy bins' constraint on the AGN model. At 100 GeV, we expect the DGRB to decrease by a factor of 1.6 to 2.6 at the 95% CL upper and lower flux limits, whereas at 100 MeV the DGRB only decreases by a factor of 1.3 to 1.9. The difference in DGRB improvement is due to a greater fraction of the DGRB being due to blazars at high energies, while the nonblazar AGN flux dominates at low energies. Importantly, the resolution of sources can do better than the square root of exposure time due to the increased prevalence of easily-detected hard sources beyond, but near, the current point-source flux-limit sensitivity.

4.5 Conclusions

We have shown that the DGRB can be composed entirely by gamma-rays produced in blazars and nonblazar AGN. The LDDE plus SED-sequence is a physical model for the spectral evolution of a cosmologically-evolving blazar population contributing to the DGRB based on the unified AGN model for blazars. This model successfully accounts for the full DGRB spectrum as well as the full blazar source-count distribution function, which, unlike other approaches, are not used as components of the model. Independent of the nonblazar AGN component, the blazar model produces nearly the entire DGRB at its highest measured energies. The small value of $\kappa \simeq 2.4 \times 10^{-6}$, the x-ray AGN fraction seen as blazars, constrains this model to require a small fraction, $\lesssim$20%, to be both properly oriented and sufficiently energetic in order to be gamma-ray emitters.

We found constraints on this model from the spectrum of the DGRB and source-count distribution function dN/dF of blazars as observed by Fermi-LAT. Our results are consistent with previous work by Inoue & Totani [135] which employed EGRET spectral data to forecast the Fermi-LAT DGRB. We forecast that $94.7^{+1.9}_{-2.1}\%$ of the flux from blazars will be resolved into point sources by Fermi-LAT with 5 years of observation, with a corresponding reduction of the flux in the DGRB by a factor of $\sim$2 to 3 (95% CL) from the automatic removal of these sources in the measurement of the DGRB. This has significant consequences for the sensitivity of the DGRB measurement to dark matter annihilation, which we explore in a companion paper [31].

We predict that 2415^{+240}_{-420} blazars should be resolved, of $5.4^{+1.8}_{-1.7} \times 10^4$ total blazars in the universe (95% CL). Recent results of anisotropy in the DGRB also indicate the likely presence of an unresolved point-source population [187]. Using tests with enhanced point-source sensitivity, we find that future gamma-ray experiments at Fermi-LAT energies will resolve the blazar contribution to the DGRB such that the flux in the DGRB decreases as the square root of the point-source sensitivity.

The LDDE plus SED-sequence model is more complex than the over-simplistic source-count method with a fixed spectral-index distribution adopted by the Fermi-LAT Collaboration in FB10, yet it has *fewer* free parameters for the blazar population than the more simplified model (three versus four free for the blazar model, plus those fixed in the nonblazar AGN model in this work). Most importantly, the Fermi-LAT analysis of FB10 fixes the spectral index of the blazar population, and, crucially, does not include the hardening of the spectra of the unresolved low-

luminosity blazar population. The hardening of spectra with lower luminosity has been seen by both EGRET [161, 162, 164] and Fermi-LAT (figure 4.1). The fixed spectrum forces the FB10 conclusion that only $\sim$16% of the GeV isotropic diffuse background could arise from blazars, and is also the case in other work using fixed blazar spectra [166]. Other recent work with different blazar population models, including spectral shape variation [188], possible point-source confusion [189], and BL Lac dominance of the unresolved portion [190] also find that a substantial portion of the DGRB could arise from the blazar population.

Overall, the SED-sequence model of blazars and AGN as the source of the DGRB is remarkably consistent with the measured DGRB spectrum and blazar source-count distribution. The SED-sequence will continue to be improved with upcoming Fermi-LAT blazar data [191]. Further analyses of the type presented here, incorporating potential enhancements to the SED-sequence model, the XLF of AGN, and general studies of observed blazar spectral properties, will further enlighten the understanding of the extragalactic gamma-ray sky.

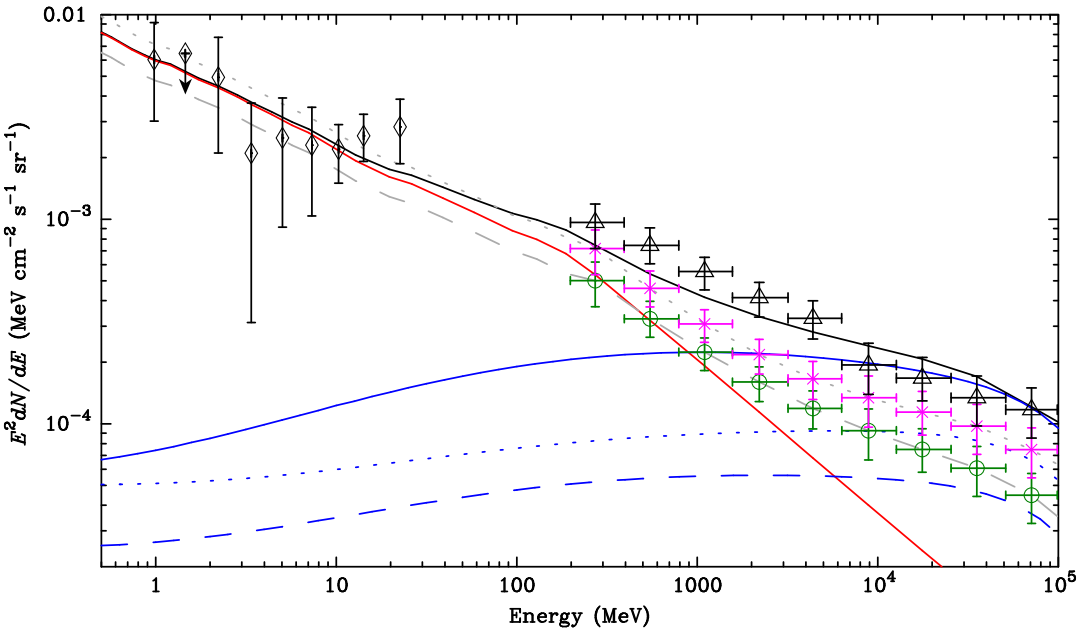

Figure 4.3: Shown are the best-fit model for the current DGRB spectrum (solid black line) and our upper/lower 95% CL forecast for the Fermi-LAT 5-year sensitivity (magenta-star/green-circle points). The low-energy-dominating solid red line is the AGN flux from Ref. [137]. The high-energy-dominating blue lines are the blazar contribution to the DGRB for the current (solid), and predictions for the most-optimistic (dashed) and least-optimistic (dotted) 95% CL 5-year Fermi-LAT resolved fractions. The grey lines are the combined 95% CL AGN plus blazar predicted flux for the corresponding blazar contribution. The DGRB data (triangles) are from FS10 and the COMPTEL data (diamonds) are from Ref. [182].

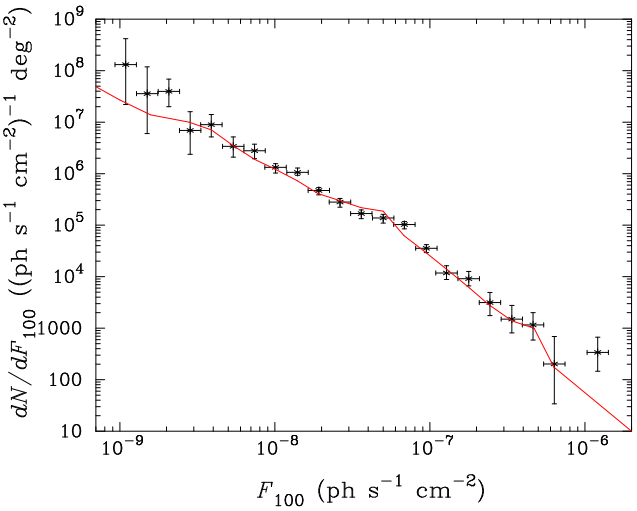

Figure 4.4: Shown is the best-fit model for the source-count distribution function dN/dF (solid line). The data are from Ref. [131]

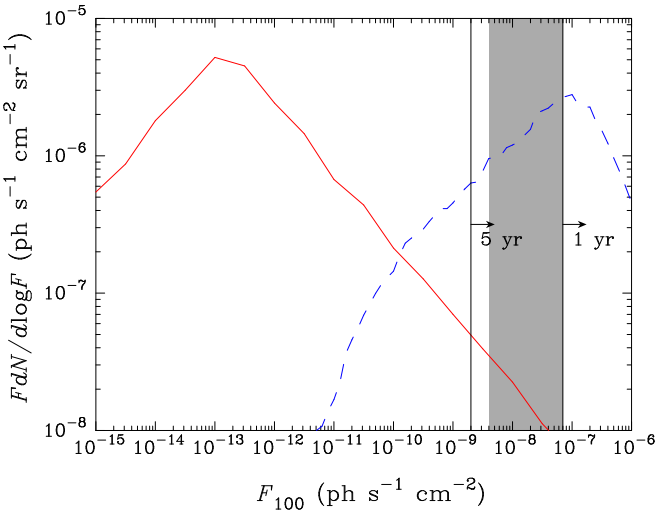

Figure 4.5: Shown is the flux per logarithmic sensitivity for our best-fit model. The dashed line is the flux coming from blazars and the solid line is the flux coming from nonblazar AGN. The vertical solid lines with arrows mark the sensitivity to *all* spectral-index sources at the Fermi-LAT 1-year and the projected 5-year sensitivity of Fermi-LAT. The gray boxed region indicates the range of sensitivity at 1-year to sources with the spectral indices of the bulk of the blazar population, as in figure 4.1.

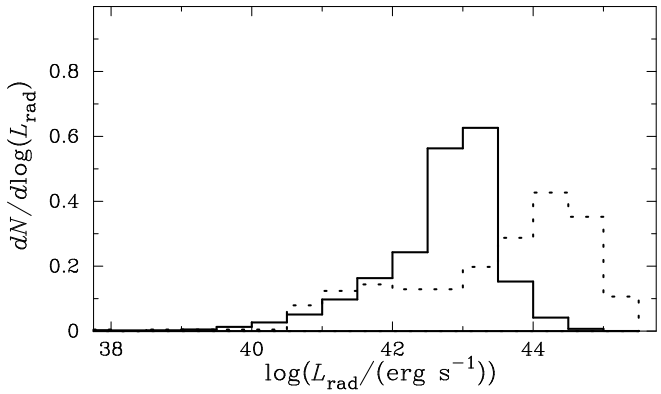

Figure 4.6: Shown is the radio luminosity distribution of blazars. The solid line is our prediction for the distribution after 5 years of Fermi-LAT running. The dotted line is the current Fermi-LAT distribution for blazars [171]. Each distribution is independently normalized to unity.

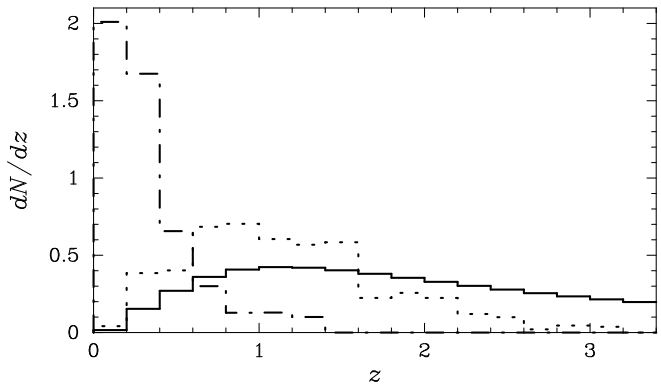

Figure 4.7: Shown are the distribution in redshift of blazars. The solid line is our prediction for the distribution after 5 years of LAT running. The dotted line is the current Fermi-LAT-measured distribution for FSRQs and the dot-dashed line is the current Fermi-LAT-measured distribution for BL Lacs [171]. Each distribution is independently normalized to unity.

Chapter 5

Current and Future Constraints on Dark Matter from Prompt and Inverse-Compton Photon Emission in the Isotropic Diffuse Gamma-ray Background

5.1 Introduction

The existence of cosmological dark matter is well established by observations of galaxy clusters, galaxy rotation curves, the cosmic microwave background (CMB) and large-scale structure, though its nature remains a fundamental problem in cosmology and particle physics. There exists an abundance of particle candidates which could account for the dark matter (for a review, see, e.g. [32]). For a class of particles with weak-scale interaction and weak-scale particle mass, weakly interacting massive particles (WIMPs), their production in the early Universe in thermal processes naturally produces the observed dark matter density, largely independent of the particle mass.

Thermal freeze-out predicts a canonical annihilation rate of $\langle \sigma_{\rm A} v \rangle \approx 3 \times 10^{-26}$ cm^3 s^{-1}. This predicted annihilation rate in standard model channels leads to energetic gamma-ray production in the hadronization of quarks, the Higgs or gauge bosons, through bremsstrahlung in the case of the lighter leptons, or directly to two gammas through higher order processes. The diffuse gamma-ray background

(DGRB) was forecast to be one of the most robust constraints on annihilating WIMP dark matter [134]. Because of a more conservative model for the extragalactic dark matter signal, the conservative limits on dark matter annihilation presented by the Fermi-LAT Collaboration from the 1-year observation of the DGRB [130, 133] were weaker than prelaunch estimates [134]. On the other hand, it was shown that the DGRB has an irreducible contribution from the Milky Way Galactic dark matter halo [40] that is greater in amplitude than the conservative estimates of the extragalactic contribution, and correspondingly has more stringent limits over many annihilation channels [36]. This irreducible, isotropic component is due to the fact that annihilating or decaying dark matter in the Milky Way halo has an isotropic component equal to the minimum of the annihilation or decay signal. This minimum is equal to the amount toward the anti-Galactic Center.

The isotropic DGRB has several potential astrophysical source contributions, including blazars [135, 148, 192, 193], starburst galaxies [138] and millisecond pulsars [139]. The only model that successfully predicts the shape and amplitude of the DGRB over all energies is the luminosity-dependent density evolution (LDDE) blazar spectral energy density (SED) sequence model with an active galactic nuclei (AGN) contribution [30, 136]. The SED-sequence model matches the shape of the observed blazar SED's luminosity dependence [161, 162, 164]. Reference [136] reproduces well the DGRB as observed by Fermi-LAT, while several other analyses under-produce the DGRB from blazars. Reference [136] estimates that $\gtrsim 98\%$ of the blazar flux contributing to the DGRB will be resolved in the 5-year Fermi-LAT survey. Prior work that under-produces the DGRB uses a single power-law for the

spectrum of all blazars instead of the observed SED sequence for blazars, e.g [131]. Other recent work with varied blazar population models, including spectral shape variation [188], possible point source confusion [189], and BL Lac dominance of the unresolved portion [190] also find that a substantial portion of the DGRB could arise from the blazar population.

There may also be an unmodeled, unreduced isotropic Galactic component to the DGRB [130, 133]. It should be noted that two things could happen if there is a presently unremoved Galactic isotropic diffuse component: one, it is detected, modeled, and removed, which will make future constraints stronger; or, two, it remains a systematic diffuse background, which means our starting assumption of an LDDE SED-sequence model is not the correct model for the DGRB. However, this uncertainty cannot be removed without further observational analysis.

Below, we calculate and show the current constraints from the DGRB on dark matter annihilation and decay gamma-rays from the prompt as well as inverse-Compton components. In addition, when adopting the LDDE plus SED-sequence model forecasts of the Fermi-LAT resolved DGRB, future observations will extend the reach of Fermi-LAT sensitivity to dark matter typically by a factor of 2 to 3. We explore in detail the forecasts on standard WIMP dark matter and leptonic-channel motivated models [54, 57] including Asymmetric Dark Matter models [194, 195], nonthermal winolike dark matter [81, 196], and decaying dark matter [69], as well as models of light ($\sim$8 GeV) WIMP dark matter in scalar dark matter models [197–199]. The resolution of the DGRB into point source blazars will reduce the DGRB amplitude and ultimately enhance the limits on annihilation in WIMP dark matter

models.

In a companion paper, Ref. [30] (ABH2), we constrain our adopted SED-sequence model using the observed DGRB spectrum as well as the observed blazar source count distribution function, dN/dF. In agreement with Ref. [136], ABH2 found that $\gtrsim 95\%$ of the flux from blazars will be resolved with 5 years of Fermi-LAT observation. The resolution of the DGRB is in fact similar to the resolution of the cosmic x-ray background observed by *Chandra*, which in turn provided stringent constraints on decaying light sterile neutrino dark matter [200].

The work presented here advances previous work on prompt gamma-ray emission in annihilating dark matter (e.g., [36]) by including the enhanced constraints and sensitivity from inverse-Compton (IC) emission present in the Fermi-LAT observation of the DGRB as well as forecasts of the improvement of this sensitivity. In addition, we go beyond previous analyses of IC emission enhancement of the extragalactic and Galactic signals (e.g., [69, 201]) by applying the IC enhancement in the Fermi-LAT observation of the DGRB and its forecast improvement.

5.2 The Blazar Population and SED-sequence model

The SED-sequence model specifies the cosmological blazar spatial distribution and spectrum for a given blazar luminosity. It is based on the observed evolution of the peak flux in synchrotron and IC emission with luminosity. The luminosity-dependent density evolution model specifies the gamma-ray luminosity function of blazars through a fraction of the total AGN population and its x-ray luminosity

function. Our blazar population and SED-sequence model in ABH2 successfully reproduces the observed DGRB and blazar source count dN/dF.

Our model is a modification of that by Inoue and Totani [135], and is detailed in ABH2. We provide a summary here. The bolometric blazar jet luminosity P and disk x-ray luminosity L_X are related by $P = 10^q L_X$. The blazar gamma-ray redshift-dependent luminosity function is given as a fraction κ of the AGN x-ray luminosity function (XLF), $\rho_\gamma(L_\gamma, z) = \kappa(dL_X/dL_\gamma)\rho_X(L_X, z)$. We adopt the AGN XLF of Ueda et al. [165]. The main fit parameter in the XLF is the faint-end slope index, γ_1. The model also includes a nonblazar AGN component which dominates at lower energies, $E_\gamma \lesssim 1$ GeV.

In ABH2, we constrain the blazar population model by simultaneously fitting the DGRB spectrum as well as the blazar flux source count distribution function dN/dF observed by Fermi-LAT [130, 131]. The best fit parameters we find are $q = 4.19^{+0.57}_{-0.13}$, $\log(\kappa/10^{-6}) = 0.38^{+0.15}_{-0.70}$, and $\gamma_1 = 1.51^{+0.10}_{-0.09}$. These are consistent with previous work [135], though more constrained because we are also fitting the source count distribution function dN/dF. The model reproduces the DGRB and blazar dN/dF, with a reduced $\chi^2/\mathrm{DOF} = 0.63$.

Using the dN/dF estimated from a power-law blazar spectrum model is not perfect, since the efficiency depends on this model [131]. However, Ref. [131] tested the dN/dF estimate with a non-power-law fit to the blazar spectra and found it did not appreciably change the estimates of dN/dF, adding a systematic uncertainty of 10%. We also checked this sensitivity with a test fit by increasing the errors on the measured dN/dF at low flux and our model did not prefer a different amplitude or

shape to the source counts at the low flux where the efficiency for blazar detection is low.

Our model fits the current DGRB, and, furthermore, predicts the DGRB for the expected enhanced sensitivity to point sources after 5 years of Fermi-LAT data, 2×10^{-9} photons cm^{-2} s^{-1}, which will resolve $94.7^{+1.9}_{-2.1}$% of the flux from blazars. This expected enhanced point source sensitivity value is the Fermi-LAT Collaboration's estimate of the LAT flux sensitivity to point sources at high-latitude with gamma-ray index of $\sim$2 [186].[1] In ABH2, we find the 68% and 95% confidence level (C.L.) upper and lower limit forecasts for the DGRB $E^2 d\Phi/dE$ when varying the fit parameters. This model finds that the DGRB will reduce by a factor of 1.6-2.6 (95% C.L.) with the spatial point-source resolution of the blazar contribution, after five years of the Fermi-LAT mission. The current and forecast spectra are shown in figure 5.1. In our forecasts, we calculate the limits using the flux as predicted by the model at the minimal and maximal values, not simply performing a scaling of the limits.

From the first to second Fermi source catalogs, there were 162 potentially spurious sources designated, indicating the sources' further identification with a spatially extended source, source variability, or other systematic effects [202]. The catalogs include sources with the test statistic $TS = 25$, while the Fermi-LAT DGRB analysis only removed sources with $TS = 50$, or with higher significance. (For the definition of TS, see Eq. 20 of Ref. [203].) This type of spurious contamination may alter forecasts for the DGRB, though the higher significance required for the exclusion of sources in the DGRB spectrum would likely reduce or eliminate this

[1] http://fermi.gsfc.nasa.gov/science/resources/aosrd/

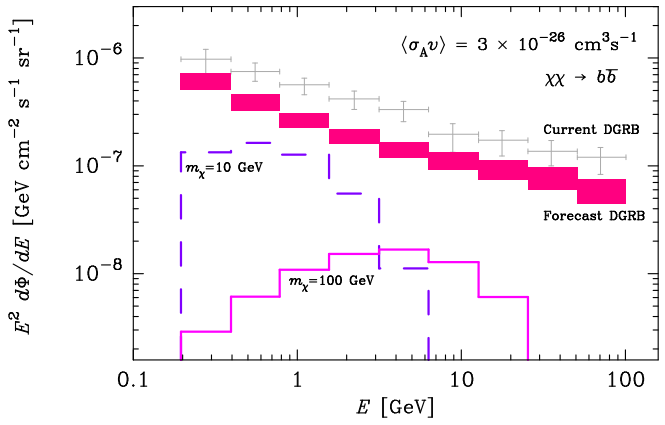

Figure 5.1: Shown are the current Fermi-LAT observed DGRB [130] in grey, and the forecast DGRB upper and lower 95% C.L. central values as the boxed (magenta) regions. Also shown are the expected emission from the Galactic and extragalactic contribution for WIMP annihilation into $b\bar{b}$ for the WIMP particle masses 10 GeV and 100 GeV, for the canonical $\langle\sigma_{\rm A} v\rangle = 3 \times 10^{-26}$ cm^3 s^{-1}.

systematic effect.

5.3 Current and Future Sensitivity to Dark Matter Models of the Fermi-LAT DGRB

The signal constrained by observations of the DGRB is the annihilation or decay of dark matter both in the Milky Way Galaxy and extragalactically. There is an irreducible contribution to the background from Galactic annihilation or decay that is isotropic and equal, at minimum, to the emission from the Anti-Galactic-Center (AGC). Here we examine in detail constraints on annihilating and decaying dark matter from both prompt and IC emission of photons.

5.3.1 Diffuse Emission from Annihilating Dark Matter

The products of dark matter annihilation emit in gamma-rays in several ways: annihilation channels that include the direct emission of a photon, decay of annihilation products into photons, and IC scattering of daughter electrons off of background radiation. Through loop contributions to the annihilation cross section of dark matter, it is possible to have a direct $\gamma\gamma$ line signal, through a typically small branching fraction. If the dark matter annihilation particles include hadrons, then the decay chain of the products will lead to neutral pion decay into photons. Additionally, electrons among the dark matter annihilation daughters will up-scatter background photons from the cosmic microwave background (CMB) and starlight to gamma-ray energies through IC scattering. We will consider the latter two cases in this paper: photons from prompt radiation in bremsstrahlung and hadronization, and IC emission from electron daughter particles. We calculate the photon and electron spectrum from annihilation using the software PYTHIA [10]. To be conservative, we only consider IC emission from the CMB, not starlight or the infrared (IR) background, which is a good approximation in the direction of the AGC that we will consider.

There are two sources of dark matter that contribute to the DGRB, Galactic and extragalactic dark matter. The signal from Galactic dark matter is largest in the line-of-sight toward the Galactic Center and is much smaller in other directions. However, there is an irreducible, isotropic signal from the Galactic dark matter that is equal to the signal from the AGC. This isotropic signal can be the strongest

dark matter contributor to the DGRB given conservative assumptions about the extragalactic contribution [40].

To calculate the dark matter annihilation flux for a given cross section $\langle \sigma_A v \rangle$ and photon spectrum dN_γ/dE, we follow the treatment of Ref. [36]. The Galactic contribution to the diffuse flux is given by:

$$\frac{d\Phi_\gamma}{dE d\Omega} = \frac{\langle \sigma_A v \rangle}{2} \frac{\mathcal{J}(\mathrm{AGC})}{\mathrm{J}_0} \frac{1}{4\pi m_\chi^2} \frac{dN_\gamma}{dE}, \tag{5.1}$$

$$\mathcal{J}(\mathrm{AGC}) = \frac{1}{\Delta\Omega_{\mathrm{obs}}} \int_{\Delta\Omega_{\mathrm{obs}}} \mathcal{J}(0, 180^\circ) d\Omega, \tag{5.2}$$

$$\mathcal{J}(b, \ell) = \mathrm{J}_0 \int_{x_{\mathrm{min}}}^{x_{\mathrm{max}}} \rho^2 \left(r_{\mathrm{gal}}(b, \ell, x) \right) dx, \tag{5.3}$$

$$r_{\mathrm{gal}}(b, \ell, x) = \sqrt{R_\odot^2 - 2 x R_\odot \cos(\ell) \cos(b) + x^2}, \tag{5.4}$$

evaluated conservatively at the AGC ($b = 0^\circ$, $\ell = 180^\circ$). In these equations, m_χ is the dark matter particle mass, x is the line-of-sight distance, $R_\odot$ is the distance from the Galactic Center to the sun, and $\mathrm{J}_0 \equiv 1/[8.5\ \mathrm{kpc}(0.3\ \mathrm{GeV\ cm^{-3}})^2]$ is an arbitrary constant that cancels in the final expression for flux. For the Fermi-LAT, the solid angle above $|b| > 10^\circ$ has $\Delta\Omega_{\mathrm{obs}} = 10.4$. The quantity $\mathcal{J}$ is the dark matter density squared integrated along the line of sight, and $\mathcal{J}(\mathrm{AGC})$ is this value averaged over the observed angular sky region. For dark matter density ρ we use the minimal Einasto profile for the Milky Way halo:

$$\rho_{\mathrm{Einasto}}(r) = \rho_s \exp\left[-\frac{2}{\alpha_E} \left(\left(\frac{r}{r_s} \right)^{\alpha_E} - 1 \right) \right], \tag{5.5}$$

with $\alpha_E = 0.22$, $r_s = 21$ kpc, $r_\odot = 8.28$ kpc, and $\rho_\odot = 0.385$ GeV cm^{-3} as in Ref. [36]. This profile is a conservative choice and gives $\mathcal{J}(\mathrm{AGC}) = 0.62$, and extreme assumptions about the Milky Way dark matter profile only change this

value by $\sim 10\%$.

The Milky Way dark matter halo has abundant substructure which enhances the annihilation rate of dark matter. Following Ref. [82], the boost factor for the annihilation due to substructure is

$$\begin{aligned} B(r) &= f_s e^{\Delta^2} \\ &\quad +(1-f_s)\frac{1+\alpha}{1-\alpha}\left[\left(\frac{\rho_{\max}}{\rho_h}\right)^{1-\alpha}-1\right]. \end{aligned} \tag{5.6}$$

The fraction f_s of the halo volume is filled with a smooth dark matter component with density ρ_h. The maximal density of the PDF $\rho_{\max}$ is taken to be the scale density ρ_s of the earliest forming halos. The first term in Eq. (5.6), $f_s e^{\Delta^2}$, is due to the variation in the smooth component, which contributes only a few percent to the boost, and therefore we ignore it. The second term is the boost factor due to substructure. The total luminosity boost due to the entire Galactic halo within radius R is

$$B(<R) = \frac{\int_0^R B(r)\rho(r)^2 r^2 dr}{\int_0^R \rho(r)^2 r^2 dr}, \tag{5.7}$$

where r is the halo-centric radial coordinate. The annihilation rate is larger in all directions than the AGC, therefore we calculate the luminosity with boost along that line of sight as the minimal annihilation rate due to our Galactic halo. Along the line-of-sight,

$$\mathcal{J}_{\rm boost}(b,\ell) = \mathrm{J}_0 \int_{x_{\min}}^{x_{\max}} B(r_{\rm gal}(b,\ell,x))\rho^2\left(r_{\rm gal}(b,\ell,x)\right) dx. \tag{5.8}$$

There is a partial reduction of the total luminosity boost [Eq. (5.7)] along the line of sight to the AGC due to our presence within the Galactic halo. Using the central

value of $\alpha = 0$ from simulations, the boost is $B_{\rm AGC} \equiv \mathcal{J}_{\rm boost}({\rm AGC})/\mathcal{J}({\rm AGC}) = 3.3$. Though the boost factor toward the Galactic Center is expected to be unity [82], that from the total Galactic halo can approach ∼20 to 2000. Therefore, the approximation of a total Galactic boost in the DGRB field of view as 3.3 is conservative.

In addition to this Galactic contribution to the dark matter flux, we include a subdominant contribution from extragalactic dark matter annihilations [204, 205]. This contribution is given by

$$\frac{d\Phi_\gamma}{dEd\Omega} = \frac{\langle\sigma_A v\rangle}{2}\frac{c}{4\pi H_0}\frac{(f_{\rm DM}\Omega_m)^2\rho_{\rm crit}^2}{m_\chi^2}\times \int_0^{z_{\rm up}}\frac{f(z)(1+z)^3 e^{-\tau(z,E')}}{\sqrt{(1+z)^3\Omega_m+\Omega_\Lambda}}\frac{dN(E')}{dE'}dz, \tag{5.9}$$

where H_0 is the Hubble constant, Ω_m is the matter density in units of the critical density, $\rho_{\rm crit}$, and the fraction of matter in dark matter is $f_{\rm DM} = \Omega_{\rm DM}/(\Omega_{\rm DM} + \Omega_b) \approx 0.833$, where we take the fraction of critical density of the dark matter as $\Omega_{\rm DM} = 0.237$, and baryon density $\Omega_b = 0.0456$ [2]. Here, $E' = E(1+z)$ is the source energy of the photons, and $z_{\rm up} = (m_\chi/E) - 1$ is the maximum redshift to get a photon with energy E. The factor $f(z)$ accounts for the increase in density squared during halo growth and the redshift evolution of the halo mass function. We adopt the fit of Refs. [205–207], namely:

$$f(z) = f_0 10^{0.9[\exp(-0.9z)-1]-0.16z}. \tag{5.10}$$

For the Einasto profile, $f_0 \simeq 3\times10^4$. We also include the boost factor of 6.6, from the total luminosity of a halo $B(<R)$. This extragalactic contribution only accounts for $\lesssim 30\%$ of the total diffuse flux from dark matter.

To calculate the limits on $\langle \sigma v \rangle$, we attribute all the DGRB to dark matter annihilation (or decay), including both the Galactic and extragalactic dark matter contributions. This provides an upper limit on the cross section of annihilating dark matter (or a lower limit on the lifetime of decaying dark matter). We use the upper and lower 68% and 95% C.L. forecast fluxes corresponding to the extremal upper and lower fluxes in the three-dimensional contour in q, κ and γ_1 parameter space, as constrained by the DGRB spectrum and source count distribution function, as described in our companion paper [30]. We take errors on the forecast DGRB for all of the upper and lower 68% and 95% C.L. forecast fluxes each to be proportional to its amplitude, which corresponds to the modeling methods of the DGRB measurement, though this is not necessarily the ultimate scaling of the errors. To do so, a Monte Carlo of the modeling methods of Ref. [130] would need to be performed, which is beyond the scope of this work.

Figure 5.2 demonstrates the forecast for four canonical dark matter annihilation channels and how they compare to expected minimal supersymmetric model (MSSM) and minimal supergravity (mSUGRA) dark matter cross sections. The cross sections are from a scan in MSSM and mSUGRA parameter space by Ref. [208]. Note that our predicted constraints from Fermi-LAT's observations of the DGRB are comparable to current constraints Fermi-LAT observations of the Galactic Center [69], shown as a dashed line in figure 5.2. For comparison, in figure 5.2 we also show constraints from the Fermi-LAT analysis of stacked dwarf galaxies [44, 45]. The constraints shown are from Ref. [44]. In all relevant panels, we also show constraints from the HESS observation of the Galactic Center [33] as calculated in Ref. [28].

It has been proposed that a nonthermally-produced winolike dark matter annihilation could lead to the positron excess signal in PAMELA, which requires wino dark matter masses of 100 GeV $\lesssim m_\chi \lesssim$ 200 GeV [81, 196]. As shown in figure 5.2(b), these models are disfavored by the current constraints, and the forecast spectrum will be significantly more sensitive to this model.

The standard thermal relic weakly-interacting dark matter annihilation cross section is $\sim 3\times10^{-26}$ cm^3 s^{-1} [211–213], which corresponds roughly with the broader MSSM/mSUGRA region. The plot of dark matter annihilating into $\tau^+\tau^-$, figure 5.2(d), contains a region in parameter space which has recently been claimed to be consistent with the morphology and spectrum of excess gamma-ray flux towards the Galactic Center [210], though such a signal is also consistent with emission from stellar clusters [214]. The width of the forecast region follows from the increasing width of the DGRB prediction with energy. Our model predicts a factor of $2-3$ (95% C.L.) improvement in the sensitivity of the DGRB measurement to dark matter.

5.3.2 Diffuse Emission from Annihilation of Dark Matter into Leptonic Modes and IC

Dark matter that annihilates into leptons has been proposed as an explanation for an excess in cosmic-ray positrons seen by the PAMELA Collaboration [46] and a feature in the cosmic-ray e^+/e^- spectrum from the Fermi-LAT [50, 65, 108]. The DGRB is forecast to be sensitive to direct $\mu^+\mu^-$ production models that fit

the PAMELA excess and Fermi-LAT e^+/e^- feature, such as Asymmetric Dark Matter [194, 195]. Such direct annihilation models are already strongly disfavored by constraints of observations by the Galactic Ridge by HESS [35, 36, 38], observations by Fermi-LAT toward the Galactic Center [69], and HESS toward the Galactic Center [28, 33]. The latter two constraints shown in figure 5.3.

It has also been suggested that Sommerfeld-enhanced dark matter annihilation into four leptons, via a light mediator particle, could explain these signals. Therefore, we also consider how an improved DGRB will affect these leptonic dark matter annihilation channels. Note that such models are also constrained by detailed calculations of the relic abundance from dark matter production in the early Universe and halo shapes [60], as well as distortions of the CMB spectrum [62, 217]. Recent work finds that several reasonable parameter choices in models of Sommerfeld-enhanced dark matter for PAMELA and the Fermi-LAT e^+/e^- spectral feature avoid these limits [66]. These Sommerfeld-enhanced models are partially constrained by the current limits and will be further constrained by our forecast limits, as shown in figure 5.3(b).

Dark matter annihilation into leptons produces fewer photons than the quark or gauge boson channels. However, such annihilations do produce highly-boosted electrons which undergo IC scattering on the CMB and starlight which is then observable in gamma-rays. We calculate this IC contribution as in Ref. [69]. To be conservative, we only include the scattering from the CMB, not from starlight or the IR background.

The spectrum of IC photons coming from one dark matter annihilation is given

by [69, 201]

$$\frac{dN}{dE} = \frac{1}{E}\int_{m_e}^{m_\chi} d\epsilon \frac{\mathcal{P}(E,\epsilon)}{\dot{\mathcal{E}}(\epsilon)} Y(\epsilon), \tag{5.11}$$

where $\mathcal{P}(E,\epsilon)$ is the differential power emitted into photons of energy E by an electron with energy ϵ, $\dot{\mathcal{E}}$ denotes the total rate of electron energy loss due to IC scattering, and $Y(\epsilon)$ is the number of electrons generated with energy larger than ϵ in one annihilation. To get the energy of the annihilation products, we use the software PYTHIA [10]. In the Thomson limit, which is a very good approximation for CMB photons, one obtains

$$\dot{\mathcal{E}}(\epsilon) = \frac{4}{3}\sigma_T \gamma^2 \int_0^\infty d\epsilon' \epsilon' n(\epsilon') \tag{5.12}$$

$$\mathcal{P}(E,\epsilon) = \frac{3\sigma_T}{4\gamma^2} E \int_0^1 dy \frac{n(\epsilon'(y))}{y} \times \left(2y\ln y + y + 1 - 2y^2\right), \tag{5.13}$$

where γ is the Lorentz factor of the electron, ϵ' is the energy of the initial CMB photon, $y \equiv E/(4\gamma^2\epsilon')$, $\sigma_T \simeq 0.665$ barn is the Thomson cross section, and the radiation density of CMB photons at $T_{\rm CMB} \simeq 2.725$ K is given by

$$n_{\rm CMB}(\epsilon') = \frac{\epsilon'^2}{\pi^2} \frac{1}{\exp(\epsilon'/T_{\rm CMB}) - 1}. \tag{5.14}$$

The flux coming from the IC contribution can then be calculated as in Eqs. (5.1)-(5.10).

It is important to note that we are neglecting the diffusion of the electrons and positrons from the dark matter annihilation to the point where IC scattering occurs. As stated in Ref. [69], this is a good approximation in regions away from the Galactic Center, as we consider in this work. For an analysis where diffusion is included, see

Ref. [216]. To be more explicit, in Ref. [78], it was shown that the electron/positron flux produced by dark matter annihilations was only slightly modified by diffusion effects for distances from the Galactic Center larger than 8 kpc. Corrections were found to reach a factor of 2 only at the lowest energies around 100 MeV (see their figure 14). Therefore, diffusion effects are not significant in our calculation of the IC component. Note that the IC component is modeled in the measurement if the DGRB independent of the observation [130], so there is no accidental subtraction of a potential IC signal.

Our calculations for the standard $\mu^+\mu^-$ leptonic channel are shown in figure 5.3(a). Also shown are the regions which are consistent with the PAMELA excess and Fermi-LAT e^+/e^- spectral feature from Ref. [215], modified for a higher local dark matter density of our minimal Einasto halo model ($\rho_\odot = 0.385$ GeV cm^{-3}), and the local boost of $B(r = R_\odot) = 1.57$ [Eq. (5.6)] from substructure. For this boost, we use the same parameters for the subhalo PDF as our subhalo boost annihilation signal. Such models are already highly constrained by several gamma-ray observations as shown in figure 5.3(a), and such models will be further constrained with our forecast DGRB sensitivity. Note that the IC contribution improves the bounds by several orders of magnitude. The IC gamma-ray flux contribution peaks at much lower energies than the prompt component for a given dark matter particle mass, which is why the width of the forecast region decreases when the IC component becomes important. Also shown in figure 5.3 are complementary limits on the cross section of $\mu^+\mu^-$-channel annihilating dark matter from other work. Shown in figure 5.3(b) is dark matter annihilation into four muons via intermediate scalars ϕ

with 0.3 GeV masses. Even in this less-constrained case, our forecast is that the Fermi-LAT measurement of the DGRB will have the sensitivity to detect or rule out a portion of the parameter space the dark matter interpretations of PAMELA.

5.3.3 Diffuse Emission from Decaying Dark Matter

Decaying dark matter is another, less constrained, possibility for the source of the positron fraction signal seen in PAMELA and the Fermi-LAT e^+/e^- spectral feature [69]. To calculate the flux from decaying dark matter with lifetime τ and photon spectrum dN_γ/dE, the procedure is very similar to the annihilating dark matter case. However, in Eq. (5.3), $\rho^2 \to \rho$ and there is no boost factor due to the lack of decay enhancement with density. Here, Eq. (5.1) becomes

$$\frac{d\Phi_\gamma}{dEd\Omega} = \frac{1}{\tau}\frac{\mathcal{J}_{\rm AGC}}{\rm J_0}\frac{1}{4\pi m_\chi}\frac{dN_\gamma}{dE}. \tag{5.15}$$

Similarly, to calculate the extragalactic flux from decaying dark matter, in Eq. (5.9) replace

$$\frac{\langle\sigma_A v\rangle}{2}\frac{(f_{\rm DM}\Omega_m)^2\rho_{\rm crit}^2}{m_\chi^2} \to \frac{1}{\tau}\frac{(f_{\rm DM}\Omega_m)\rho_{\rm crit}}{m_\chi} \tag{5.16}$$

and drop all boost factors.

Figure 5.4 shows how the predicted DGRB value will constrain the lifetime of a dark matter particle which decays into $\mu^+\mu^-$. The improved constraint will have the sensitivity to exclude or detect the decaying dark matter interpretation of the Fermi-LAT e^+/e^- feature and should provide strong limits on an interpretation of the PAMELA excess [46, 216]. The DGRB limit is comparable to and is forecast to be more sensitive than the limits on decaying dark matter from Fermi-LAT observations

of clusters of galaxies [218], as shown in figure 5.4.

5.3.4 Comparison to Direct Dark Matter Detection Limits on Light Dark Matter

Dark matter may be detected through two distinct methods: indirect-detection experiments seek the annihilation or decay products from dark matter in the Universe, while direct-detection experiments look for the recoil of heavy nuclei after their collision with a dark matter particle from our Galactic halo. In general, the interaction cross section between annihilating dark matter is not simply related to the interaction cross section between dark matter and nucleons. A few recent direct-detection experiments, however, have seen signals that could be caused by a light dark matter particle, including DAMA [221–223, 225], CoGeNT [220] and CDMS [224].

These light dark matter signals could be due to dark matter that interacts through the exchange of Higgs bosons [197–199]. For such a dark matter candidate, the indirect annihilation cross section and direct nuclear cross section are related by

$$\sigma_{\rm ind}(SS \to \bar{f}f)\frac{v}{c} = n_c \frac{\lambda_L^2}{\pi}\frac{m_f^2(m_S^2-m_f^2)^{3/2}}{m_h^4 m_S^3} \quad (5.17)$$

$$\sigma_{\rm dir}(SN \to SN) = \frac{\lambda_L^2}{\pi}\frac{\mu_r^2}{m_h^4 m_S^2} f^2 m_N^2 \quad (5.18)$$

$$\sum \frac{\sigma_{\rm ind}}{\sigma_{\rm dir}}\frac{v}{c} = \sum \frac{n_c m_f^2}{f^2 m_N^2}\frac{(m_S^2-m_f^2)^{3/2}}{\mu_r^2 m_S}, \quad (5.19)$$

where m_h is the Higgs mass, λ_L is the dark matter-Higgs coupling, $n_c = 3(1)$ for quarks (leptons), μ_r is the dark matter-nucleon reduced mass, $f \sim 0.3$, and m_S is the dark matter mass [197, 198]. The sum in Eq. (5.19) is over all annihilation products,

which are dominated by the b-quark, the c-quark, and the τ-lepton. Through this ratio, we can relate our predicted DGRB limits on indirect detection into limits on direct-detection experiments. For such a Higgs-mediated dark matter model, we compare our projected limit to the findings of several direct-detection experiments in figure 5.5.

The limit on the dark matter-nucleon cross section as found by our DGRB forecast is competitive with the limits by the XENON100 Collaboration in the lowest mass range [219]. The current Fermi-LAT DGRB values rule out the DAMA region without channeling and some of the region consistent with a dark matter interpretation of CoGeNT. After a Fermi-LAT 5-year run, we forecast the DGRB spectrum to have the sensitivity to exclude most of the CoGeNT region consistent with dark matter interpretations in the spin-independent case. This is complementary to the findings of direct-detection experiments since the DGRB indirect-detection limits tend to exclude lower dark matter masses than direct-detection experiments.

5.4 Conclusions

The DGRB as measured by Fermi-LAT is one of the most powerful constraints on annihilating weak-scale particle dark matter. We show that the likely resolution of blazars into point sources by Fermi-LAT—and their automatic removal from the DGRB measurement—will enhance the sensitivity of the DGRB to dark matter annihilation by a factor of 2 to 3 (95% C.L.), depending on the channel, mass scale, and true realization of the blazar distribution and SED sequence.

We find the forecast dark matter sensitivity of the DGRB observation to both prompt and inverse-Compton photon emission to be comparable in sensitivity with other limits on annihilating weak-scale dark matter. The DGRB is forecast to be comparable to current limits from Fermi-LAT observations toward the Galactic Center [69], individual dwarf galaxies [209], and, in the case of decaying dark matter, observations of clusters of galaxies [218]. This sensitivity makes the DGRB among the best methods of detecting or constraining dark matter with the Fermi-LAT mission. The forecast for the DGRB projects it to be less constraining, for certain channels and particle masses, than current stacked dwarf analyses with Fermi-LAT [44, 45] and observations of the Galactic Center by HESS [28, 33].

The future resolution and reduction of the DGRB into blazar point sources highlights and enhances the possibility that the Fermi-LAT experiment will either detect or constrain the dark matter in a robust yet conservative way.

Figure 5.2: Shown are our predictions for the Fermi-LAT sensitivity to constraints on dark matter in several canonical annihilation channels: (a) $\chi\chi \to b\bar{b}$; (b) $\chi\chi \to W^+W^-$; (c) $\chi\chi \to t\bar{t}$; (d) $\chi\chi \to \tau^+\tau^-$. The blue double and single hashed regions are the 68% and 95% C.L. predictions for 5-year Fermi-LAT sensitivity, respectively. Also shown is the limit from the current Fermi-LAT DGRB spectrum (solid blue). In panel (a), we also show the current constraints from Fermi-LAT observations of Draco (thick dotted line) [209]. In panels (a), (b) and (d), we show constraints from the stacking of dwarf galaxies (thin dotted line) [44]. In the W^+W^- channel, panel (b), the cross section versus mass for a nonthermal winolike neutralino is shown. The winolike dark matter of the PAMELA signal at $m_\chi \sim 200$ GeV [81, 196] is disfavored by the current constraints and will be further constrained in the forecast spectrum. The 'MSSM/mSUGRA' red-striped region is the expected cross sections for a sampling of points in supersymmetric parameter space [208]. The dashed line is a limit from the $3^\circ \times 3^\circ$ in the Galactic Center [69]. In the $\tau^+\tau^-$ plot, panel (d), the green box is a region that could be consistent with an excess in the spectrum toward the Galactic Center [210]. In all panels, the triple-dot-dashed line is the limit from the HESS observation of the Galactic Center [33] for the respective channels in the case of a Navarro-Frenk-White halo profile, from Ref. [28].

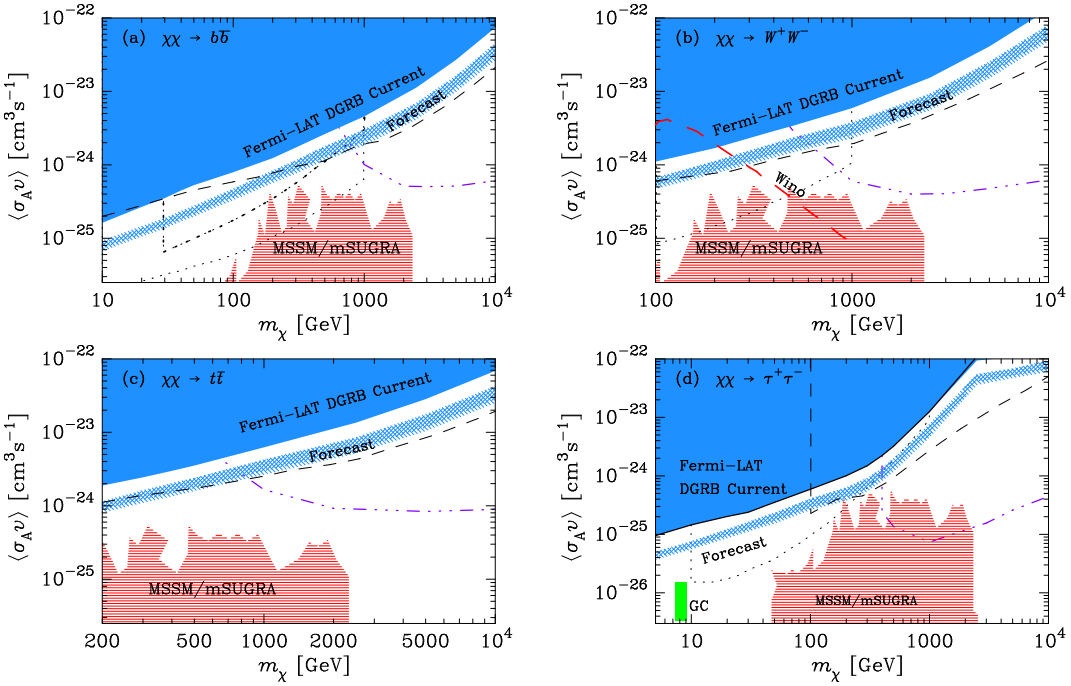
(a) $\chi\chi \to b\bar{b}$
(b) $\chi\chi \to W^+W^-$
(c) $\chi\chi \to t\bar{t}$
(d) $\chi\chi \to \tau^+\tau^-$
Fermi-LAT DGRB Current
Forecast
MSSM/mSUGRA
Wino
GC
$\langle\sigma_A v\rangle$ [cm^{3}s^{-1}]
m_χ [GeV]

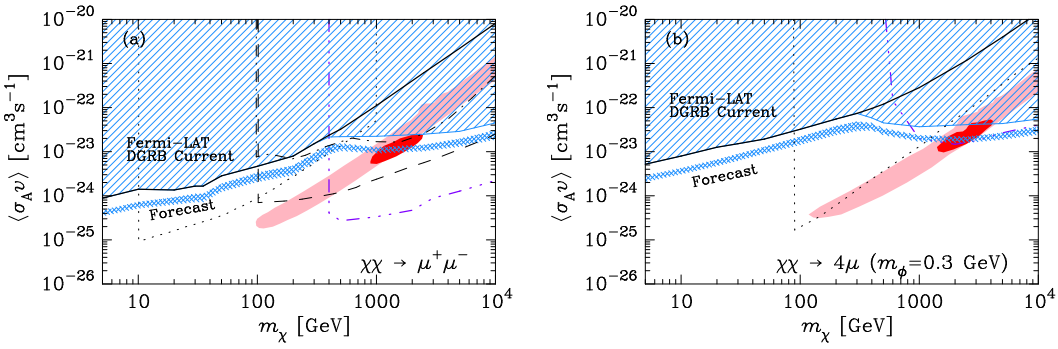

Figure 5.3: Shown in panel (a) are our predictions for Fermi-LAT sensitivity to $\mu^+\mu^-$ channel dark matter annihilation. The dot-dashed line is the 95% C.L. limit on prompt and IC emission from Ursa Minor [209]. In this panel, we show the constraint from the stacking of dwarf galaxies (thin dotted line) [44]. In panel (b), dark matter annihilation into four muons via intermediate 0.3 GeV scalar particles ϕ. The blue double and single hashed regions are the 68% and 95% C.L. predictions for 5-year Fermi-LAT sensitivity, respectively. Also included is the limit from the current Fermi-LAT DGRB spectrum (striped blue region). The solid black line shows where the exclusion would be without the IC contribution. The light pink shaded region is consistent with a dark matter interpretation of the PAMELA signal and the dark red shaded region is consistent with a dark matter interpretation of the Fermi-LAT e^+/e^- feature [215, 216]. The triple-dot-dashed line is the limit from the HESS observation of the Galactic Center [33] for the respective channels in the case of a Navarro-Frenk-White halo profile, from Ref. [28]. In panel (b), the dotted line is a limit on dark matter annihilation from radio synchrotron from the Galactic Center [215]. The dashed line is the 99% C.L. limit from the $3^\circ \times 3^\circ$ region toward the Galactic Center [69].

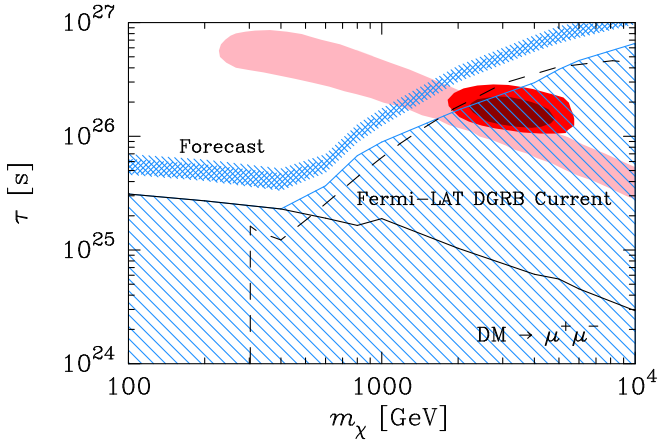

Figure 5.4: Our predictions for Fermi-LAT sensitivity to dark matter decaying into $\mu^+\mu^-$. The dark and light blue hashed regions are the 68% and 95% C.L. predictions for 5-year Fermi-LAT sensitivity, respectively. Also included is the limit from the current Fermi-LAT DGRB spectrum (blue striped region). The solid black line shows where the exclusion would be without the IC contribution. The light pink shaded region is consistent with a dark matter interpretation of the PAMELA signal, and the dark red shaded regions are consistent with a dark matter interpretation of the Fermi-LAT e^+/e^- feature at 3- and 5-σ [216]. The dashed line is from constraints on prompt and IC emission from dark matter annihilation made from Fermi-LAT observations of the Fornax cluster of galaxies [218].

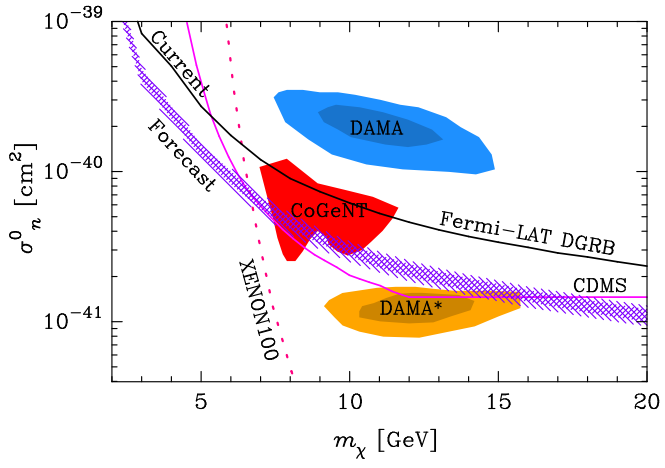

Figure 5.5: Our predictions for Fermi-LAT sensitivity to light dark matter coupled via Higgs-like couplings [197, 198]. The dark and light purple hashed regions are the 68% and 95% C.L. predictions for 5-year Fermi-LAT sensitivity, respectively. Also included is the limit from the current Fermi-LAT DGRB spectrum (black line). To the right of the dotted pink line is exclusion from the XENON100 Collaboration [219]. The red "CoGeNT" region is consistent with the findings of the CoGeNT Collaboration [220]. The blue upper "DAMA" region is the DAMA signal without channeling [221]. The orange lower "DAMA*" region is the DAMA signal if channeling is included [222, 223]. The region labeled "CDMS" is excluded by that experiment's light dark matter search at 95% C.L. [224].

Chapter 6

The Sensitivity of HAWC to High-Mass Dark Matter Annihilations

6.1 Introduction

The effects of dark matter has been seen in many observations: galaxy clusters, galactic rotation curves, the cosmic microwave background, large-scale cosmological structure, and gravitational lensing around dwarf spheroidal galaxies. The particle nature of the dark matter remains unclear, however (for a review of dark matter particle candidates, see, e.g. [32]). Of the candidates which have been considered, the weakly-interacting massive particle (WIMP) is perhaps the best-motivated. A thermal relic WIMP with TeV-scale mass with a weak-scale cross-section $\langle \sigma_{\mathrm{A}} v \rangle \approx 3 \times 10^{-26}$ cm^3 s^{-1} produces the dark matter relic density observed in nature. In areas of high dark matter density, WIMPs can annihilate into Standard Model particles and produce photons via pion decay, radiative processes by charged leptons, or direct production of gamma-rays through loop-order processes. The detection of these dark matter annihilation products is referred to as "indirect detection" of dark matter, and can be used to constrain the mass, annihilation spectrum, and annihilation cross-section of the dark matter.

The High Altitude Water Cherenkov (HAWC) observatory is a high-energy gamma-ray observatory currently being installed at Sierra Negra, Mexico. The site is 4100 m above sea level, at latitude 18°59′41″N and longitude 97°18′28″W.

The water Čerenkov design has previously been used successfully with the Milagro Gamma-Ray Observatory for observations of the Galactic plane and point sources with emission energies above 1 TeV [226, 227]. HAWC will consist of a 22000 m^2 array of 5 m high water tanks. Each tank will contain four photo-multiplier tubes for observing the Čerenkov light emitted by charged particles passing through the water. [228, 229].

Water Čerenkov detectors work by observing the particles from the air shower associated with a high-energy cosmic ray or gamma-ray entering the atmosphere. Unlike air Čerenkov detectors, water Čerenkov detectors do not directly measure the Čerenkov light given off by the air shower, but rather measure the Čerenkov light given off inside each detector when the air shower hits it. Also unlike air Čerenkov detectors, water Čerenkov detectors have a wide field of view and can operate continuously. Because the detector is effective during daylight and regardless of weather, it has a much longer observation time than Air Čerenkov detectors. The effective field-of-view is usually limited to within 45° of the zenith, but can in principle observe photons coming from the entire hemisphere of the sky [228, 229]. This large field-of-view eliminates the need for pointed observations, allowing the observatory to detect in multiple locations at once.

HAWC is expected to be $\sim$ 15 times more sensitive than Milagro, with a 1-year sensitivity of 50 mCrab for hard-spectrum Galactic point-sources. As designed, the field-of-view will be 2 sr, with more than 7 sr observable each sidereal day. The angular resolution above 5 TeV will be better than 0.25°, with resolutions down to 0.5° at 300 GeV. The effective area above 2 TeV is 4×10^8 cm^2. However, the high

altitude allows for significantly more electromagnetic particles in each air shower than at lower altitudes, so at lower energies, the effective area is still quite large, reaching 4×10^6 cm^2 at 100 GeV. The energy resolution is 100% at low energies, improving to 30% above 30 TeV [228–230].

In this work, we use the Coma Berenices dwarf galaxy, the Draco dwarf galaxy, and the Galactic center (GC) to forecast the sensitivity of HAWC to dark matter annihilation signatures. Coma Berenices has a small dark matter annihilation signal but is close to the zenith for the HAWC experiment. In contrast, Draco has a large dark matter annihilation signal but is closer to the horizon for HAWC. With this, we can test whether zenith angle or dark matter annihilation flux is the dominant factor for detection. For the GC, we consider two dark matter profiles, a conservative Einasto profile and a cuspier NFW profile. Throughout this work, we assume no annihilation boost factor from dark matter substructure.

Constraints on the dark matter annihilation rate from dwarf spheroidal galaxies and from the GC are well-established by studies of lower-energy gamma-rays. The Fermi-LAT studied emission from several dwarf galaxies below $E_\gamma = 50$ GeV [209], and the stacked analysis of the Fermi-LAT dwarfs was used to exclude the thermal dark matter cross-section for WIMP masses below 30 GeV for the $b\bar{b}$ and $\tau^+\tau^-$ annihilation channels [44, 45]. Toward the GC, background-removal techniques have been used with Fermi-LAT to also exclude the thermal dark matter cross-section for WIMP masses below 30 GeV for these annihilation channels [69, 231, 232]. Observations of the Sculptor and Carina dwarf spheroidal galaxies with HESS [233], the Segue 1 dwarf galaxy with MAGIC-I [234], and the Draco, Ursa Minor, Boötes 1,

and Segue 1 dwarf galaxies with VERITAS [235, 236] have constrained WIMPs with masses between 1 TeV and 10 TeV to cross-sections below $\langle \sigma_{\rm A} v \rangle \lesssim 1 \times 10^{-22}$ cm^3 s^{-1}. Also, HESS observations from the GC have been used to constrain WIMPs with masses between 1 TeV and 10 TeV to cross-sections below $\langle \sigma_{\rm A} v \rangle \lesssim 5 \times 10^{-25}$ cm^3 s^{-1} [28, 33]. Here, we show that the HAWC observatory is more constraining on high-mass WIMPs than most of these limits.

Below, we show the ability of HAWC to detect annihilating WIMP dark matter from dwarf spheroidal galaxies and the GC. We take the flux profile for annihilating dark matter and run simulations for the HAWC observatory to determine the significance of each signal. Assuming that no such signal is observed, we interpret the lack of a signal as a limit on the dark matter annihilation rate. We consider dark matter annihilations into three channels: a hadronic $t\bar{t}$ channel, a bosonic W^+W^- channel, and a leptonic $\tau^+\tau^-$ channel. The forecasted dark matter limits from HAWC are stronger for high-mass WIMPs than most limits coming from lower-energy observatories.

6.2 Gamma-Ray Emission from Annihilating Dark Matter

6.2.1 Dark Matter Differential Flux

A calculation of the gamma-ray flux from dark matter annihilation requires information about both the astrophysical properties of the dark matter source and the particle properties of the final-state radiation. The differential gamma-ray flux integrated over solid angle $\Delta\Omega$ for a dark matter candidate with cross-section $\langle \sigma_{\rm A} v \rangle$

is

$$\frac{dF}{dE} = \frac{\langle \sigma_{\rm A} v \rangle}{2} \frac{J_{\Delta\Omega}}{J_0} \frac{\Delta\Omega}{4\pi M_\chi^2} \frac{dN_\gamma}{dE} \tag{6.1}$$

where dN_γ/dE is the γ-ray spectrum per annihilation and M_χ is the dark matter particle mass. The integrated mass density squared along line-of-sight x, averaged over the solid angle of the observation region is defined as

$$J_{\Delta\Omega} = \frac{J_0}{\Delta\Omega} \int_{\Delta\Omega} d\,\Omega \int d\,x\ \rho^2(r_{\rm gal}(\theta, x)) \tag{6.2}$$

where distance from the source is given by

$$r_{\rm gal}(\theta, x) = \sqrt{R^2 - 2xR\cos(\theta) + x^2}\ . \tag{6.3}$$

A normalization constant $J_0 \equiv 1/\left[8.5\ {\rm kpc}(0.3\ {\rm GeV\ cm^{-3}})^2\right]$ is chosen to make J dimensionless, but the final flux calculation is independent of the choice of J_0. R is the distance to the source and θ is the angle between the line-of-sight and the source.

For the GC, the dark matter profiles $\rho(r)$ are chosen as the conservative Einasto and NFW models, as was done in Ref. [36]. The conservative Einasto profile is given by

$$\rho_{\rm Einasto}(r) = \rho_s \exp\left[-\frac{2}{0.22}\left(\left(\frac{r}{r_s}\right)^{0.22} - 1\right)\right]\ , \tag{6.4}$$

while the NFW profile is of the form

$$\rho = \frac{\rho_0}{(r/r_s)(1 + r/r_s)^2}\ . \tag{6.5}$$

For the dwarf galaxies Draco and Coma Berenices, the dark matter profiles are done using an NFW profile with parameters given by [209]. The scale radii, scale density,

Parameter	Coma Ber.	Draco	GC NFW	GC Einasto
Declination (J2000)	$+23°54'15''$	$+57°54'55''$	$-29°00'28''$	$-29°00'28''$
Distance R (kpc)	44[a]	76[a]	8.5[b]	8.28[b]
Scale Density ρ_s $\left(\frac{\text{GeV}}{\text{cm}^3}\right)$	9.76[a]	0.976[a]	0.259[b]	0.0715[b]
Scale Radius r_s (kpc)	0.16[a]	2.1[a]	20.0[b]	21.0[b]
$J_{\Delta\Omega}$ $(\Delta\Omega = 10^{-4})$	11.0	42.8	4510	1440

Table 6.1: : Declinations and halo parameters for Coma Berenices, Draco, the GC with an NFW profile, and the GC with an Einasto profile. [a]Coma Berenices and Draco data are chosen as in Ref. [209]. [b]GC data are chosen as in Ref. [36].

and distance to each considered source are shown in Table 6.1. The angular size for a HAWC point-source varies with energy, from $\sim 0.5°$ at 300 GeV to $\sim 0.25°$ above 5 TeV [228, 229], which causes more-peaked dark matter profiles to have an increased J-factor at high energies relative to dark matter profiles which are less-peaked. The energy resolution of HAWC is over 100% at low energies and approaches 30% at high energies, so the energy bins for dF/dE are large. Therefore, the cross-section limits are dominated by the flux in the lowest energy bin, near the HAWC low-energy threshold, 1 TeV.

6.2.2 Calculation of Dark Matter Spectra

To calculate the photon spectrum for a particular WIMP annihilation channel, we use PYTHIA 6.4 to simulate the photon radiation of charged particles as well

as decays of particles such as the π^0 [10], following the method from section 3.2 of Ref. [28]. For each final state and each value of M_χ, we calculate the average number of photons in each energy bin per annihilation event, dN_γ/dE. Specifically, we consider the hadronic $t\bar{t}$, bosonic W^+W^-, and leptonic $\tau^+\tau^-$ annihilations channels.

The HAWC simulation software requires source spectra parameterized as power laws with exponential cutoffs,

$$\frac{dF}{dE} = AE^{-B}\exp(CE) \ . \tag{6.6}$$

For each considered matter source and for each dark matter mass between 1 TeV and 100 TeV, we fit the differential gamma-ray flux from dark matter annihilation above $E = 0.1$ TeV for best-fit parameters A, B, and C. These cutoff-power-law fits differ from the true calculated differential flux by at most a factor of 2, mostly at high energies, and therefore do not significantly affect our results.

6.3 Forecasted Dark Matter Limits from HAWC

Through detailed simulation of the HAWC gamma-ray sensitivity and backgrounds, we have determined the significance of the dark matter flux for several annihilation spectra, a range of dark matter masses, and four different dark matter sources. Assuming that no dark matter signal is observed above background, we convert the source significance into exclusion curves of the dark matter cross section for given dark matter mass. For our exclusion curves, we have assumed a one-year observation time for HAWC and derived the 95% confidence-level (CL) cross-section limits for the $t\bar{t}$, W^+W^-, and $\tau^+\tau^-$ annihilation channels.

In figures 6.1-6.3, the curves are the forecasted 95% CL limits from the Draco dwarf galaxy (dashed light blue curve), the Coma Berenices dwarf galaxy (solid red curve), the GC assuming an Einasto dark matter profile (dot-dashed dark blue curve), and the GC assuming an NFW dark matter profile (dotted purple curve).

Non-relativistic WIMPs, as we consider here, are dominated by s-wave annihilations. For such annihilations, unitarity of the scattering matrix gives an upper bound to the dark matter mass of [237, 238]

$$\sigma_{\rm inel} v_{\rm rel} \leq \frac{4\pi}{M_\chi^2 v_{\rm rel}} = 4.40 \times 10^{-19}\,{\rm cm}^3\,{\rm s}^{-1} \left(\frac{\rm TeV}{M_\chi}\right)^2 \left(\frac{100\,{\rm km\,s}^{-1}}{v_{\rm rel}}\right) \ , \qquad (6.7)$$

in units where $\hbar = c = 1$. The relative velocity between WIMPs in the Galaxy is given by $v_{\rm rel} \sim 300$ kms^{-1}, so for $M_\chi \gtrsim 1000$ TeV the unitarity bound rules out the thermal cross-section of 3×10^{-26} cm^3 s^{-1}. (For further discussion of the unitarity bound, see Appendix C.) The unitarity bound is shown in figures 6.1-6.3 as a black curve, for comparison to our forecasted limits.

6.4 Discussion

The forecasted dark matter limits from HAWC show the relative strengths of the different dark matter sources considered here. The Draco dwarf galaxy has a larger dark matter J-factor than Coma Berenices, by a factor of ~ 4. However, Coma Berenices has a declination closer to the zenith at Sierra Negra than does Draco (see Table 6.1). Figures 6.1-6.3 clearly show that the observational losses due to zenith angle for Draco overwhelm the larger dark matter J-factor, so the limits on Coma Berenices from HAWC are stronger than those for Draco. Therefore, the

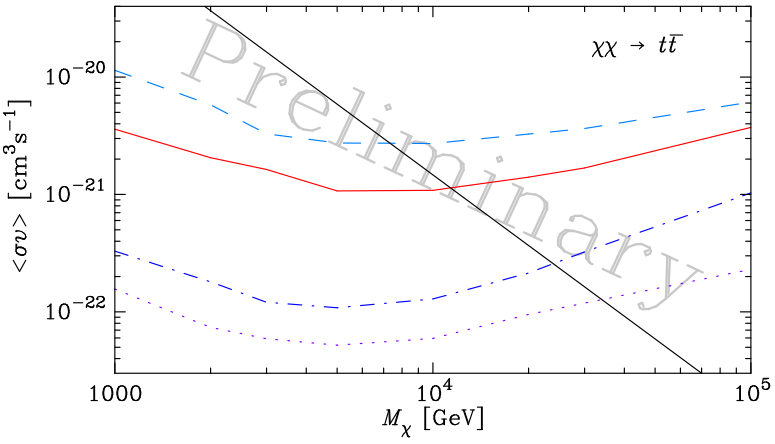

Figure 6.1: The forecasted dark matter limits from HAWC after one year, for the $t\bar{t}$ dark matter annihilation channel. The dashed light blue curve is for the Draco dwarf galaxy. The solid red curve is for the Coma Berenices dwarf galaxy. The dot-dashed dark blue curve is for the GC, assuming an Einasto dark matter profile. The dotted purple curve is for the GC, assuming an NFW dark matter profile. All limits are at 95% CL. The solid black line shows the unitarity limits on the dark matter cross-section for Galactic dark matter.

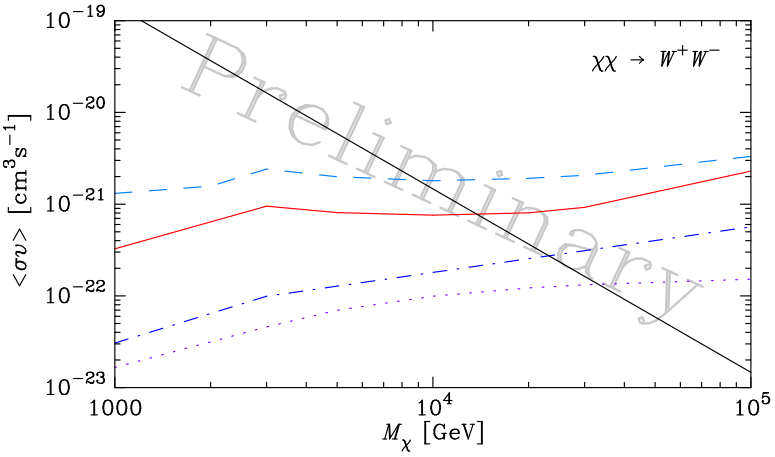

Figure 6.2: The forecasted dark matter limits from HAWC after one year, for the W^+W^- dark matter annihilation channel. The dashed light blue curve is for the Draco dwarf galaxy. The solid red curve is for the Coma Berenices dwarf galaxy. The dot-dashed dark blue curve is for the GC, assuming an Einasto dark matter profile. The dotted purple curve is for the GC, assuming an NFW dark matter profile. All limits are at 95% CL. The solid black line shows the unitarity limits on the dark matter cross-section for Galactic dark matter.

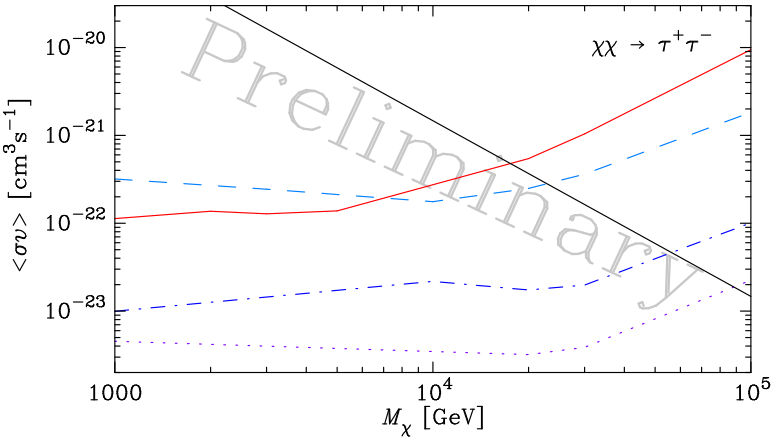

Figure 6.3: The forecasted dark matter limits from HAWC after one year, for the $\tau^+\tau^-$ dark matter annihilation channel. The dashed light blue curve is for the Draco dwarf galaxy. The solid red curve is for the Coma Berenices dwarf galaxy. The dot-dashed dark blue curve is for the GC, assuming an Einasto dark matter profile. The dotted purple curve is for the GC, assuming an NFW dark matter profile. All limits are at 95% CL. The solid black line shows the unitarity limits on the dark matter cross-section for Galactic dark matter.

most favorable targets for HAWC dark matter analyses of dwarf spheroidal galaxies are more strongly dependent on the zenith angle of the sources than on the intrinsic dark matter flux from those sources.

As is shown in figures 6.1-6.3, the GC is an optimal source for HAWC studies of dark matter. Though the GC is over 48° from the zenith, the incredibly large dark matter J-factors from the GC cause its forecasted dark matter annihilation limit to be over an order of magnitude stronger than the Coma Berenices dwarf galaxy. At low energy, where the angular resolution is worse, the NFW profile is twice as constrained as the Einasto profile, while at higher energy, with better angular resolution, the more-peaked NFW profile is more constrained than the less-peaked Einasto profile by a factor of ~ 4.

For the $t\bar{t}$ and W^+W^- annihilation channels (figures 6.1 and 6.2), the forecasted dwarf galaxy limits are stronger than the unitarity bound up to $M_\chi \sim 10$ TeV and the forecasted GC limits are stronger than the unitarity bound up to $M_\chi \sim 30$ TeV. The forecasted $\tau^+\tau^-$ limits (figure 6.3) are an order of magnitude more constraining than for the $t\bar{t}$ and W^+W^- annihilation channels. The forecasted $\tau^+\tau^-$ limits are stronger than the unitarity bound below $M_\chi \sim 20$ TeV for the dwarf galaxies, below $M_\chi \sim 50$ TeV for the Einasto GC model and below ~ 90 TeV for the NFW GC model.

When compared to dark matter analyses at lower energies, the HAWC forecasted dark matter limits are strong. The Fermi-LAT has done a dark matter analysis through stacking of all their observed dwarf spheroidal galaxies, which drops off as M_χ^{-2} for high dark matter masses [44, 45].. Observations of individ-

ual dwarf galaxies by the HESS [233], MAGIC-I [234], and VERITAS [235, 236] collaborations at higher energies have been done as well. The HAWC individual dwarf galaxy forecasts give stronger constraints than the Fermi-LAT, VERITAS, HESS, and MAGIC-I dwarf galaxy analyses above $M_\chi \sim 30$ TeV. Additionally, HAWC's large sky coverage should be able to observe several dwarf galaxies, and a stacked analysis of HAWC dwarf spheroidals will improve the limits considerably. The HAWC GC forecast gives stronger dark matter limits than the Fermi-LAT, VERITAS, HESS, and MAGIC-I dwarf galaxy analyses above $M_\chi \sim 1$ TeV.

It is useful to compare to lower-energy GC analyses as well. Gamma-ray fluxes from the inner $3^\circ \times 3^\circ$ about the GC from the Fermi-LAT have been used to limit dark matter annihilation [69]. These limits are similar in magnitude to the Fermi-LAT stacked dwarf spheroidal analysis discussed above, and the HAWC GC (dwarf spheroidal) forecasted limits are stronger than the Fermi-LAT GC analysis above $M_\chi \sim 1$ TeV ($M_\chi \sim 30$ TeV). Further studies of the Fermi-LAT GC have used background-removal techniques to strengthen the Fermi-LAT limits on the dark matter cross-section [231, 232]. Compared to these background-removed GC Fermi-LAT limits, the HAWC GC (dwarf spheroidal) forecasted limits are stronger above $M_\chi \sim 20$ TeV ($M_\chi \sim 100$ TeV) for the hadronic $t\bar{t}$ and bosonic W^+W^- annihilation channels. However, the leptonic $\tau^+\tau^-$ annihilation channel will be much more strongly constrained by HAWC than by the Fermi-LAT GC analyses. The HAWC GC forecast gives a stronger limit for $M_\chi \gtrsim 2$ TeV and the HAWC dwarf forecast gives a stronger limit for $M_\chi \gtrsim 5$ TeV than the Fermi-LAT GC analyses. A study of the GC with HESS has been shown to have the strongest

constraints on high-mass annihilating dark matter, which is significantly stronger than the forecasted HAWC limits up to 1000 TeV [28, 33].

6.5 Conclusions

The HAWC observatory will give strong bounds to high-mass WIMP dark matter from both the GC and dwarf spheroidal galaxies after one year of observations. For the baryonic $t\bar{t}$ and bosonic W^+W^- dark matter annihilation channels, the Fermi-LAT, HESS, MAGIC, and VERITAS collaborations' dwarf spheroidal limits on the dark matter cross-section [44, 45, 233–236] should be weaker than the HAWC GC limit above $M_\chi \sim 1$ TeV and weaker than the HAWC dwarf spheroidal limit above $M_\chi \sim 30$ TeV. The HAWC GC dark matter cross-section limits should be stronger than the Fermi-LAT GC limits [69, 231, 232] for $M_\chi \gtrsim 20$ TeV in these two dark matter channels. For the leptonic $\tau^+\tau^-$ annihilation channel, both the HAWC GC and dwarfs forecast strong limits, giving a stronger limit than the Fermi-LAT GC analyses and the Fermi-LAT, HESS, MAGIC, and VERITAS collaborations' dwarf spheroidal analyses above $M_\chi \sim 2$ TeV for the HAWC GC forecast and above $M_\chi \sim 5$ TeV for the HAWC dwarf spheroidal forecast. For all dark matter annihilation channels, however, the HESS GC limit [28, 33] provides a stronger limit on the annihilation cross-section than does HAWC.

With the construction of HAWC should come better understanding its gamma/hadron separation and improvements on the energy resolution and angular resolution of the observatory. Better angular resolution would help reject back-

ground photons outside of the region-of-interest, and good energy resolution is necessary to compare the spectral shape of any signal to that expected from the dark matter. Additionally, a greater understanding of backgrounds in the gamma-ray sky should improve HAWC's sensitivity to point-sources, as will improved background-removal techniques. Source stacking should also improve HAWC's ability to detect the dark matter.

Water Čerenkov detectors, like HAWC, are the optimal technology for searching for annihilating high-mass dark matter. Their all-sky field-of-view and near-continuous observation time enable the observation of many dark matter source simultaneously. With the construction of the HAWC observatory, we can probe the dark matter at higher masses than ever before. The prospects for the observation of high-mass dark matter are great.

Chapter 7

Afterward

There is currently a great deal of high-quality astrophysical data coming from a wide variety of experiments. For gamma-ray energies from 100 MeV to 100 GeV, the Fermi-LAT provides a large field-of-view (2.5 sr) with 10% energy resolution and $0.1^\circ - 1^\circ$ angular resolution [239]. At higher energies, from 100 GeV to 10 TeV, the Air Čerenkov detectors HESS, MAGIC, and VERITAS give good sensitivity to gamma-rays with excellent angular resolution [240–242]. The HESS observatory, for example, has a $5^\circ \times 5^\circ$ field-of-view observable with 20% energy resolution and an angular resolution of better than 0.1° [240]. For high gamma-ray energies, above 1 TeV, Water Čerenkov detectors, such as the HAWC observatory, have strong sensitivity to gamma-rays with large field-of-view (1.9 sr), good angular resolution ($0.25^\circ - 0.5^\circ$), and $\sim 50\%$ energy resolution [228–230]. Also sensitive to high-energy astrophysics is the WMAP observatory, which can detect the synchrotron emission from high-energy electrons and positrons emitted in high-energy processes [243].

Chapter 3 discussed the WMAP haze, which was observed in the WMAP foreground emission [89, 125]. Since the writing of that paper, a gamma-ray analogue to the WMAP haze was seen in the inner degrees of the Fermi-LAT data [244]. It was further determined that the gamma-ray signal was elongated away from the GC above and below the Galactic plane, in a geometry known as the "Fermi

bubbles" [245]. In its 7-year polarized data set, however, WMAP saw no evidence for the WMAP haze [243], though it is uncertain whether a polarized emission from synchrotron of hard electrons should be observable above the noise in the signal [246]. In fact, the WMAP haze does appear to be a legitimate signal, as preliminary images from the Planck observatory seem to confirm that a Galactic haze, possibly coincident with the Fermi bubbles, exists in the center of the Galaxy[1].

In chapters 4-5, we considered a blazar model which accounted for the blazar SED and GLF in order to show that blazars unresolved by the Fermi-LAT can produce the entire DGRB, in contradiction to Ref. [131]. Since finishing that work, several other papers have indicated similar results. Ref. [189] finds that blazars could be the source of the DGRB, when accounting for the effects of spectral biasing and uncertainties in the blazar gamma-ray indices, for instance. Additionally, Ref. [193] finds that approximately 59% of the DGRB is due to unresolved blazars, which is much more than the 20% claimed by Ref. [131]. Furthermore, the anisotropy measurements of the DGRB with the Fermi-LAT show an anisotropy consistent with a single population which has gamma-ray indices similar to that of blazars [247]. However, some papers continue to use a model for blazars which does not account for the luminosity-dependence of the blazar index distribution, leading to artificially tight bounds on the blazar contribution to the DGRB (e.g. Ref. [248]). to better understand the intrinsic blazar SED, a recent study by Ref. [191] considers the blazar SED in the radio band. As the amount of data on the blazar SED increases, we should be better able to quantify the contribution of blazars to the DGRB.

[1]http://www.nasa.gov/mission_pages/planck

Upcoming experiments will increase our knowledge of high-energy astrophysical processes greatly. The HAWC collaboration will soon have its first tanks installed and running, and it should be fully functional in 3-4 years, studying the sky at energies of several TeV [249]. For synchrotron emission from high-energy electrons produced in high-energy processes, the Planck observatory [110] will soon be releasing its data from its first years of observations, which should indicate the relationship between the microwave haze and the gamma-ray Fermi bubbles. Additionally, the Čerenkov Telescope Array (CTA) is expected to begin construction in 2013, concluding in 2018 [86]. CTA will provide sky coverage in the northern and southern hemispheres at energies from 20 GeV up to 100 TeV, with sensitivity greater than the Fermi-LAT with an angular resolution better than one arcminute. The next few years will be significant for observations of high-energy astrophysical sources.

Appendix A

Calculation of the WIMP Cross-Section at Freeze-Out

The annihilation cross-section $\langle \sigma v \rangle$ of WIMPs is set by their thermal freezeout in the early universe. Below, I show how a TeV-scale WIMP annihilating with a weak-scale cross-section gives the expected relic density for dark matter, following Ref. [250]. In the early universe, WIMPs (χ) were in thermal equilibrium with other particles (ψ) and interacting with them via $\psi\bar{\psi} \leftrightarrow \chi\bar{\chi}$ annihilations. The phase-space distribution functions f for the ψ particles are given by

$$f_\psi = \exp\left[-\frac{E_\psi}{T}\right], \quad f_{\bar{\psi}} = \exp\left[-\frac{E_{\bar{\psi}}}{T}\right] \quad , \tag{A.1}$$

assuming there is no chemical potential for the WIMPs. Because $E_\chi + E_{\bar{\chi}} = E_\psi + E_{\bar{\psi}}$,

$$f_\psi f_{\bar{\psi}} = \exp\left[-\frac{E_\psi + E_{\bar{\psi}}}{T}\right] = \exp\left[-\frac{E_\chi + E_{\bar{\chi}}}{T}\right] = f_\chi^{eq} f_{\bar{\chi}}^{eq} \quad . \tag{A.2}$$

The Boltzmann equation for the WIMPs then reads

$$\frac{d\, n_\chi}{d\, t} + 3Hn_\chi = -\langle \sigma_{\chi\bar{\chi}\to\psi\bar{\psi}} |v| \rangle \left[f_\chi f_{\bar{\chi}} - f_\psi f_{\bar{\psi}} \right] \tag{A.3}$$

$$= -\langle \sigma_{\chi\bar{\chi}\to\psi\bar{\psi}} |v| \rangle \left[f_\chi f_{\bar{\chi}} - f_\chi^{eq} f_{\bar{\chi}}^{eq} \right] \tag{A.4}$$

$$= -\langle \sigma_{\chi\bar{\chi}\to\psi\bar{\psi}} |v| \rangle \left[n_\chi^2 - (n_\chi^{eq})^2 \right] \quad . \tag{A.5}$$

Summing over all channels, $\sigma_{\chi\bar{\chi}\to\psi\bar{\psi}} \to \sigma_A$. To simplify the Boltzmann equation, we now define

$$Y \equiv \frac{n_\chi}{s} = \frac{n_{\bar{\chi}}}{s} \tag{A.6}$$

$$x \equiv \frac{M}{T} \tag{A.7}$$

$$H_M \equiv x^2 H = 1.67 g_*^{1/2} \frac{M^2}{M_{pl}^2} \tag{A.8}$$

where s is the entropy density, M_{pl} is the Planck mass, and M is the mass of the WIMP. This simplified form of the Boltzmann equation for WIMPs reads

$$\frac{dY}{dx} = -\frac{xs\langle\sigma_A v\rangle}{H_M}\left(Y^2 - Y_{eq}^2\right) \quad . \tag{A.9}$$

When $\Gamma_A \equiv n_{eq}\langle\sigma_A v\rangle \ll H$ we have $dY \ll Y_{eq} d\ln(x)$, so Y changing little with respect to its equilibrium value and is said to have undergone "freeze-out". The value of x where $\Gamma_A \approx H$ is labeled x_f.

The annihilation cross-section for WIMPs should go as $\langle\sigma_A v\rangle \propto v^{2l}$ with $l = 0$ for s-wave annihilation, $l = 1$ for p-wave annihilation, and so on. Because WIMPs freeze out late ($x_f > 3$) they are non-relativistic and therefore s-wave ($l = 0$) annihilation should dominate. Conveniently, this means that $\langle\sigma_A v\rangle$ is a constant, independent of temperature. The Boltzmann equation for s-wave annihilation is

$$\frac{dY}{dx} = -\lambda x^{-2}\left(Y^2 - Y_{eq}^2\right) \tag{A.10}$$

with

$$Y_{eq} = \frac{n_\chi^{eq}}{s} = \left[g \left(\frac{MT}{2\pi} \right)^{3/2} \exp\left(-\frac{M}{T} \right) \right] \left[\frac{45}{2\pi^2 g_{*s} T^3} \right] = 0.145 \frac{g}{g_{*s}} x^{3/2} e^{-x} \quad \text{(A.11)}$$

$$\lambda = \frac{xs\langle\sigma_A v\rangle}{H_M} x^2 = \left[\frac{2\pi^2}{45} g_{*s} T^3 x^3 \langle\sigma_A v\rangle \right] \left[\frac{M_{pl}}{1.67 g_*^{1/2} M^2} \right]$$

$$= 0.264 \frac{g_{*s}}{g_*^{1/2}} M_{pl} M \langle\sigma_A v\rangle \quad \text{(A.12)}$$

where we have used the entropy density

$$s = \frac{2\pi^2}{45} g_{*s} T^3 \ . \quad \text{(A.13)}$$

For $x \gg x_f$, Y is frozen out and remains fairly constant while Y_{eq} dies exponentially, so $Y \gg Y_{eq}$ is a good approximation. We find an approximate solution to Eq. A.10 for large x by integrating from x_f to ∞ to get

$$Y_\infty \approx \frac{x_f}{\lambda} \quad \text{(A.14)}$$

$$x_f \approx \ln\left[0.038 \frac{g}{g_*^{1/2}} M_{pl} M \langle\sigma_A v\rangle \right] - \frac{1}{2} \ln\left\{ \ln\left[0.038 \frac{g}{g_*^{1/2}} M_{pl} M \langle\sigma_A v\rangle \right] \right\} \ . \quad \text{(A.15)}$$

The present number density of WIMPs is

$$n_{\chi 0} = s_0 Y_\infty \approx (2970 \mathrm{cm}^{-3}) \mathrm{Y}_\infty \quad \text{(A.16)}$$

$$\Omega_\chi h^2 = \frac{M n_{\chi 0}}{\rho_c} \quad \text{(A.17)}$$

$$\rho_c = \frac{3H_0^2}{8\pi G} \ . \quad \text{(A.18)}$$

Specifically, we will choose a WIMP with mass M, annihilation cross-section $\langle\sigma_A v\rangle = a \cdot (3 \times 10^{-26}\,\mathrm{cm}^3\,\mathrm{s}^{-1})$, and two degrees of freedom ($g = 2$) that freezes out

at $T \sim 100\,\mathrm{MeV}$ ($g_* = g_{*s} \approx 60$). For these parameters,

$$\begin{aligned} x_f &\approx 19.6 + \ln\left[a\left(\frac{M}{\mathrm{GeV}}\right)\right] - \frac{1}{2}\ln\left\{19.6 + \ln\left[a\left(\frac{M}{\mathrm{GeV}}\right)\right]\right\} \\ &\approx 18 + \ln\left[a\left(\frac{M}{\mathrm{GeV}}\right)\right] \end{aligned} \tag{A.19}$$

$$\begin{aligned} Y_\infty &\approx \frac{1.56 \times 10^{-11}}{a\,(M/\mathrm{GeV})}\left(18 + \ln\left[a\left(\frac{M}{\mathrm{GeV}}\right)\right]\right) \\ &\approx \frac{2.81 \times 10^{-10}}{a\,(M/\mathrm{GeV})}\left(1 + 0.0556\ln\left[a\left(\frac{M}{\mathrm{GeV}}\right)\right]\right) \end{aligned} \tag{A.20}$$

$$\Omega_\chi h^2 \approx 4.41 \times 10^{-3}\,\frac{x_f}{a} \approx \frac{0.0794}{a}\left(1 + 0.0556\ln\left[a\left(\frac{M}{\mathrm{GeV}}\right)\right]\right) \quad . \tag{A.21}$$

The current best-fit value for the dark matter fraction is $\Omega_{CDM}h^2 = 0.1122$ from the WMAP collaboration [2]. Neglecting the logarithmic term, this gives $\langle\sigma_A v\rangle \approx 2.1 \times 10^{-26}\,\mathrm{cm^3\,s^{-1}}$, which is close to the canonical value of $3 \times 10^{-26}\,\mathrm{cm^3\,s^{-1}}$, corresponding to a weak-scale WIMP annihilation cross-section $\sigma_A \approx 1$ pb. Including the logarithmic term, the cross-section is dependent on the WIMP mass, though only by ~ 50 percent over four orders of magnitude in M. The cross-section for a range of masses is given in Table A.1. The solution, labeled $\langle\sigma_A v\rangle$, varies by only ~ 50 percent over four orders of magnitude in M, so the standard assumption that $\langle\sigma_A v\rangle = 3 \times 10^{-26}\,\mathrm{cm^3\,s^{-1}}$ regardless of mass is very well-motivated.

Table 1

Mass-Dependence of WIMP Cross-Sections	
M[GeV]	$\langle \sigma_A v \rangle$
1	2.08×10^{-26}
3	2.22×10^{-26}
10	2.37×10^{-26}
30	2.50×10^{-26}
100	2.65×10^{-26}
300	2.79×10^{-26}
1000	2.93×10^{-26}
3000	3.07×10^{-26}
1×10^4	3.22×10^{-26}
3×10^4	3.35×10^{-26}
1×10^5	3.50×10^{-26}

Table A.1: WIMP annihilation cross-section vs WIMP mass, for a standard thermal WIMP. The cross-sections have been calculated to leading logarithmic order.

Appendix B

Blazar Model

B.1 Blazar SED Sequence

The full SED fit is given as a function of radio luminosity ψ_R and the logarithm of rest-frame frequency x. We follow Ref. [251] in the formulation of the SED. The radio luminosity is used to distinguish between SEDs for blazars of different bolometric luminosity. This separation of SED by total luminosity should account for the difference in spectral index seen by the Fermi-LAT between higher-luminosity FSRQs and lower-luminosity BL Lacs [163, 172, 173].

$$x \equiv \log_{10}(\nu/\mathrm{Hz}), \tag{B.1}$$

$$\psi(x;\psi_R) \equiv \log_{10}[\frac{\nu L_\nu(\nu(x), P(\psi_R))}{\mathrm{erg\ s^{-1}}}], \tag{B.2}$$

$$\psi_R \equiv \psi(x = 9.698). \tag{B.3}$$

The full model is the sum of a synchrotron $[\psi_s(x)]$ and inverse Compton $[\psi_c(x)]$ component.

$$\psi(x) = \log_{10}[10^{\psi_s(x)} + 10^{\psi_c(x)}]. \tag{B.4}$$

Each component is parameterized as the sum of a lower-frequency linear part and a higher-frequency parabolic part. Here, $x_{tr,s}$ and $x_{tr,c}$ are the frequencies where the linear part transitions to the parabolic part for the synchrotron and IC

component. The linear parts are written as

$$\psi_{s1}(x) \equiv (1-\alpha_s)(x-x_R)+\psi_R \ (x<x_{tr,s}), \tag{B.5}$$

$$\psi_{c1}(x) \equiv (1-\alpha_c)(x-x_X)+\psi_X \ (x<x_{tr,c}), \tag{B.6}$$

where $\alpha_s = 0.2$ and $\alpha_c = 0.6$ are the $L_\nu \propto \nu^\alpha$ indices in the radio and hard x-ray bands, respectively. The characteristic radio and hard x-ray frequencies are $x_R = 9.698$ and $x_X = 17.383$. The radio luminosity ψ_R is an input parameter to the theory and the hard x-ray luminosity is fitted to the data as

$$\psi_X = \begin{cases} (\psi_R - 43) + 43.17 & \psi_R \leq 43 \\ 1.40(\psi_R - 43) + 43.17 & 43 < \psi_R \leq 46.68 \\ 1.40(46.68 - 43) + 43.17 & \psi_R > 46.68 \ . \end{cases} \tag{B.7}$$

The parameter ψ_X is kept constant for $\psi_R > 46.68$ because the continuity of the IC component cannot be satisfied above this value. However, this hard x-ray luminosity corresponds to a gamma-ray luminosity well above the maximum detected gamma-ray luminosity, so it does not affect the calculation of the DGRB.

The parabolic parts of the components are parameterized as

$$\psi_{s2}(x) \equiv \psi_{s,p} - [(x-x_s)/\sigma]^2 \ (x \geq x_{tr,s}), \tag{B.8}$$

$$\psi_{c2}(x) \equiv \psi_{c,p} - [(x-x_c)/\sigma]^2 \ (x \geq x_{tr,c}), \tag{B.9}$$

where x_s and x_c are the synchrotron and IC peak frequencies, $\psi_{s,p}$ and $\psi_{c,p}$ are the synchrotron and IC peak luminosities, and σ is the width of the parabolas.

By requiring continuity of the synchrotron component from the linear-to-

parabolic parts, we have

$$\psi_{s,p} = (1-\alpha_s)(x_{tr,s} - x_R) + \psi_R + \left(\frac{x_{tr,s} - x_s}{\sigma}\right)^2 \ . \tag{B.10}$$

Similarly, the continuity of the IC component gives

$$x_{tr,c} = \frac{-\zeta - \sqrt{\zeta^2 - 4\eta}}{2}, \tag{B.11}$$

$$\zeta = \sigma^2(1-\alpha_c) - 2x_c, \tag{B.12}$$

$$\eta = x_c^2 + \sigma^2[\psi_X - x_X(1-\alpha_c) - \psi_{c,p}] \ . \tag{B.13}$$

By inspection

$$x_{tr,s} = 10.699, \tag{B.14}$$

$$x_c = x_s + 8.699 \ . \tag{B.15}$$

Fitting to data, the rest of the parameters are given by

$$x_s = \begin{cases} -0.88(\psi_R - 43) + 14.47 & \psi_R \leq 43 \\ -0.40(\psi_R - 43) + 14.47 & \psi_R > 43 \end{cases} \tag{B.16}$$

$$\sigma = \begin{cases} 0.0891 x_s + 1.78 & \psi_R \leq 43 \\ [2(x_s - x_{tr,s})/(1-\alpha_s)]^{1/2} & \psi_R > 43 \end{cases} \tag{B.17}$$

$$\psi_{c,p} = \begin{cases} \psi_{s,p} & \psi_R \leq 43 \\ 1.77(\psi_R - 43)^{0.718} + 45.3 & \psi_R > 43 \ . \end{cases} \tag{B.18}$$

These parameters have been chosen such that the luminosity changes continuously with ψ_R over all luminosities and to make the synchrotron linear-to-parabolic transition smooth for large ψ_R.

B.2 X-ray Luminosity Function

The x-ray luminosity function ρ_X is the comoving number density of AGN per unit x-ray AGN disk luminosity L_X. The model of Refs. [165, 174] give the distribution as

$$\rho_X(L_X, z) = \rho_X(L_X, 0) f(L_X, z). \tag{B.19}$$

The present distribution is given by

$$\rho_X(L_X, 0) = \frac{A_X}{L_X ln(10)} \left[\left(\frac{L_X}{L_X^*} \right)^{\gamma_1} + \left(\frac{L_X}{L_X^*} \right)^{\gamma_2} \right]^{-1}. \tag{B.20}$$

The density evolution is given by

$$f(L_X, z) = \begin{cases} (1+z)^{p_1} & z \leq z_c(L_X) \\ (1+z_c(L_X))^{p_1} \left(\frac{1+z}{1+z_c(L_X)} \right)^{p_2} & z > z_c(L_X). \end{cases} \tag{B.21}$$

The peak evolution happens at z_c, given by

$$z_c(L_X) = \begin{cases} z_c^* & L_X \geq L_a \\ z_c^* (L_X/L_a)^{\alpha} & L_X < L_a. \end{cases} \tag{B.22}$$

The evolution indices p_1 and p_2 are

$$p_1 = p_1^* + \beta_1 [\log_{10}(L_X) - 44.0] \tag{B.23}$$

$$p_2 = p_2^* + \beta_2 [\log_{10}(L_X) - 44.0]. \tag{B.24}$$

The parameters for the models are given in Table B.1. If $\gamma_1 > 1$, then the integrated background flux diverges, so we set the minimum gamma-ray luminosity to $L_{\gamma,\min} = 10^{42}$ erg/s. This is an order-of-magnitude lower than any Fermi-LAT observed blazar, and the results are not sensitive to this value being lowered slightly [163, 172].

Parameter	Ueda et al. 2003	Hasinger et al. 2005
A_X (Mpc^{-3})	5.04×10^{-6}	2.62×10^{-7}
$log_{10}L_X^*$	$43.94^{+0.21}_{-0.26}$	43.94 ± 0.11
γ_2	2.23 ± 0.13	2.57 ± 0.16
z_c^*	1.9, fixed	1.96 ± 0.15
$log_{10}L_a$	44.6, fixed	44.67, fixed
α	0.335 ± 0.07	0.21 ± 0.04
p_1^*	4.23 ± 0.39	4.7 ± 0.3
p_2^*	-1.5, fixed	-1.5 ± 0.7
β_1	0.0, fixed	0.7 ± 0.3
β_2	0.0, fixed	0.6 ± 0.8

Table B.1: Parameters for the AGN XLF from Refs. [165, 174]. Note: Luminosities are in erg/s.

Appendix C

Unitarity Bounds on the WIMP Cross-Section

For multi-TeV WIMPs, the unitarity of the scattering matrix (S) provides an upper limit on the dark matter annihilation cross-section, which I show here following Refs. [237, 238]. Unitarity of S provides that $S^\dagger S = 1$. Therefore,

$$(1-S)(1-S)^\dagger = (1-S^\dagger) + (1-S) \ . \tag{C.1}$$

For the scattering from one state $|i\rangle$ to an identical state $|i\rangle$, then unitarity gives

$$2\,\mathrm{Re}[\langle i|(1-S)|i\rangle] = \langle i|(1-S) + (1-S^\dagger)|i\rangle \tag{C.2}$$

$$= \langle i|(1-S)(1-S)^\dagger|i\rangle \tag{C.3}$$

$$= \int d\,\gamma \langle i|(1-S)|\gamma\rangle\langle\gamma|(1-S)^\dagger|i\rangle \tag{C.4}$$

where $d\,\gamma$ covers the complete set of states γ. By definition, the scattering amplitude $A_{\beta\alpha}$ is

$$\langle\beta|(1-S)|\alpha\rangle \equiv -i(2\pi)^4\delta^4\left(\sum p_\beta - \sum p_\alpha\right) A_{\beta\alpha} \ . \tag{C.5}$$

Inserting Eq. C.5 into Eq. C.4 gives

$$2\,\mathrm{Re}[-i(2\pi)^4\delta^4(p_i-p_i)A_{ii}] = \int d\,\gamma \left\{-i(2\pi)^4\delta^4(p_i-p_\gamma)A_{i\gamma}\right\} \times$$

$$\times \left\{i(2\pi)^4\delta^4(p_i-p_\gamma)A^*_{\gamma i}\right\} \tag{C.6}$$

$$2\,\mathrm{Im}[(2\pi)^4\delta^4(0)A_{ii}] = \int d\,\gamma (2\pi)^8\delta^4(0)\delta^4(p_i-p_\gamma)|A_{\gamma i}|^2 \tag{C.7}$$

$$2\,\mathrm{Im}[A_{ii}] = \int d\,\gamma (2\pi)^4\delta^4(p_i-p_\gamma)|A_{\gamma i}|^2 \ . \tag{C.8}$$

For any two particles scattering in the center-of-mass frame, the differential cross-section is [252]

$$d\,\sigma(i \to \gamma) = \frac{(2\pi)^4 |A_{\gamma i}|^2}{4(E_1 + E_2)|\vec{p}_1|} \delta^4 \left(\sum p_i - \sum p_\gamma \right) d\,\gamma \ , \tag{C.9}$$

where the center-of-mass energies of the initial two particles are E_1 and E_2, the center-of-mass momentum of one of the initial particles is $\vec{p}_1$, and all final states' phase-space are covered by

$$d\,\gamma = \frac{d^3 p_1'}{(2\pi)^3 2E_1'} \frac{d^3 p_2'}{(2\pi)^3 2E_2'} \cdots \ . \tag{C.10}$$

Inserting Eq. C.8 into Eq. C.9, we get the optical theorem

$$\sigma_{tot} = \int d\,\gamma \frac{d\,\sigma}{d\,\gamma}(i \to \gamma) = \frac{\mathrm{Im}[A_{ii}]}{2(E_1 + E_2)|\vec{p}_1|} \ . \tag{C.11}$$

Our next goal is to calculate the total cross-section and inelastic cross-sections for 2-to-2 particle scattering, in the center-of-mass frame. Let $|i\rangle = |p_1, p_2, s_{1z}, s_{2z}\rangle$ and $|\gamma\rangle = |p_1', p_2', s_{1z}', s_{2z}'\rangle$ be the initial and final states, with 4-momenta and spins, in 2-to-2 particle scattering, respectively. Starting with Eq. C.5, we sum over final particle momenta and insert a set of complete angular momentum states around the scattering matrix. The sum over final particle momenta yields the expression

$$\begin{aligned}
(2\pi)^4 \delta^4(p_1' + p_2' - p_1 - p_2) \frac{d^3 p_1'}{(2\pi)^3 2E_1'} \frac{d^3 p_2'}{(2\pi)^3 2E_2'} & \\
&= \frac{\delta(E_1' + E_2' - E_1 - E_2)}{E_1' E_2'} \frac{|\vec{p}_1|^2 d\,|\vec{p}_1| d\,\Omega}{4(2\pi)^2} \\
&= \frac{1}{4(2\pi)^2} \frac{|\vec{p}_1| d\,\Omega}{E_1' + E_2'} \delta(W - E_1' - E_2') dW \\
&= \frac{1}{4(2\pi)^2} \frac{|\vec{p}_1| d\,\Omega}{E_1 + E_2}
\end{aligned} \tag{C.12}$$

where

$$W = E_1 + E_2 = E_1' + E_2' = \sqrt{M_1'^2 + |\vec{p}_1'|^2} + \sqrt{M_2'^2 + |-\vec{p}_1'|^2} \tag{C.13}$$

$$dW = d\,|\vec{p}_1'|\left(\frac{|\vec{p}_1'|}{E_1'} + \frac{|\vec{p}_1'|}{E_2'}\right) = d\,|\vec{p}_1'||\vec{p}_1'|\frac{E_1' + E_2'}{E_1' E_2'} \ . \tag{C.14}$$

Around the scattering matrix, we also insert the complete set of angular momentum states

$$\sum_{j,j_z}|j\ j_z\rangle\langle j\ j_z|\sum_{l,l_z}|l\ l_z\rangle\langle l\ l_z|\sum_{s,s_z}|s\ s_z\rangle\langle s\ s_z|\sum_{l',l_z'}|l'\ l_z'\rangle\langle l'\ l_z'|\sum_{s',s_z'}|s'\ s_z'\rangle\langle s'\ s_z'| \tag{C.15}$$

to get the complete scattering amplitude

$$A_{\gamma i} = 4i(2\pi)^2\frac{E_1 + E_2}{|\vec{p}_1|}\sum_{j,j_z}\sum_{l,l',s,s'}\langle l'\ s'|(1-S)|l\ s\rangle\times \tag{C.16}$$

$$\times\sum_{s_z,s_z'}\langle s'\ s_z'|s_{z1}'\ s_{z2}'\rangle\langle s\ s_z|s_{z1}\ s_{z2}\rangle^*\times \tag{C.17}$$

$$\times\sum_{l_z,l_z'}\langle j\ j_z|l_z'\ s_z'\rangle\langle j\ j_z|l_z\ s_z\rangle^*\langle\hat{p}_1'|l'\ l_z'\rangle\langle\hat{p}_1|l\ l_z\rangle^* \ .$$

If we let $\hat{p}_1 = \hat{z}$, average over initial spins, and set $|\gamma\rangle = |i\rangle$, then

$$A_{ii} = \frac{4\pi i}{(2s_1+1)(2s_2+1)}\frac{E_1 + E_2}{|\vec{p}_1|}\sum_j(2j+1)\sum_{l,s}\langle l\ s|(1-S)|l\ s\rangle \ . \tag{C.18}$$

Finally, inserting Eq. C.18 into the optical theorem, Eq. C.11, we get the total 2-body cross-section

$$\sigma_{\rm tot} = \frac{2\pi}{(2s_1+1)(2s_2+1)|\vec{p}_1|^2}\sum_j(2j+1)\sum_{l,s}\mathrm{Re}[\langle l\ s|(1-S)|l\ s\rangle] \ . \tag{C.19}$$

The elastic cross-section is the cross-section for $\chi\chi \to \chi\chi$ or $\chi\bar{\chi} \to \chi\bar{\chi}$. The cross-section for this interaction is given by [252]

$$d\,\sigma_{\rm el} = \frac{|A_{fi}|^2}{4(E_1+E_2)|\vec{p}_1|}(2\pi)^4\delta^4\left(\sum p_f - \sum p_i\right)\frac{d^3p_1'}{(2\pi)^3 2E_1'}\frac{d^3p_2'}{(2\pi)^3 2E_2'} \ . \tag{C.20}$$

From Eq. C.16, averaging over initial spins, and letting $\hat{p}_1 = \hat{z}$, we find that

$$|A_{fi}|^2 = \frac{64\pi^3}{(2s_1+1)(2s_2+1)} \frac{(E_1+E_2)^2}{|\vec{p}_1|^2} \sum_{j,j_z} \sum_{l,l',s,s'} |\langle l'\, s'|(1-S)|l\, s\rangle|^2 \tag{C.21}$$

where we have used $\int d\,\Omega' |Y_{l'\,l'_z}|^2 = \delta_{l'\,l'} \delta_{l'_z\,l'_z} = 1$ for the outgoing particle directions Ω'. From Eqs. C.12, C.20, and C.21, the total elastic cross-section is

$$\sigma_{\rm el} = \frac{1}{(2s_1+1)(2s_2+1)} \frac{\pi}{|\vec{p}_1|} \sum_j (2j+1) \sum_{l,l',s,s'} |\langle l'\, s'|(1-S)|l\, s\rangle|^2 \ . \tag{C.22}$$

The inelastic cross-section ($\chi\chi \nrightarrow \chi\chi$ or $\chi\bar{\chi} \nrightarrow \chi\bar{\chi}$) is given by $\sigma_{\rm tot} - \sigma_{\rm el}$

$$\begin{aligned}
\sigma_{\rm inel} =& \frac{\pi}{(2s_1+1)(2s_2+1)|\vec{p}_1|^2} \sum_j (2j+1) \\
& \times \left\{ \sum_{l,s} 2{\rm Re}[\langle {\rm l\,s}|(1-{\rm S})|{\rm l\,s}\rangle] - \sum_{\rm l,l',s,s'} |\langle {\rm l'\,s'}|(1-{\rm S})|{\rm l\,s}\rangle|^2 \right\} \qquad \text{(C.23)} \\
=& \frac{\pi}{(2s_1+1)(2s_2+1)|\vec{p}_1|^2} \sum_j (2j+1) \\
& \times \sum_{l,s} \left\{ 1 - |\langle l\, s|S|l\, s\rangle|^2 - \sum_{l\neq l', s\neq s'} |\langle l'\, s'|(1-S)|l\, s\rangle|^2 \right\} \qquad \text{(C.24)}
\end{aligned}$$

where we have used

$$\begin{aligned}
|\langle l\, s|(1-S)|l\, s\rangle|^2 &= (\langle l\, s|(1-S)|l\, s\rangle)^* \langle l\, s|(1-S)|l\, s\rangle \\
&= 1 - 2{\rm Re}[\langle {\rm l\,s}|{\rm S}|{\rm l\,s}\rangle] + |\langle {\rm l\,s}|{\rm S}|{\rm l\,s}\rangle|^2 \ . \qquad \text{(C.25)}
\end{aligned}$$

To place constraints on the cross-sections, we will place limits on the S-matrix elements in Eqs. C.19 and C.24. Trivially,

$${\rm Re}[\langle\alpha|(1-{\rm S})|\alpha\rangle] = 1 - {\rm Re}[\langle\alpha|{\rm S}|\alpha\rangle] \leq 1 + |{\rm Re}[\langle\alpha|{\rm S}|\alpha\rangle]| \leq 1 + |\langle\alpha|{\rm S}|\alpha\rangle| \ . \tag{C.26}$$

Furthermore,

$$|\langle\alpha|S|\alpha\rangle|^2 = \langle\alpha|S^\dagger|\alpha\rangle\langle\alpha|S|\alpha\rangle \leq \int d\,\gamma \langle\alpha|S^\dagger|\gamma\rangle\langle\gamma|S|\alpha\rangle = \langle\alpha|S^\dagger S|\alpha\rangle = 1 \tag{C.27}$$

because $|\alpha\rangle$ is one of the states summed over in $|\gamma\rangle$. Therefore, we can place an upper limit on the total cross-section through:

$$\mathrm{Re}[\langle\alpha|(1-\mathrm{S})|\alpha\rangle] \leq 2 \tag{C.28}$$

$$\sigma_{\mathrm{tot}} \leq \frac{4\pi}{(2s_1+1)(2s_2+1)|\vec{p}_1|^2}\sum_{j,l,s}(2j+1)\ . \tag{C.29}$$

An upper bound on the inelastic cross-section can be found as well, using

$$|\langle l\ s|S|l\ s\rangle|^2 \geq 0 \tag{C.30}$$

$$|\langle l'\ s'|(1-S)|l\ s\rangle|^2 \geq 0 \tag{C.31}$$

$$1-|\langle l\ s|S|l\ s\rangle|^2-|\langle l'\ s'|(1-S)|l\ s\rangle|^2 \leq 1 \tag{C.32}$$

$$\sigma_{\mathrm{inel}} \leq \frac{\pi}{(2s_1+1)(2s_2+1)|\vec{p}_1|^2}\sum_{j,l,s}(2j+1)\ . \tag{C.33}$$

For thermalized WIMPs annihilating non-relativistically with relative velocity v_{rel} the momentum is related to the relative velocity and the WIMP mass by

$$|\vec{p}_1|^2 = E_1^2 - M_\chi^2 = M_\chi^2\frac{v_1^2}{1-v_1^2} = \frac{M_\chi^2}{4}\frac{v_{\mathrm{rel}}^2}{1-v_{\mathrm{rel}}^2/4} \approx M_\chi^2\frac{v_{\mathrm{rel}}^2}{4} \tag{C.34}$$

because $\vec{v}_{\mathrm{rel}} = \vec{v}_1 - \vec{v}_2 = 2\vec{v}_1$. Therefore, for WIMPs with relative velocity v_{rel} and mass M_χ the cross-section is limited by

$$\sigma_{\mathrm{tot}} \leq \frac{16\pi}{(M_\chi v_{\mathrm{rel}})^2} = 1.76\times10^{-25}\,\mathrm{cm}^2\left(\frac{\mathrm{TeV}}{M_\chi}\right)^2\left(\frac{100\,\mathrm{km\,s^{-1}}}{v_{\mathrm{rel}}}\right)^2 \tag{C.35}$$

$$\sigma_{\mathrm{inel}}v_{\mathrm{rel}} \leq \frac{4\pi}{M_\chi^2 v_{\mathrm{rel}}} = 4.40\times10^{-19}\,\mathrm{cm}^3\,\mathrm{s}^{-1}\left(\frac{\mathrm{TeV}}{M_\chi}\right)^2\left(\frac{100\,\mathrm{km\,s^{-1}}}{v_{\mathrm{rel}}}\right) \tag{C.36}$$

for an s-wave annihilation (as is expected for non-relativistic WIMP annihilations), with $v_{\mathrm{rel}} \sim 300\,\mathrm{km\,s^{-1}}$ in the Milky Way, $v_{\mathrm{rel}} \sim 1000\,\mathrm{km\,s^{-1}}$ in clusters, and $v_{\mathrm{rel}} \sim 1.50\times10^5\,\mathrm{km\,s^{-1}}$ at freeze-out, assuming those WIMPs are thermalized [237, 238].

Bibliography

[1] F. Zwicky, *Spectral displacement of extra galactic nebulae*, *Helv.Phys.Acta* **6** (1933) 110–127.

[2] **WMAP Collaboration** Collaboration, E. Komatsu *et. al.*, *Seven-Year Wilkinson Microwave Anisotropy Probe (WMAP) Observations: Cosmological Interpretation*, *Astrophys.J.Suppl.* **192** (2011) 18, [arXiv:1001.4538].

[3] D. Larson, J. Dunkley, G. Hinshaw, E. Komatsu, M. Nolta, *et. al.*, *Seven-Year Wilkinson Microwave Anisotropy Probe (WMAP) Observations: Power Spectra and WMAP-Derived Parameters*, *Astrophys.J.Suppl.* **192** (2011) 16, [arXiv:1001.4635].

[4] B. A. Reid, W. J. Percival, D. J. Eisenstein, L. Verde, D. N. Spergel, *et. al.*, *Cosmological Constraints from the Clustering of the Sloan Digital Sky Survey DR7 Luminous Red Galaxies*, *Mon.Not.Roy.Astron.Soc.* **404** (2010) 60–85, [arXiv:0907.1659].

[5] O. Y. Gnedin and J. P. Ostriker, *Limits on collisional dark matter from elliptical galaxies in clusters*, *Astrophys.J.* (2000) [astro-ph/0010436].

[6] S. W. Randall, M. Markevitch, D. Clowe, A. H. Gonzalez, and M. Bradac, *Constraints on the Self-Interaction Cross-Section of Dark Matter from Numerical Simulations of the Merging Galaxy Cluster 1E 0657-56*, *Astrophys.J.* **679** (2008) 1173–1180, [arXiv:0704.0261].

[7] **MACHO** Collaboration, C. Alcock *et. al.*, *The MACHO project: limits on planetary mass dark matter in the galactic halo from gravitational microlensing*, *Astrophys.J.* **471** (1996) 774, [astro-ph/9604176].

[8] **MACHO** Collaboration, C. Alcock *et. al.*, *The MACHO project: Microlensing results from 5.7 years of LMC observations*, *Astrophys.J.* **542** (2000) 281–307, [astro-ph/0001272].

[9] L. Wyrzykowski, S. Kozlowski, J. Skowron, A. Udalski, M. Szymanski, *et. al.*, *The OGLE View of Microlensing towards the Magellanic Clouds. III. Ruling out sub-solar MACHOs with the OGLE-III LMC data*, arXiv:1012.1154.

[10] T. Sjostrand, S. Mrenna, and P. Z. Skands, *PYTHIA 6.4 Physics and Manual*, *JHEP* **0605** (2006) 026, [hep-ph/0603175].

[11] G. R. Blumenthal, S. Faber, R. Flores, and J. R. Primack, *Contraction of Dark Matter Galactic Halos Due to Baryonic Infall*, *Astrophys.J.* **301** (1986) 27.

[12] J. Diemand *et. al.*, *Clumps and streams in the local dark matter distribution*, *Nature* **454** (2008) 735–738, [arXiv:0805.1244].

[13] O. Y. Gnedin, A. V. Kravtsov, A. A. Klypin, and D. Nagai, *Response of dark matter halos to condensation of baryons: cosmological simulations and improved adiabatic contraction model*, *Astrophys. J.* **616** (2004) 16–26, [astro-ph/0406247].

[14] O. Y. Gnedin *et. al.*, *Halo Contraction Effect in Hydrodynamic Simulations of Galaxy Formation*, arXiv:1108.5736.

[15] J. Guedes, S. Callegari, P. Madau, and L. Mayer, *Forming Realistic Late-Type Spirals in a LCDM Universe: The Eris Simulation*, *Astrophys. J.* **742** (2011) 76, [arXiv:1103.6030].

[16] A. V. Maccio' *et. al.*, *Halo expansion in cosmological hydro simulations: towards a baryonic solution of the cusp/core problem in massive spirals*, arXiv:1111.5620.

[17] J. F. Navarro, C. S. Frenk, and S. D. M. White, *A Universal Density Profile from Hierarchical Clustering*, *Astrophys. J.* **490** (1997) 493–508, [astro-ph/9611107].

[18] J. F. Navarro *et. al.*, *The Diversity and Similarity of Cold Dark Matter Halos*, arXiv:0810.1522.

[19] S. Pedrosa, P. B. Tissera, and C. Scannapieco, *The joint evolution of baryons and dark matter haloes*, *Mon. Not. Roy. Astron. Soc.* **402** (Feb., 2010) 776–788, [arXiv:0910.4380].

[20] E. Romano-Diaz, I. Shlosman, Y. Hoffman, and C. Heller, *Erasing Dark Matter Cusps in Cosmological Galactic Halos with Baryons*, arXiv:0808.0195.

[21] E. Romano-Diaz, I. Shlosman, C. Heller, and Y. Hoffman, *Dissecting Galaxy Formation: I. Comparison Between Pure Dark Matter and Baryonic Models*, *Astrophys. J.* **702** (2009) 1250–1267, [arXiv:0901.1317].

[22] J. Stadel, D. Potter, B. Moore, J. Diemand, P. Madau, M. Zemp, M. Kuhlen, and V. Quilis, *Quantifying the heart of darkness with GHALO - a multibillion particle simulation of a galactic halo*, *Mon. Not. Roy. Astron. Soc.* **398** (Sept., 2009) L21–L25, [arXiv:0808.2981].

[23] P. B. Tissera, S. D. M. White, S. Pedrosa, and C. Scannapieco, *Dark matter response to galaxy formation*, arXiv:0911.2316.

[24] J. Einasto, *Kinematics and dynamics of stellar systems*, *Trudy Inst. Astrofiz. Alma-Ata* **51** (1965) 87.

[25] V. Springel, J. Wang, M. Vogelsberger, A. Ludlow, A. Jenkins, *et. al.*, *The Aquarius Project: the subhalos of galactic halos*, *Mon.Not.Roy.Astron.Soc.* **391** (2008) 1685–1711, [arXiv:0809.0898].

[26] R. Catena and P. Ullio, *A novel determination of the local dark matter density*, *JCAP* **1008** (2010) 004, [arXiv:0907.0018].

[27] **Particle Data Group** Collaboration, K. Nakamura *et. al.*, *Review of particle physics*, *J.Phys.G* **G37** (2010) 075021.

[28] K. N. Abazajian and J. Harding, *Constraints on WIMP and Sommerfeld-Enhanced Dark Matter Annihilation from HESS Observations of the Galactic Center*, *JCAP* **1201** (2012) 041, [arXiv:1110.6151].

[29] J. Harding and K. N. Abazajian, *Morphological Tests of the Pulsar and Dark Matter Interpretations of the WMAP Haze*, *Phys.Rev.* **D81** (2010) 023505, [arXiv:0910.4590].

[30] K. N. Abazajian, S. Blanchet, and J. Harding, *The Contribution of Blazars to the Extragalactic Diffuse Gamma-ray Background and Their Future Spatial Resolution*, *Phys.Rev.* **D84** (2011) 103007, [arXiv:1012.1247].

[31] K. N. Abazajian, S. Blanchet, and J. Harding, *Current and Future Constraints on Dark Matter from Prompt and Inverse-Compton Photon Emission in the Isotropic Diffuse Gamma-ray Background*, *Phys.Rev.* **D85** (2012) 043509, [arXiv:1011.5090].

[32] J. L. Feng, *Dark Matter Candidates from Particle Physics and Methods of Detection*, *Ann.Rev.Astron.Astrophys.* **48** (2010) 495, [arXiv:1003.0904].

[33] **HESS** Collaboration, A. Abramowski *et. al.*, *Search for a Dark Matter annihilation signal from the Galactic Center halo with H.E.S.S*, *Phys.Rev.Lett.* **106** (2011) 161301, [arXiv:1103.3266].

[34] **The HESS** Collaboration, J. Hinton, *The Status of the H.E.S.S. project*, *New Astron.Rev.* **48** (2004) 331–337, [astro-ph/0403052].

[35] **The HESS** Collaboration, F. Aharonian *et. al.*, *Discovery of very-high-energy gamma-rays from the galactic centre ridge*, *Nature* **439** (2006) 695–698, [astro-ph/0603021].

[36] K. N. Abazajian, P. Agrawal, Z. Chacko, and C. Kilic, *Conservative Constraints on Dark Matter from the Fermi-LAT Isotropic Diffuse Gamma-Ray Background Spectrum*, *JCAP* **1011** (2010) 041, [arXiv:1002.3820].

[37] N. F. Bell and T. D. Jacques, *Gamma-ray Constraints on Dark Matter Annihilation into Charged Particles*, *Phys.Rev.* **D79** (2009) 043507, [arXiv:0811.0821].

[38] G. Bertone, M. Cirelli, A. Strumia, and M. Taoso, *Gamma-ray and radio tests of the e+e- excess from DM annihilations*, *JCAP* **0903** (2009) 009, [arXiv:0811.3744].

[39] X.-J. Bi, X.-G. He, E. Ma, and J. Zhang, *Cosmic $e^{\pm}, \bar{p}, \gamma$ and neutrino rays in leptocentric dark matter models*, *Phys.Rev.* **D81** (2010) 063522, [arXiv:0910.0771].

[40] G. D. Mack, T. D. Jacques, J. F. Beacom, N. F. Bell, and H. Yuksel, *Conservative Constraints on Dark Matter Annihilation into Gamma Rays*, *Phys.Rev.* **D78** (2008) 063542, [arXiv:0803.0157].

[41] P. Meade, M. Papucci, A. Strumia, and T. Volansky, *Dark Matter Interpretations of the Electron/Positron Excesses after FERMI*, *Nucl. Phys.* **B831** (2010) 178–203, [arXiv:0905.0480].

[42] D. Nekrassov and f. t. H. Collaboration, *Searches for DM signals from the Galactic Centre region with H.E.S.S*, *PoS* **IDM2010** (2011) 075, [arXiv:1106.2752].

[43] M. Regis and P. Ullio, *Multi-wavelength signals of dark matter annihilations at the Galactic center*, *Phys.Rev.* **D78** (2008) 043505, [arXiv:0802.0234].

[44] **Fermi-LAT** Collaboration, M. Ackermann *et. al.*, *Constraining Dark Matter Models from a Combined Analysis of Milky Way Satellites with the Fermi Large Area Telescope*, *Phys.Rev.Lett.* **107** (2011) 241302, [arXiv:1108.3546].

[45] A. Geringer-Sameth and S. M. Koushiappas, *Exclusion of canonical WIMPs by the joint analysis of Milky Way dwarfs with Fermi*, *Phys.Rev.Lett.* **107** (2011) 241303, [arXiv:1108.2914].

[46] O. Adriani *et. al.*, *An anomalous positron abundance in cosmic rays with energies 1.5.100 GeV*, *Nature* **458** (2009) 607–609, [arXiv:0810.4995].

[47] I. Cholis, D. P. Finkbeiner, L. Goodenough, and N. Weiner, *The PAMELA Positron Excess from Annihilations into a Light Boson*, *JCAP* **0912** (2009) 007, [arXiv:0810.5344].

[48] I. Cholis, L. Goodenough, D. Hooper, M. Simet, and N. Weiner, *High Energy Positrons From Annihilating Dark Matter*, *Phys.Rev.* **D80** (2009) 123511, [arXiv:0809.1683].

[49] M. Cirelli, M. Kadastik, M. Raidal, and A. Strumia, *Model-independent implications of the e+-, anti-proton cosmic ray spectra on properties of Dark Matter*, *Nucl.Phys.* **B813** (2009) 1–21, [arXiv:0809.2409].

[50] A. A. Abdo *et. al.*, *Measurement of the Cosmic Ray e+ plus e- spectrum from 20 GeV to 1 TeV with the Fermi Large Area Telescope*, *Phys. Rev. Lett.* **102** (2009) 181101, [arXiv:0905.0025].

[51] L. Bergstrom, J. Edsjo, and G. Zaharijas, *Dark matter interpretation of recent electron and positron data*, *Phys. Rev. Lett.* **103** (2009) 031103, [arXiv:0905.0333].

[52] I. Cholis, G. Dobler, D. P. Finkbeiner, L. Goodenough, and N. Weiner, *The Case for a 700+ GeV WIMP: Cosmic Ray Spectra from ATIC and PAMELA*, *Phys. Rev.* **D80** (2009) 123518, [arXiv:0811.3641].

[53] **The Fermi-LAT** Collaboration, M. Ackermann *et. al.*, *Measurement of separate cosmic-ray electron and positron spectra with the Fermi Large Area Telescope*, arXiv:1109.0521.

[54] N. Arkani-Hamed, D. P. Finkbeiner, T. R. Slatyer, and N. Weiner, *A Theory of Dark Matter*, *Phys.Rev.* **D79** (2009) 015014, [arXiv:0810.0713].

[55] M. Baumgart, C. Cheung, J. T. Ruderman, L.-T. Wang, and I. Yavin, *Non-Abelian Dark Sectors and Their Collider Signatures*, *JHEP* **0904** (2009) 014, [arXiv:0901.0283].

[56] A. Katz and R. Sundrum, *Breaking the Dark Force*, *JHEP* **0906** (2009) 003, [arXiv:0902.3271].

[57] M. Pospelov and A. Ritz, *Astrophysical Signatures of Secluded Dark Matter*, *Phys.Lett.* **B671** (2009) 391–397, [arXiv:0810.1502].

[58] M. R. Buckley and P. J. Fox, *Dark Matter Self-Interactions and Light Force Carriers*, *Phys.Rev.* **D81** (2010) 083522, [arXiv:0911.3898].

[59] J. B. Dent, S. Dutta, and R. J. Scherrer, *Thermal Relic Abundances of Particles with Velocity-Dependent Interactions*, *Phys.Lett.* **B687** (2010) 275–279, [arXiv:0909.4128].

[60] J. L. Feng, M. Kaplinghat, and H.-B. Yu, *Halo Shape and Relic Density Exclusions of Sommerfeld-Enhanced Dark Matter Explanations of Cosmic Ray Excesses*, *Phys.Rev.Lett.* **104** (2010) 151301, [arXiv:0911.0422].

[61] J. L. Feng, M. Kaplinghat, and H.-B. Yu, *Sommerfeld Enhancements for Thermal Relic Dark Matter*, *Phys.Rev.* **D82** (2010) 083525, [arXiv:1005.4678].

[62] J. Zavala, M. Vogelsberger, and S. D. White, *Relic density and CMB constraints on dark matter annihilation with Sommerfeld enhancement*, *Phys.Rev.* **D81** (2010) 083502, [arXiv:0910.5221].

[63] J. Hisano, M. Kawasaki, K. Kohri, T. Moroi, K. Nakayama, *et. al.*, *Cosmological constraints on dark matter models with velocity-dependent annihilation cross section*, *Phys.Rev.* **D83** (2011) 123511, [arXiv:1102.4658].

[64] N. Padmanabhan and D. P. Finkbeiner, *Detecting dark matter annihilation with CMB polarization: Signatures and experimental prospects*, *Phys.Rev.* **D72** (2005) 023508, [astro-ph/0503486].

[65] T. R. Slatyer, N. Padmanabhan, and D. P. Finkbeiner, *CMB Constraints on WIMP Annihilation: Energy Absorption During the Recombination Epoch*, *Phys.Rev.* **D80** (2009) 043526, [arXiv:0906.1197].

[66] D. P. Finkbeiner, L. Goodenough, T. R. Slatyer, M. Vogelsberger, and N. Weiner, *Consistent Scenarios for Cosmic-Ray Excesses from Sommerfeld-Enhanced Dark Matter Annihilation*, *JCAP* **1105** (2011) 002, [arXiv:1011.3082].

[67] T. R. Slatyer, N. Toro, and N. Weiner, *The Effect of Local Dark Matter Substructure on Constraints in Sommerfeld-Enhanced Models*, arXiv:1107.3546.

[68] J. Zavala, M. Vogelsberger, T. R. Slatyer, A. Loeb, and V. Springel, *The cosmic X-ray and gamma-ray background from dark matter annihilation*, *Phys.Rev.* **D83** (2011) 123513, [arXiv:1103.0776].

[69] M. Cirelli, P. Panci, and P. D. Serpico, *Diffuse gamma ray constraints on annihilating or decaying Dark Matter after Fermi*, *Nucl.Phys.* **B840** (2010) 284–303, [arXiv:0912.0663].

[70] J. Hisano, M. Kawasaki, K. Kohri, T. Moroi, and K. Nakayama, *Cosmic Rays from Dark Matter Annihilation and Big-Bang Nucleosynthesis*, *Phys.Rev.* **D79** (2009) 083522, [arXiv:0901.3582].

[71] J. Hisano, M. Kawasaki, K. Kohri, and K. Nakayama, *Positron/Gamma-Ray Signatures of Dark Matter Annihilation and Big-Bang Nucleosynthesis*, *Phys.Rev.* **D79** (2009) 063514, [arXiv:0810.1892].

[72] D. P. Finkbeiner and N. Weiner, *Exciting Dark Matter and the INTEGRAL/SPI 511 keV signal*, *Phys.Rev.* **D76** (2007) 083519, [astro-ph/0702587].

[73] B. J. Teegarden, K. Watanabe, P. Jean, J. Knodlseder, V. Lonjou, *et. al.*, *INTEGRAL/SPI limits on electron-positron annihilation radiation from the Galactic Plane*, *Astrophys.J.* **621** (2005) 296–300, [astro-ph/0410354].

[74] H. Zhan, *Optimal Softening for N-Body Halo Simulations*, *Astrophys. J.* **639** (2006) 617–620, [astro-ph/0507237].

[75] C. Power *et. al.*, *The Inner Structure of LambdaCDM Halos I: A Numerical Convergence Study*, *Mon. Not. Roy. Astron. Soc.* **338** (2003) 14–34, [astro-ph/0201544].

[76] G. Stinson *et. al.*, *Cosmological Galaxy Formation Simulations Using SPH*, arXiv:1004.0675.

[77] **The HESS** Collaboration, F. Aharonian *et. al.*, *The H.E.S.S. survey of the Inner Galaxy in very high-energy gamma-rays*, *Astrophys. J.* **636** (2006) 777–797, [astro-ph/0510397].

[78] L. Pieri, J. Lavalle, G. Bertone, and E. Branchini, *Implications of High-Resolution Simulations on Indirect Dark Matter Searches*, *Phys. Rev.* **D83** (2011) 023518, [arXiv:0908.0195].

[79] M. Kuhlen, J. Diemand, and P. Madau, *The Dark Matter Annihilation Signal from Galactic Substructure: Predictions for GLAST*, *Astrophys. J.* **686** (Oct., 2008) 262–278, [arXiv:0805.4416].

[80] J. Mardon, Y. Nomura, D. Stolarski, and J. Thaler, *Dark Matter Signals from Cascade Annihilations*, *JCAP* **0905** (2009) 016, [arXiv:0901.2926].

[81] P. Grajek, G. Kane, D. J. Phalen, A. Pierce, and S. Watson, *Neutralino Dark Matter from Indirect Detection Revisited*, arXiv:0807.1508.

[82] M. Kamionkowski, S. M. Koushiappas, and M. Kuhlen, *Galactic Substructure and Dark Matter Annihilation in the Milky Way Halo*, *Phys.Rev.* **D81** (2010) 043532, [arXiv:1001.3144].

[83] J. F. Navarro *et. al.*, *The Inner Structure of LambdaCDM Halos III: Universality and Asymptotic Slopes*, *Mon. Not. Roy. Astron. Soc.* **349** (2004) 1039, [astro-ph/0311231].

[84] M. Boylan-Kolchin, C.-P. Ma, and E. Quataert, *Dissipationless mergers of elliptical galaxies and the evolution of the fundamental plane*, *Mon.Not.Roy.Astron.Soc.* **362** (2005) 184–196, [astro-ph/0502495].

[85] I. Cholis and N. Weiner, *MiXDM: Cosmic Ray Signals from Multiple States of Dark Matter*, arXiv:0911.4954.

[86] The CTA Consortium, *Design Concepts for the Cherenkov Telescope Array*, arXiv:1008.3703.

[87] B. Gold *et. al.*, *Five-Year Wilkinson Microwave Anisotropy Probe (WMAP 1) Observations: Galactic Foreground Emission*, *Astrophys. J. Suppl.* **180** (2009) 265–282, [arXiv:0803.0715].

[88] G. Hinshaw *et. al.*, *Five-Year Wilkinson Microwave Anisotropy Probe (WMAP 1) Observations:Data Processing, Sky Maps, & Basic Results*, *Astrophys. J. Suppl.* **180** (2009) 225–245, [arXiv:0803.0732].

[89] D. P. Finkbeiner, *Microwave Interstellar Medium Emission Observed by the Wilkinson Microwave Anisotropy Probe*, *Astrophys. J.* **614** (Oct., 2004) 186–193, [0311547].

[90] M. Bottino, A. J. Banday, and D. Maino, *Foreground analysis of the WMAP three-year data with FASTICA*, arXiv:0807.1865.

[91] D. Hooper, D. P. Finkbeiner, and G. Dobler, *Evidence Of Dark Matter Annihilations In The WMAP Haze*, *Phys. Rev. D* **76** (2007) 083012, [arXiv:0705.3655].

[92] G. Dobler and D. P. Finkbeiner, *Extended Anomalous Foreground Emission in the WMAP 3-Year Data*, *Astrophys. J.* **680** (2008) 1222–1234, [arXiv:0712.1038].

[93] D. P. Finkbeiner, *WMAP microwave emission interpreted as dark matter annihilation in the inner Galaxy*, 0409027.

[94] K. Ferriere, *Interstellar magnetic fields in the Galactic center region*, arXiv:0908.2037.

[95] S. Kurtz, E. Churchwell, and D. O. S. Wood, *Ultracompact H II regions. 2: New high-resolution radio images*, *Astrophys. J. Supp.* **91** (Apr., 1994) 659–712.

[96] A. W. Strong and I. V. Moskalenko, *Propagation of cosmic-ray nucleons in the Galaxy*, *Astrophys. J.* **509** (1998) 212–228, [9807150].

[97] A. W. Strong, I. V. Moskalenko, and O. Reimer, *Diffuse continuum gamma rays from the Galaxy*, *Astrophys. J.* **537** (2000) 763–784, [9811296].

[98] E. A. Baltz and J. Edsjö, *Positron propagation and fluxes from neutralino annihilation in the halo*, *Phys. Rev. D* **59** (Jan., 1999) 023511–+, [9808243].

[99] E. A. Baltz and L. Wai, *Diffuse inverse Compton and synchrotron emission from dark matter annihilations in galactic satellites*, *Phys. Rev. D* **70** (July, 2004) 023512–+, [0403528].

[100] J. Zhang *et. al.*, *Discriminating different scenarios to account for the cosmic e + /- excess by synchrotron and inverse Compton radiation*, *Phys. Rev.* **D80** (2009) 023007, [arXiv:0812.0522].

[101] D. T. Cumberbatch, J. Zuntz, H. K. K. Eriksen, and J. Silk, *Can the WMAP Haze really be a signature of annihilating neutralino dark matter?*, arXiv:0902.0039.

[102] M. Kaplinghat, D. J. Phalen, and K. M. Zurek, *Pulsars as the Source of the WMAP Haze*, *JCAP* **0912** (2009) 010, [arXiv:0905.0487].

[103] A. Boulares, *The nature of the cosmic-ray electron spectrum, and supernova remnant contributions*, *Astrophys. J.* **342** (July, 1989) 807–813.

[104] D. Hooper, P. Blasi, and P. D. Serpico, *Pulsars as the Sources of High Energy Cosmic Ray Positrons*, *JCAP* **0901** (2009) 025, [arXiv:0810.1527].

[105] S. Profumo, *Dissecting cosmic-ray electron-positron data with Occam's Razor: the role of known Pulsars*, *Central Eur.J.Phys.* **10** (2011) 1–31, [arXiv:0812.4457].

[106] H. Yuksel, M. D. Kistler, and T. Stanev, *TeV Gamma Rays from Geminga and the Origin of the GeV Positron Excess*, *Phys. Rev. Lett.* **103** (2009) 051101, [arXiv:0810.2784].

[107] J. Chang *et. al.*, *An excess of cosmic ray electrons at energies of 300.800 GeV*, *Nature* **456** (2008) 362–365.

[108] **FERMI-LAT** Collaboration, D. Grasso *et. al.*, *On possible interpretations of the high energy electron- positron spectrum measured by the Fermi Large Area Telescope*, *Astropart. Phys.* **32** (2009) 140–151, [arXiv:0905.0636].

[109] S. M. Leach *et. al.*, *Component separation methods for the Planck mission*, *Astron. Astrophys.* **491** (2008) 597–615, [arXiv:0805.0269].

[110] **Planck Collaboration** Collaboration, Planck Collaboration, *The Scientific programme of planck*, astro-ph/0604069.

[111] V. Stolyarov, M. P. Hobson, M. A. J. Ashdown, and A. N. Lasenby, *All-sky component separation for the Planck mission*, *Mon. Not. Roy. Astron. Soc.* **336** (2002) 97–111, [0105432].

[112] L. Zhang and K. S. Cheng, *Cosmic-ray positrons from mature gamma-ray pulsars*, *Astron. & Astrophys.* **368** (Mar., 2001) 1063–1070.

[113] A. K. Harding and R. Ramaty, *The Pulsar Contribution to Galactic Cosmic Ray Positrons*, in *International Cosmic Ray Conference*, vol. 2, p. 92, 1987.

[114] R. Narayan, *The birthrate and initial spin period of single radio pulsars*, *Astrophys. J.* **319** (Aug., 1987) 162–179.

[115] M. Bailes and D. A. Kniffen, *Galactic gamma-ray emission from radio pulsars*, *Astrophys. J.* **391** (June, 1992) 659–666.

[116] M. Kramer *et. al.*, *The Effelsberg Search for Pulsars in the Galactic Centre*, 0002117.

[117] D. R. Lorimer, *The Galactic population and birth rate of radio pulsars*, 0308501.

[118] D. A. Leahy and X. Wu, *The Galactic distribution of shell-type supernova remnants*, *Pub. Astron. Soc. Pacific* **101** (June, 1989) 607–613.

[119] F. W. Stecker, *New galactic population class*, *Nature* **260** (Apr., 1976) 412–414.

[120] B. J. Robinson, R. N. Manchester, J. B. Whiteoak, D. B. Sanders, N. Z. Scoville, D. P. Clemens, W. H. McCutcheon, and P. M. Solomon, *The distribution of CO in the Galaxy for longitudes 294 deg to 86 deg*, *Astrophys. J. Lett.* **283** (Aug., 1984) L31–L35.

[121] G. Battaglia *et. al.*, *The radial velocity dispersion profile of the Galactic halo: Constraining the density profile of the dark halo of the Milky Way*, *Mon. Not. Roy. Astron. Soc.* **364** (2005) 433–442, [0506102].

[122] A. Klypin, H. Zhao, and R. S. Somerville, *LCDM-based models for the Milky Way and M31 I: Dynamical Models*, *Astrophys. J.* **573** (2002) 597–613, [0110390].

[123] **Particle Data Group** Collaboration, C. Amsler *et. al.*, *Review of particle physics*, *Phys. Lett. B* **667** (2008) 1.

[124] J. Lavalle, Q. Yuan, D. Maurin, and X. Bi, *Full Calculation of Clumpiness Boost factors for Antimatter Cosmic Rays in the light of Lambda-CDM N-body simulation results. Abandoning hope in clumpiness enhancement?*, *Astron.Astrophys.* **479** (2008) 427–452, [arXiv:0709.3634].

[125] C. Bennett *et. al.*, *First Year Wilkinson Microwave Anisotropy Probe (WMAP) Observations: Foreground Emission*, *Astrophys. J. Suppl.* **148** (2003) 97, [0302208].

[126] C. E. Fichtel *et. al.*, *High-energy gamma-ray results from the second small astronomy satellite*, *Astrophys. J.* **198** (May, 1975) 163–182.

[127] C. E. Fichtel *et. al.*, *SAS-2 observations of the diffuse gamma radiation in the galactic latitude interval from 10 to 90 deg in both hemispheres*, *Astrophys. J. Lett.* **217** (Oct., 1977) L9–L13.

[128] C. E. Fichtel, G. A. Simpson, and D. J. Thompson, *Diffuse gamma radiation*, *Astrophys. J.* **222** (June, 1978) 833–849.

[129] D. J. Thompson and C. E. Fichtel, *Extragalactic gamma radiation - Use of galaxy counts as a galactic tracer*, *Astron. & Astrophys.* **109** (May, 1982) 352–354.

[130] **Fermi-LAT Collaboration** Collaboration, A. A. Abdo *et. al.*, *The Spectrum of the Isotropic Diffuse Gamma-Ray Emission Derived From First-Year Fermi Large Area Telescope Data*, *Phys. Rev. Lett.* **104** (2010) 101101, [arXiv:1002.3603].

[131] **Fermi-LAT Collaboration** Collaboration, A. A. Abdo *et. al.*, *The Fermi-LAT high-latitude Survey: Source Count Distributions and the Origin of the Extragalactic Diffuse Background*, *Astrophys.J.* **720** (2010) 435–453, [arXiv:1003.0895].

[132] P. Sreekumar *et. al.*, *EGRET Observations of the Extragalactic Gamma-Ray Emission*, *Astrophys. J.* **494** (Feb., 1998) 523–+, [9709257].

[133] **Fermi-LAT** Collaboration, A. A. Abdo *et. al.*, *Constraints on Cosmological Dark Matter Annihilation from the Fermi-LAT Isotropic Diffuse Gamma-Ray Measurement*, *JCAP* **1004** (2010) 014, [arXiv:1002.4415].

[134] E. A. Baltz *et. al.*, *Pre-launch estimates for GLAST sensitivity to Dark Matter annihilation signals*, *JCAP* **0807** (2008) 013, [arXiv:0806.2911].

[135] Y. Inoue and T. Totani, *The Blazar Sequence and the Cosmic Gamma-Ray Background Radiation in the Fermi Era*, *Astrophys. J.* **702** (2009) 523–536, [arXiv:0810.3580].

[136] Y. Inoue *et. al.*, *The Cosmological Evolution of Blazars and the Extragalactic Gamma-Ray Background in the Fermi Era*, arXiv:1001.0103.

[137] Y. Inoue, T. Totani, and Y. Ueda, *The Cosmic MeV Gamma-Ray Background and Hard X-Ray Spectra of Active Galactic Nuclei: Implications for the Origin of Hot AGN Coronae*, *Astrophys. J. Lett.* **672** (Jan., 2008) L5–L8, [arXiv:0709.3877].

[138] B. D. Fields, V. Pavlidou, and T. Prodanovic, *Cosmic Gamma-Ray Background from Star-Forming Galaxies*, *Astrophys.J.* **722** (2010) L199, [arXiv:1003.3647].

[139] C. A. Faucher-Giguere and A. Loeb, *The Pulsar Contribution to the Gamma-Ray Background*, *JCAP* **1001** (2010) 005, [arXiv:0904.3102].

[140] J. M. Siegal-Gaskins, R. Reesman, V. Pavlidou, S. Profumo, and T. P. Walker, *Anisotropy Constraints on Millisecond Pulsars in the Diffuse Gamma Ray Background*, arXiv:1011.5501.

[141] S. Ando and E. Komatsu, *Anisotropy of the cosmic gamma-ray background from dark matter annihilation*, *Phys. Rev.* **D73** (2006) 023521, [astro-ph/0512217].

[142] S. Ando, E. Komatsu, T. Narumoto, and T. Totani, *Dark matter annihilation or unresolved astrophysical sources? Anisotropy probe of the origin of cosmic gamma-ray background*, *Phys. Rev.* **D75** (2007) 063519, [astro-ph/0612467].

[143] M. Fornasa, L. Pieri, G. Bertone, and E. Branchini, *Anisotropy probe of galactic and extra-galactic Dark Matter annihilations*, *Phys. Rev.* **D80** (2009) 023518, [arXiv:0901.2921].

[144] B. S. Hensley, J. M. Siegal-Gaskins, and V. Pavlidou, *The detectability of dark matter annihilation with Fermi using the anisotropy energy spectrum of the gamma-ray background*, *Astrophys. J.* **723** (2010) 277–284, [arXiv:0912.1854].

[145] F. Miniati, S. M. Koushiappas, and T. Di Matteo, *Angular Anisotropies in the Cosmic Gamma-ray Background as a Probe of its Origin*, *Astrophys. J.* **667** (2007) L1–L14, [astro-ph/0702083].

[146] J. M. Siegal-Gaskins, *Revealing dark matter substructure with anisotropies in the diffuse gamma-ray background*, *JCAP* **0810** (2008) 040, [arXiv:0807.1328].

[147] J. M. Siegal-Gaskins and V. Pavlidou, *Robust identification of isotropic diffuse gamma rays from Galactic dark matter*, *Phys. Rev. Lett.* **102** (2009) 241301, [arXiv:0901.3776].

[148] F. Stecker and M. Salamon, *The Gamma-ray background from blazars: A New look*, *Astrophys.J.* **464** (1996) 600–605, [astro-ph/9601120].

[149] D. Bhattacharya, P. Sreekumar, and R. Mukherjee, *Gamma-ray luminosity function of Gamma-ray bright AGNs*, *Res. Astron. Astrophys.* **9** (2009) 85–94, [arXiv:0811.4388].

[150] J. Chiang *et. al.*, *The Evolution of Gamma-Ray–loud Active Galactic Nuclei*, *Astrophys. J.* **452** (Oct., 1995) 156–+.

[151] J. Chiang and R. Mukherjee, *The Luminosity Function of the EGRET Gamma-Ray Blazars*, *Astrophys. J.* **496** (Mar., 1998) 752–+.

[152] C. D. Dermer, *Statistics of Cosmological Black Hole Jet Sources: Blazar Predictions for the Gamma-Ray Large Area Space Telescope*, *Astrophys. J.* **659** (Apr., 2007) 958–975, [0605402].

[153] P. Giommi *et. al.*, *Non-thermal Cosmic Backgrounds from Blazars: the contribution to the CMB, X-ray and gamma-ray Backgrounds*, *Astron. Astrophys.* **445** (2006) 843–855, [astro-ph/0508034].

[154] A. Mücke and M. Pohl, *The contribution of unresolved radio-loud AGN to the extragalactic diffuse gamma-ray background*, *Mon. Not. Roy. Astron. Soc.* **312** (Feb., 2000) 177–193.

[155] T. Narumoto and T. Totani, *Gamma-Ray Luminosity Function of Blazars and the Cosmic Gamma-Ray Background: Evidence for the Luminosity Dependent Density Evolution*, *Astrophys. J.* **643** (2006) 81, [astro-ph/0602178].

[156] P. Padovani *et. al.*, *Radio-loud AGN and the extragalactic gamma-ray background*, *Mon. Not. Roy. Astron. Soc.* **260** (Feb., 1993) L21–L24.

[157] V. Pavlidou and T. M. Venters, *The Spectral Shape of the Gamma-Ray Background from Blazars*, *Astrophys. J.* **673** (Jan., 2008) 114–118, [arXiv:0710.0002].

[158] M. H. Salamon and F. W. Stecker, *The blazar gamma-ray luminosity function and the diffuse extragalactic gamma-ray background*, *Astrophys. J. Lett.* **430** (July, 1994) L21–L24.

[159] F. W. Stecker, M. H. Salamon, and M. A. Malkan, *The high-energy diffuse cosmic gamma-ray background radiation from blazars*, *Astrophys. J. Lett.* **410** (June, 1993) L71–L74.

[160] D. Donato *et. al.*, *Hard X-ray properties of blazars*, *Astron. & Astrophys.* **375** (Sept., 2001) 739–751, [0105203].

[161] G. Fossati *et. al.*, *Unifying models for X-ray selected and Radio selected BL Lac Objects*, astro-ph/9704113.

[162] G. Fossati *et. al.*, *A Unifying View of the Spectral Energy Distributions of Blazars*, *Mon. Not. Roy. Astron. Soc.* **299** (1998) 433–448, [astro-ph/9804103].

[163] **Fermi-LAT Collaboration** Collaboration, A. A. Abdo *et. al.*, *Spectral Properties of Bright Fermi-Detected Blazars in the Gamma-Ray Band*, *Astrophys. J.* **710** (Feb., 2010) 1271–1285.

[164] D. Donato *et. al.*, *Hard X-ray properties of blazars*, astro-ph/0105203.

[165] Y. Ueda, M. Akiyama, K. Ohta, and T. Miyaji, *Cosmological Evolution of the Hard X-ray AGN Luminosity Function and the Origin of the Hard X-ray Background*, *Astrophys. J.* **598** (2003) 886–908, [astro-ph/0308140].

[166] D. Malyshev and D. W. Hogg, *Statistics of gamma-ray point sources below the Fermi detection limit*, *Astrophys.J.* **738** (2011) 181, [arXiv:1104.0010].

[167] R. C. Hartman *et. al.*, *The Third EGRET Catalog of High-Energy Gamma-Ray Sources*, *Astrophys. J. Supp.* **123** (July, 1999) 79–202.

[168] C. M. Urry and P. Padovani, *Unified Schemes for Radio-Loud Active Galactic Nuclei*, *Pub. Astron. Soc. Pacific* **107** (Sept., 1995) 803–+, [9506063].

[169] R. D. Blandford and A. Konigl, *Relativistic jets as compact radio sources*, *Astrophys. J.* **232** (Aug., 1979) 34–48.

[170] C. D. Dermer and N. Gehrels, *Two Classes of Gamma-Ray–emitting Active Galactic Nuclei*, *Astrophys. J.* **447** (July, 1995) 103–+.

[171] **Fermi-LAT Collaboration** Collaboration, A. A. Abdo *et. al.*, *The First Catalog of Active Galactic Nuclei Detected by the Fermi Large Area Telescope*, *Astrophys. J.* **715** (2010) 429–457, [arXiv:1002.0150].

[172] **Fermi-LAT Collaboration** Collaboration, A. A. Abdo *et. al.*, *The Spectral Energy Distribution of Fermi bright blazars*, *Astrophys. J.* **716** (2010) 30–70, [arXiv:0912.2040].

[173] G. Ghisellini, L. Maraschi, and F. Tavecchio, *The Fermi blazars' divide*, *Mon. Not. Roy. Astron. Soc.* **396** (June, 2009) L105–L109, [arXiv:0903.2043].

[174] G. Hasinger, T. Miyaji, and M. Schmidt, *Luminosity-dependent evolution of soft X-ray selected AGN: New Chandra and XMM-Newton surveys*, *Astron. Astrophys.* **441** (2005) 417–434, [astro-ph/0506118].

[175] H. Falcke, E. Koerding, and S. Markoff, *A Scheme to Unify Low-Power Accreting Black Holes - Jet- Dominated Accretion Flows and the Radio/X-Ray Correlation*, *Astron. Astrophys.* **414** (2004) 895–903, [astro-ph/0305335].

[176] E. Gallo *et. al.*, *A dark jet dominates the power output of the stellar black hole Cygnus X-1*, *Nature* **436** (2005) 819–821, [astro-ph/0508228].

[177] A. Merloni, S. Heinz, and T. Di Matteo, *A fundamental plane of black hole activity*, *Mon. Not. Roy. Astron. Soc.* **345** (2003) 1057, [astro-ph/0305261].

[178] A. Marconi *et. al.*, *Local Supermassive Black Holes, Relics of Active Galactic Nuclei and the X-ray Background*, *Mon. Not. Roy. Astron. Soc.* **351** (2004) 169, [astro-ph/0311619].

[179] R. C. Gilmore *et. al.*, *GeV Gamma-Ray Attenuation and the High-Redshift UV Background*, *Mon. Not. Roy. Astron. Soc.* **399** (Nov., 2009) 1694–1708, [arXiv:0905.1144].

[180] **Fermi-LAT Collaboration** Collaboration, A. A. Abdo *et. al.*, *Fermi Large Area Telescope Constraints on the Gamma-ray Opacity of the Universe*, *Astrophys. J.* **723** (2010) 1082–1096, [arXiv:1005.0996].

[181] S. C. Kappadath *et. al.*, *The preliminary cosmic diffuse γ-ray spectrum from 800keV to 30MeV measured with COMPTEL.*, *Astron. & Astrophys. Supp.* **120** (Dec., 1996) C619+.

[182] K. Watanabe, D. H. Hartmann, M. D. Leising, and L. S. The, *Constraining the Cosmic Star Formation Rate with the MeV Background*, *Nucl. Phys.* **A718** (2003) 425–427, [astro-ph/0306161].

[183] A. Pushkarev, Y. Kovalev, M. Lister, and T. Savolainen, *Jet opening angles and gamma-ray brightness of AGN*, arXiv:0910.1813.

[184] J. H. Krolik, *Active Galactic Nuclei: From the Central Black Hole to the Galactic Environment*. Princeton University Press, Princeton, N.J., 1998.

[185] Y. Inoue, S. Inoue, M. A. R. Kobayashi, T. Totani, J. Kataoka, and R. Sato, *Searching for the most distant blazars with the Fermi Gamma-ray Space Telescope*, *Mon. Not. Roy. Astron. Soc.* **411** (Feb., 2011) 464–468, [arXiv:1007.4379].

[186] **LAT** Collaboration, W. B. Atwood *et. al.*, *The Large Area Telescope on the Fermi Gamma-ray Space Telescope Mission*, *Astrophys. J.* **697** (2009) 1071–1102, [arXiv:0902.1089].

[187] G. G. Vargas, o. b. o. t. F.-L. collaboration, and E. Komatsu, *Measurement of anisotropies in the large-scale diffuse gamma-ray emission*, *Nuovo Cim.* **C34N3** (2011) 327–331, [arXiv:1012.0755].

[188] T. M. Venters and V. Pavlidou, *The Effect of Blazar Spectral Breaks on the Blazar Contribution to the Extragalactic Gamma-ray Background*, *Astrophys. J., in press* (2011) [arXiv:1105.0372].

[189] F. W. Stecker and T. M. Venters, *Components of the Extragalactic Gamma Ray Background*, *Astrophys.J.* **736** (2011) 40, [arXiv:1012.3678].

[190] A. Neronov and D. Semikoz, *Extragalactic Very-High-Energy gamma-ray background*, arXiv:1103.3484.

[191] E. T. Meyer, G. Fossati, M. Georganopoulos, and M. L. Lister, *From the Blazar Sequence to the Blazar Envelope: Revisiting the Relativistic Jet Dichotomy in Radio-loud AGN*, *Astrophys.J.* **740** (2011) 98, [arXiv:1107.5105].

[192] M. Cavadini, R. Salvaterra, and F. Haardt, *A New model for the extragalactic γ-ray background*, arXiv:1105.4613.

[193] J. Singal, V. Petrosian, and M. Ajello, *Flux and Photon Spectral Index Distributions of Fermi-LAT Blazars And Contribution To The Extragalactic Gamma-ray Background*, *Astrophysical Journal* (2011) [arXiv:1106.3111].

[194] Y. Cai, M. A. Luty, and D. E. Kaplan, *Leptonic Indirect Detection Signals from Strongly Interacting Asymmetric Dark Matter*, arXiv:0909.5499.

[195] A. Falkowski, J. T. Ruderman, and T. Volansky, *Asymmetric Dark Matter from Leptogenesis*, *JHEP* **05** (2011) 106, [arXiv:1101.4936].

[196] G. Kane, R. Lu, and S. Watson, *PAMELA Satellite Data as a Signal of Non-Thermal Wino LSP Dark Matter*, *Phys.Lett.* **B681** (2009) 151–160, [arXiv:0906.4765].

[197] S. Andreas, T. Hambye, and M. H. Tytgat, *WIMP dark matter, Higgs exchange and DAMA*, *JCAP* **0810** (2008) 034, [arXiv:0808.0255].

[198] C. Arina and M. H. Tytgat, *Constraints on a Light WIMP from the Isotropic Diffuse Gamma-Ray Emission*, arXiv:1007.2765.

[199] C. P. Burgess, M. Pospelov, and T. ter Veldhuis, *The minimal model of nonbaryonic dark matter: A singlet scalar*, *Nucl. Phys.* **B619** (2001) 709–728, [hep-ph/0011335].

[200] K. N. Abazajian, M. Markevitch, S. M. Koushiappas, and R. C. Hickox, *Limits on the radiative decay of sterile neutrino dark matter from the unresolved cosmic and soft X-ray backgrounds*, *Phys. Rev.* **D75** (2007) 063511, [astro-ph/0611144].

[201] S. Profumo and T. E. Jeltema, *Extragalactic Inverse Compton Light from Dark Matter Annihilation and the Pamela Positron Excess*, *JCAP* **0907** (2009) 020, [arXiv:0906.0001].

[202] T. F.-L. Collaboration, *Fermi Large Area Telescope Second Source Catalog*, arXiv:1108.1435.

[203] J. R. Mattox *et. al.*, *The Likelihood Analysis of EGRET Data*, *Astrophys. J.* **461** (1996) 396.

[204] L. Bergstrom, J. Edsjo, and P. Ullio, *Spectral gamma-ray signatures of cosmological dark matter annihilations*, *Phys. Rev. Lett.* **87** (2001) 251301, [astro-ph/0105048].

[205] P. Ullio, L. Bergstrom, J. Edsjo, and C. G. Lacey, *Cosmological dark matter annihilations into gamma-rays: A closer look*, *Phys. Rev.* **D66** (2002) 123502, [astro-ph/0207125].

[206] S. Ando, *Can dark matter annihilation dominate the extragalactic gamma-ray background?*, *Phys. Rev. Lett.* **94** (2005) 171303, [astro-ph/0503006].

[207] H. Yuksel, S. Horiuchi, J. F. Beacom, and S. Ando, *Neutrino Constraints on the Dark Matter Total Annihilation Cross Section*, *Phys. Rev.* **D76** (2007) 123506, [arXiv:0707.0196].

[208] L. Bergstrom, T. Bringmann, and J. Edsjo, *Complementarity of direct dark matter detection and indirect detection through gamma-rays*, *Phys.Rev.* **D83** (2011) 045024, [arXiv:1011.4514].

[209] A. Abdo *et. al.*, *Observations of Milky Way Dwarf Spheroidal galaxies with the Fermi-LAT detector and constraints on Dark Matter models*, *Astrophys.J.* **712** (2010) 147–158, [arXiv:1001.4531].

[210] D. Hooper and L. Goodenough, *Dark Matter Annihilation in The Galactic Center As Seen by the Fermi Gamma Ray Space Telescope*, arXiv:1010.2752.

[211] R. J. Scherrer and M. S. Turner, *On the relic, cosmic abundance of stable, weakly interacting massive particles*, *Phys. Rev. D* **33** (Mar, 1986) 1585–1589.

[212] G. Steigman, *Cosmology Confronts Particle Physics*, *Ann. Rev. Nucl. Part. Sci.* **29** (1979) 313–338.

[213] Y. B. Zeldovich, *A magnetic model of the universe*, *Zh. Eksp. Teor. Fiz.* **48** (1965) 986.

[214] K. N. Abazajian, *The Consistency of the Dark-Matter-Interpreted Fermi-LAT Observations of the Galactic Center with a Millisecond Pulsar Population in the Central Stellar Cluster*, arXiv:1011.4275.

[215] P. Meade, M. Papucci, and T. Volansky, *Dark Matter Sees The Light*, *JHEP* **12** (2009) 052, [arXiv:0901.2925].

[216] M. Papucci and A. Strumia, *Robust implications on Dark Matter from the first FERMI sky gamma map*, *JCAP* **1003** (2010) 014, [arXiv:0912.0742].

[217] S. Galli, F. Iocco, G. Bertone, and A. Melchiorri, *CMB constraints on Dark Matter models with large annihilation cross-section*, *Phys. Rev.* **D80** (2009) 023505, [arXiv:0905.0003].

[218] L. Dugger, T. E. Jeltema, and S. Profumo, *Constraints on Decaying Dark Matter from Fermi Observations of Nearby Galaxies and Clusters*, *JCAP* **1012** (2010) 015, [arXiv:1009.5988].

[219] **XENON100 Collaboration** Collaboration, E. Aprile *et. al.*, *Likelihood Approach to the First Dark Matter Results from XENON100*, *Phys.Rev.* **D84** (2011) 052003, [arXiv:1103.0303].

[220] **CoGeNT** Collaboration, C. Aalseth *et. al.*, *Results from a Search for Light-Mass Dark Matter with a P-type Point Contact Germanium Detector*, *Phys.Rev.Lett.* **106** (2011) 131301, [arXiv:1002.4703].

[221] C. Savage, G. Gelmini, P. Gondolo, and K. Freese, *XENON10/100 dark matter constraints in comparison with CoGeNT and DAMA: examining the Leff dependence*, arXiv:1006.0972.

[222] B. Feldstein, A. Fitzpatrick, E. Katz, and B. Tweedie, *A Simple Explanation for DAMA with Moderate Channeling*, *JCAP* **1003** (2010) 029, [arXiv:0910.0007].

[223] J. Kopp, T. Schwetz, and J. Zupan, *Global interpretation of direct Dark Matter searches after CDMS-II results*, *JCAP* **1002** (2010) 014, [arXiv:0912.4264].

[224] **CDMS-II Collaboration** Collaboration, Z. Ahmed *et. al.*, *Results from a Low-Energy Analysis of the CDMS II Germanium Data*, *Phys.Rev.Lett.* **106** (2011) 131302, [arXiv:1011.2482].

[225] **DAMA Collaboration** Collaboration, R. Bernabei *et. al.*, *First results from DAMA/LIBRA and the combined results with DAMA/NaI*, *Eur.Phys.J.* **C56** (2008) 333–355, [arXiv:0804.2741].

[226] A. Abdo, B. Allen, T. Aune, D. Berley, C. Chen, *et. al.*, *Milagro Observations of TeV Emission from Galactic Sources in the Fermi Bright Source List*, *Astrophys.J.* **700** (2009) L127–L131, [arXiv:0904.1018].

[227] **The Milagro** Collaboration, R. W. Atkins *et. al.*, *TeV gamma-ray survey of the Northern hemisphere sky using the Milagro Observatory*, *Astrophys.J.* (2004) [astro-ph/0403097].

[228] **HAWC** Collaboration, J. Goodman, *HAWC in the Fermi Era*, *Proceedings of the 31st ICRC* (2009).

[229] **HAWC** Collaboration, M. M. Gonzalez, *The High Altitude Water Cherenkov observatory, HAWC. Design and Performance*, *Proceedings of the 31st ICRC* (2009).

[230] **HAWC** Collaboration, H. Salazar, *The HAWC observatory and its synergies at volcan Sierra Negra*, *Proceedings of the 31st ICRC* (2009).

[231] E. J. Baxter and S. Dodelson, *A Robust Approach to Constraining Dark Matter from Gamma-Ray Data*, *Phys.Rev.* **D83** (2011) 123516, [arXiv:1103.5779].

[232] D. Hooper and T. Linden, *On The Origin Of The Gamma Rays From The Galactic Center*, *Phys.Rev.* **D84** (2011) 123005, [arXiv:1110.0006].

[233] **HESS** Collaboration, A. Abramowski *et. al.*, *H.E.S.S. constraints on Dark Matter annihilations towards the Sculptor and Carina Dwarf Galaxies*, *Astropart.Phys.* **34** (2011) 608–616, [arXiv:1012.5602].

[234] **The MAGIC** Collaboration, J. Aleksic *et. al.*, *Searches for Dark Matter annihilation signatures in the Segue 1 satellite galaxy with the MAGIC-I telescope*, *JCAP* **1106** (2011) 035, [arXiv:1103.0477].

[235] **The VERITAS** Collaboration, V. Acciari *et. al.*, *VERITAS Search for VHE Gamma-ray Emission from Dwarf Spheroidal Galaxies*, *Astrophys.J.* **720** (2010) 1174–1180, [arXiv:1006.5955].

[236] **VERITAS** Collaboration, E. Aliu *et. al.*, *VERITAS Deep Observations of the Dwarf Spheroidal Galaxy Segue 1*, *Phys.Rev.* **D85** (2012) 062001, [arXiv:1202.2144].

[237] K. Griest and M. Kamionkowski, *Unitarity Limits on the Mass and Radius of Dark Matter Particles*, *Phys.Rev.Lett.* **64** (1990) 615.

[238] L. Hui, *Unitarity Bounds and the Cuspy Halo Problem*, *Phys. Rev. Lett.* **86** (2001) 3467–3470, [astro-ph/0102349].

[239] **The Fermi-LAT** Collaboration, R. Rando, *Post-launch performance of the Fermi Large Area Telescope*, arXiv:0907.0626.

[240] **H.E.S.S.** Collaboration, *H.E.S.S. contributions to the 28th international cosmic ray conference*, astro-ph/0307452.

[241] E. Carmona, J. Sitarek, P. Colin, M. Doert, S. Klepser, *et. al.*, *Performance of the MAGIC Stereo System*, arXiv:1110.0947.

[242] T. Weekes, H. Badran, S. Biller, I. Bond, S. Bradbury, *et. al.*, *VERITAS: The Very energetic radiation imaging telescope array system*, *Astropart.Phys.* **17** (2002) 221–243, [astro-ph/0108478].

[243] B. Gold, N. Odegard, J. Weiland, R. Hill, A. Kogut, *et. al.*, *Seven-Year Wilkinson Microwave Anisotropy Probe (WMAP) Observations: Galactic Foreground Emission*, *Astrophys.J.Suppl.* **192** (2011) 15, [arXiv:1001.4555].

[244] G. Dobler, D. P. Finkbeiner, I. Cholis, T. R. Slatyer, and N. Weiner, *The Fermi Haze: A Gamma-Ray Counterpart to the Microwave Haze*, *Astrophys.J.* **717** (2010) 825–842, [arXiv:0910.4583].

[245] M. Su, T. R. Slatyer, and D. P. Finkbeiner, *Giant Gamma-ray Bubbles from Fermi-LAT: AGN Activity or Bipolar Galactic Wind?*, *Astrophys.J.* **724** (2010) 1044–1082, [arXiv:1005.5480].

[246] G. Dobler, *A Last Look at the Microwave Haze/Bubbles with WMAP*, arXiv:1109.4418.

[247] M. Ackermann, M. Ajello, A. Albert, L. Baldini, J. Ballet, *et. al.*, *Anisotropies in the diffuse gamma-ray background measured by the Fermi LAT*, arXiv:1202.2856.

[248] A. Cuoco, E. Komatsu, and J. Siegal-Gaskins, *Joint anisotropy and source count constraints on the contribution of blazars to the diffuse gamma-ray background*, arXiv:1202.5309.

[249] J. Goodman. Private communication, 2012.

[250] E. Kolb and M. Turner, *The Early Universe*. Westview Press, 1994.

[251] Y. Inoue and T. Totani, *The Blazar Sequence and the Cosmic Gamma-Ray Background Radiation in the Fermi Era*, *Astrophys. J.* **702** (2009) 523–536, [arXiv:0810.3580].

[252] F. Halzen and A. D. Martin, *Quarks & Leptons*. John Wiley and Sons, Inc., 1984.